MICROFLUIDIC CHAMBER ARRAYS FOR TESTING CELLULAR RESPONSES TO SOLUBLE-MATRIX AND GRADIENT SIGNALS

A Dissertation
Presented to
The Academic Faculty

by

Edward S. Park

In Partial Fulfillment
of the Requirements for the Degree
Doctor of Philosophy in the
School of Chemical and Biomolecular Engineering

Georgia Institute of Technology
May 2011

MICROFLUIDIC CHAMBER ARRAYS FOR TESTING CELLULAR RESPONSES TO SOLUBLE-MATRIX AND GRADIENT SIGNALS

Approved by:

Dr. Hang Lu, Advisor
School of Chemical and Biomolecular Engineering
Georgia Institute of Technology

Dr. Thomas H. Barker
Department of Biomedical Engineering
Georgia Institute of Technology

Dr. Andrés J. García
School of Mechanical Engineering
Georgia Institute of Technology

Dr. Paul A. Kohl
School of Chemical and Biomolecular Engineering
Georgia Institute of Technology

Dr. Mark R. Prausnitz
School of Chemical and Biomolecular Engineering
Georgia Institute of Technology

Date Approved: Dec. 16, 2010

For my father, Raymond J. Park

"For I know the plans I have for you," declares the LORD,
"plans to prosper you and not to harm you, plans to give you hope and a future."

Jeremiah 29:11

ACKNOWLEDGEMENTS

This work is the product of the kindness, guidance, and companionship of many people. First, I thank my advisor, Prof. Hang Lu, who put her confidence in me for over five years and never appeared to lose it, despite the challenges we faced. I thank her for her guidance, support, patience, and willingness to challenge me at crucial moments in this research. Also, I thank my thesis committee, Prof. Thomas Barker, Prof. Andrés García, Prof. Paul Kohl, and Prof. Mark Prausnitz, who have provided valuable insight and guidance. I only wish I could have spoken with them more. I specifically thank Tom Barker, who I spoke with on numerous occasions, and whose presence I never left without feeling as if I knew a little more about cell biology.

I thank the members of the Lu Research Group. First, I thank Dr. Kwanghun Chung, who provided helpful discussions, encouragement, and interesting topics of conversation. I thank Matthew Crane, who is always willing to get a cup coffee and engage in technical as well as lively political discussions. I thank Jeffrey Stirman for his help as the laboratory's jack-of-all-trades, particularly for experimental automation. I appreciate Alison Paul, Shalu Suri, and Jan Krajniak, who kept me company in the ES&T laboratory; particularly Jan, who often kept the same late hours, both in ES&T and in the cleanroom. And I thank Gina Cremona, a good friend and lab alumnus.

There is also Ivan Cáceres, Catherine Rivet, and Mei Zhan, who provided important help or discussion at various times; and I thank Taymour Hammoudi, my breakfast partner in the middle years of the research, waking up early for a warm meal and research discussions (among other things). I also thank Hyewon Lee, Loice

Chingozha, Dr. Sharon Hamilton, and Christine Alberico for making the lab such a comfortable and warm place to work. I will miss the group.

I worked closely with Michael DiFeo, who I especially thank for assisting me to a level that is above and beyond a typical undergraduate researcher's contribution. I thank Mike for his eagerness to learn (and to challenge me), and I am glad we are friends. As well, I thank Jacqueline Rand, who made great contributions in the final term of this work and showed great effort and intellect; also, my thanks go to Ashley Brown for being a most excellent and insightful collaborator and co-author. And I thank David Dumbauld and Dr. Sean Coyer for helpful discussions related to the project.

My gratitude goes to colleagues I met in the School of Chemical and Biomolecular Engineering. I thank Dr. J. R. Johnson (one of the first people I met from the department who made me feel very welcomed), Dr. Jason Ward, Dr. Thomas Rogers, Janna Blum, Scott Wilson, Dr. Pei Yoong Koh, and the others who are such excellent contemporaries. I especially thank Avishek Aiyar, Samirkumar Patel, and Dr. Venmathy Rajarathinam for their friendship. Finally among ChBE, I thank Richard A. Lawson, who is a great friend and was the superb emcee of my wedding. I also thank his lovely wife (and colleague) Alison Lawson for her help and support.

Finally, and most importantly, I thank my family. I thank my mother, Janice Youngja Park, for her constant prayers, support, wisdom, and tremendous love. And I thank my sisters, Kathleen and Christine, for their love, support, and understanding. Lastly, I thank my wonderful wife Jennifer Marie Park. Her support, patience, understanding, and love have been an amazing blessing to me. I am so thankful she came into my life on this journey. I give my love and gratitude to my wonderful family.

Soli Deo gloria.

TABLE OF CONTENTS

Page

ACKNOWLEDGEMENTS iv

LIST OF TABLES xi

LIST OF FIGURES xii

SUMMARY xiv

CHAPTER

1 INTRODUCTION 1

Challenges in Cell-Based Assays 1

Research Objectives 2

Objective 1: Develop a Reliable Method to Fabricate 3-D Flow Networks 3

Objective 2: Design, Realize, and Test a Novel Chamber Array for Combinations of Matrix and Soluble Signals 3

Objective 3: Design, Realize, and Test a Novel Chamber Array That Generates Soluble Signal Gradients 4

2 BACKGROUND 5

Signaling and the Microenvironment 5

Combinations of Multiple Signaling Fields 6

Gradient Signaling Fields 7

Two Examples of Cellular Response 8

Epithelial-to-Mesenchymal Transition (EMT) 8

Signal Combinations and EMT 9

Significance and Challenges of EMT Studies 9

Cell Migration 10

Basic Process of Cell Migration 11

Significance and Difficulty in Cell Migration Studies 12

In Vitro Screening Tools 14

Traditional Screening Platforms 14

Microfluidic Systems 15

Tools for Combinations of Multiple, Overlapping Signaling Fields 16

Tools for Gradient Signaling Fields 17

Needs Addressed 19

3 FABRICATION OF 3-DIMENSIONAL FLOW NETWORKS 21

3-Dimensional Flow Networks 21

Process Development 22

Protrusion Method: Attempts and Learning 22

Compression-Molding: Attempts and Learning 26

Semi-Automated Compression-Molding with NIL: Attempts and Learning 33

Adopted Fabrication Method: Modified Compression-Molding 35

Discussion 39

Estimated Yields and Observed Failure Modes 39

Scaling Efficiency and Scaling Rules 42

Microfluidic Arrays and Well Plates 45

General Discussion 48

Chapter Summary 50

4 A MICROFLUIDIC CHAMBER ARRAY FOR STUDYING CELLULAR RESPONSE TO COMBINATIONS OF MATRIX AND SOLUBLE SIGNALS 52

Specific Motivation and Objectives 52

Device Design 54
Three Attributes 55
Modes of Operation 56
Methods 58
Fabrication 58
Simulation of Chamber Flow Fields 59
Cell Culture Off-Device 59
Microscope Setup and Supporting Apparatus 60
Device Preparation and Cell Culture In-Device 60
Cell Assays 61
Data Analysis 62
Results and Discussion 63
Device Characterization 63
ATII Response to Soluble-Matrix Signal Combinations 66
Limitations of Data and Confirming Phenotypes 73
Chapter Summary 74
Further Work 75
5 MODULATING SOLUBLE GRADIENTS USING SEQUENTIALLY PULSED DELIVERY IN A MICROFLUIDIC CHAMBER ARRAY 77
Motivation: Gradients and Gradient-Generating Devices 77
Flow-Based and Free-Diffusion-Based Microfluidic Gradient Devices 79
Device Design 81
Sequentially Pulsed Delivery Concept 82
Low Shear Microenvironment 82
Temporal and Spatial Control of Gradients 83
Chambers, Array, and Fabrication Approach 84

Methods 85
Fabrication 85
Numerical Simulations 87
Flow Field and Shear Stresses 87
Diffusion-Only Gradient Formation for Comparison with Experimental Data 88
Gradient Characterization Using a Fluorescent Marker 88
Cell Culture Off-Device 89
Experimental Setup 89
Device Preparation, Cell Loading, and Incubation In-Device 90
Experiment and Image Acquisition 91
Image Processing and Cell Tracking 91
Data Analysis 93
Results and Discussion 94
Simulation of Chamber Flow Field 95
Characterization of Gradient Formation 97
Observations 98
Discussion 100
Comparison of Concentration Profiles to Diffusion-Only Model 102
Concentration Profile Variation 104
Testing of Device via Cell Migration Experiments 106
Observations 108
Discussion 112
Chapter Summary 115
6 CONCLUSIONS 120
Fabrication of 3-D Flow Networks 120

Microfluidic Chamber Array for Soluble-Matrix Signaling Studies 122

Soluble Gradients via Sequentially-Pulsed Delivery in a Chamber Array 123

Future Potential for Technology in This Work – Possible Applications in Cancer 124

Challenges and Future Directions for Microfluidic Systems 125

APPENDIX A: LAYOUTS OF MICROFLUIDIC DEVICES 128

APPENDIX B: EXPERIMENTAL SETUP 130

APPENDIX C: INTEGRATED, ON-CHIP VALVES 131

APPENDIX D: WAFER LEVEL VIEW OF MODIFIED COMPRESSION-MOLDING 132

APPENDIX E: DETAILED FABRICATION PROCESS 133

APPENDIX F: TRANSWELL ASSAYS 136

APPENDIX G: CONTROL TRIALS FOR FBS GRADIENT EXPERIMENTS 137

APPENDIX H: TIME-DEPENDENT RESULTS FROM FBS GRADIENT EXPERIMENTS 138

APPENDIX I: CELL SEGMENTATION CODE 141

REFERENCES 148

LIST OF TABLES

Page

Table 3-1: Estimated yields in fabrication of chamber array devices 39

Table 3-2: Failure modes observed while fabricating soluble-matrix and gradient devices 41

Table 3-3: Chapter summary 51

Table 4-1: Chapter summary 76

Table 5-1: Design objectives and corresponding features 81

Table 5-2: Chapter summary 119

Table E-1: Details for the modified compression-molding process described in Chapter 3 134

LIST OF FIGURES

Page

Figure 3-1: Illustration of protrusion fabrication process 23

Figure 3-2: Images of PDMS spin coated on SU-8 features 24

Figure 3-3: Putative failure modes of protrusion method 25

Figure 3-4: Compression-molding process in summary 27

Figure 3-5: Photoresist support posts 29

Figure 3-6: Gas bubbles nucleated in PDMS during compression 30

Figure 3-7: Partial curing of PDMS during compression-molding 31

Figure 3-8: Residual PDMS on the surface of SU-8 (photoresist) features after compression –molding 33

Figure 3-9: Schematic of highly conformal transparencies after NIL compression 34

Figure 3-10: Compression-molding step with pressure localized above device 35

Figure 3-11: PDMS device fabrication process 38

Figure 3-12: Example of a gain in scaling efficiency using 3-D flows 43

Figure 3-13: Scaling inlet/outlet ports for the problem in Fig. 3-12 (combinatorial conditions by rows and columns) 44

Figure 3-14: Through-holes in finished devices 50

Figure 4-1: Schematic of device architecture 54

Figure 4-2: Selected modes of operation shown in a subarray of 4 chambers 57

Figure 4-3: Flow characterization with colored dyes 64

Figure 4-4: Simulation of chamber flow field 66

Figure 4-5: Phase contrast images (representative) of ATII cells after 2 d culture 69

Figure 4-6: Viability of ATII cells after 2 d culture assessed by LIVE/DEAD fluorescent staining 70

Figure 4-7: Cytoskeletal organization of ATII cells after 2 d culture 71

Figure 4-8: Cell-cell junction formation of ATII cells after 2 d culture 72

Figure 5-1: Concept of sequentially pulsed delivery along three chambers in the array 83

Figure 5-2: Fully fabricated device loaded with colored dyes for visualization of chamber array and 3-D channel network 86

Figure 5-3: Cell segmentation 93

Figure 5-4: Simulation of chamber flow field during a flow pulse 96

Figure 5-5: Gradient formation and steady-state profiles measured via fluorescence imaging 98

Figure 5-6: Comparison of concentration profiles for numerical modeling and measured data 103

Figure 5-7: Variation in concentration profiles, chamber-to-chamber and device-to-device 106

Figure 5-8: Chemotactic index (CI) for positive control, negative controls, and experimental trials 109

Figure 5-9: CI from cell migration experiments by section 110

Figure 5-10: Speed, area, and circularity from cell migration experiments by section 111

Figure A-1: CAD layout of chamber array for soluble-matrix signaling 129

Figure A-2: CAD layout of chamber array for soluble gradient signaling 130

Figure B-1: Setup for chemotaxis experiments 131

Figure C-1: Integrated “push-up” PDMS valves 132

Figure D-1: Wafer-level view of stack for modified compression-molding fabrication process 133

Figure F-1: Transwell assays, testing response of cells (MDA-MB-231) to signals (FBS and EGF) 137

Figure G-1: Negative (left) and positive (right) controls compared to gradient trials 138

Figure H-1: Chemotactic index (CI) by time, stratified by spatial section of chamber 140

Figure H-2: Speed, area, and circularity by time, stratified by spatial section of chamber 141

SUMMARY

This work develops microfluidic technologies to advance the state-of-the-art in living cell-based assays. Current cell-based assay platforms are limited in their capabilities, particularly with respect to spatial and temporal control of external signaling factors, sample usage, and throughput. The emergence of highly quantitative, data-driven systems approaches to studying biology have added further challenges to develop assay technologies with greater throughput, content, and physiological relevance. The primary objectives of this research are to (i) develop a method to reliably fabricate 3-D flow networks and (ii) apply 3-D flow networks to the development and testing of microfluidic chamber arrays to query cellular response to soluble-matrix signal combinations and gradient signaling fields. An equally important objective is for the chamber arrays to be scaled efficiently for higher-throughput applications, which is another reason for 3-D flow networks.

Two prototype chamber arrays are designed, modeled, fabricated, and characterized. Furthermore, tests are performed wherein cells are introduced into the chambers and microenvironments are presented to elicit complex responses. Specifically, soluble-matrix signaling combinations and soluble signal gradients are presented. The study of complex biological processes necessitates improved assay techniques to control the microenvironment and increase throughput. Quantitative morphological, migrational, and fluorescence readouts, along with qualitative observations, suggest that the chamber arrays elicit responses; however further experiments are required to confirm specific phenotypes. The experiments provide initial proof-of-concept that the developed arrays can one day serve as effective and versatile screening platforms.

Understanding the integration of extracellular signals on complex cellular behaviors has significance in the study of embryonic development, tissue repair and

regeneration, and pathological conditions such as cancer. The microfluidic chamber arrays developed in this work could form the basis for enhanced assay platforms to perform massively parallel interrogation of complex signaling events upon living cells. This could lead to the rapid identification of synergistic and antagonistic signaling mechanisms that regulate complex behaviors. In addition, the same technology could be used to rapidly screen potential therapeutic compounds and identify suitable candidates to regulate pathological processes, such as cancer and fibrosis.

CHAPTER 1

INTRODUCTION

Challenges in Cell-Based Assays

Assaying the response of living cells to chemical and biomolecular stimuli is an essential activity in the life sciences and the pharmaceutical industry. Living cell-based assays are *in vitro* models consisting of (i) the cell(s) of interest and (ii) the environment (a.k.a. microenvironment) that surrounds the cells. Cell-based assays are performed in a variety of platforms, such as flasks, well plates, and microfluidic systems. The platform determines the manner in which the microenvironment can be manipulated, which in turn determines how well the assay mimics *in vivo* conditions while simultaneously providing a well-controlled environment. Because of the differences between *in vitro* and *in vivo* conditions, cells in assays tend to present a different phenotype from what they would in the tissue context; therefore, cellular behavior in such *in vitro* assays is often a poor predictor of behavior *in vivo*.[1] This limits the insightfulness of basic research and imparts a substantial economic cost to pharmaceutical development.[2,3] As a result, a major goal in the development of assay platforms is to provide new capabilities that improve the quality and control of the microenvironment. Ideally, such platforms would enable cell-based assays that emulate physiological, pathological or otherwise perturbed conditions, which elicit responses that are faithful representations of their *in vivo* counterparts.

There are also other important goals in assay development. Considerable efforts are being placed to increase parallelization (throughput),[1] increase data types (content),[4] and lower costs in cell-based assays. A key motivator in such efforts is the emergence of a more quantitative, data-driven systems approach to biological studies.[5,6] The systems approach poses a dramatic challenge to advance experimental and computational assay

tools.[7] Such tools will require massive experimental parallelization, automated data analysis, and the ability to convert complex questions from the systems viewpoint into functional experimental systems that closely reflect the relevant physiology and disease state.[8,9]

The need for high-throughput, high-content, and high-relevance screening tools is not only useful at the basic science level, but also an imperative in the pharmaceutical and biotechnology industries. In the development of new medicines, the rate-limiting step has shifted from target/early lead identification to cell-based assays. High-content screening platforms, usually in the form of well-plates with sophisticated image processing software, are regularly being used for live-cell imaging and data acquisition. Assay platforms that create microenvironments with greater predictive ability could reduce the risk in selecting candidate drugs and dramatically improve the drug development process, where costs increase exponentially into later stages of animal and human testing.[1]

Research Objectives

This work utilizes microfluidic technologies to address the challenges of cell-based assays. The microfluidic approach holds great potential for dramatically reduced sample usage and the creation of complex, previously unattainable microenvironments.[10] However, the networking of flow paths to address large-scale chamber arrays in microfluidic systems is difficult, as it ultimately requires multi-layer designs. Furthermore, if individual chamber addressing is required, inter-layer 3-D flow routing is necessary. This is especially the case for chambers arrayed in a 2-D grid, which is the hallmark of high-throughput experimental platforms.

The objectives of this research are to develop microfluidic chamber arrays that exhibit unique microenvironmental capabilities. These systems are designed to be scalable to larger, high-throughput arrays by the use of 3-D flow networks, which are

made possible by a novel fabrication process. The final objective is to test each system as a viable assay platform by eliciting complex cellular responses. Therefore, the technologies resulting from this work could be generalized for broader application. Overall, the key motivator of this work is the prospect of developing technologies that could dramatically improve the economics of cell-based assays and ultimately facilitate significant biological discoveries and more rapid drug discovery.

Objective 1: Develop a Reliable Method to Fabricate 3-D Flow Networks

The objective is to develop a process to fabricate 3-D flow networks with a yield that is acceptable for device design and testing. Previously developed methods are first tested as possible fabrication processes. Modifications are developed, involving focused pressures and alignment with partially cured PDMS, resulting in a modified compression-molding process. Yields are estimated, and a final process is adopted.

Objective 2: Design, Realize, and Test a Novel Chamber Array for Combinations of Matrix and Soluble Signals

The objective is to develop a continuously perfused, non-cross-contaminating microfluidic chamber array for studying cellular responses to orthogonal combinations of immobilized and soluble signals. This system is a prototype assay platform designed to exhibit the following novel combination of attributes: (i) continuous perfusion, (ii) flow paths that forbid cross-chamber contamination, and (iii) chamber shielding from direct perfusion to minimize shear-induced cell behavior. In addition, the system is designed to provide experimentalist with considerable versatility through four modes of operation. To confirm proper operation of the array, responses of rat-derived lung cells are observed under four pair-wise combinations of soluble and immobilized signaling molecules.

Objective 3: Design, Realize, and Test a Novel Chamber Array That Generates Soluble Signal Gradients

The objective is to develop a novel microfluidic chamber array to establish and modulate soluble gradients for chemotaxis studies. The system is a prototype assay platform designed to exhibit the following novel combination of microenvironmental features: (i) fully stable signal gradients, (ii) a shear-free microenvironment, (iii) gradient profiles approaching basal concentrations of zero, (iv) gradients switchable on-off without changing input flows, (v) gradient profiles whose curvature can be changed. In addition, the array is designed to exhibit robustness in the form of similar gradients in all chambers, a network architecture enabling efficient scale-out of the chamber array, and a fabrication process requiring only one alignment step. These features are enabled by a 3-D flow network. To test the platform, the migrational and morphological responses of human breast cancer cells to a serum gradient are measured. The intent is to highlight the utility of many features of the platform and show statistically significant differences between non-gradient and gradient conditions (both spatially and temporally).

CHAPTER 2

BACKGROUND

This chapter discusses cell signaling, combinatorial signaling fields, and two examples of cellular responses. Also, traditional and microfluidic *in vitro* cell-based screening tools are reviewed.

The focus of this research is on developing cell-based assay platforms that can present novel microenvironments in scalable chamber arrays. To validate that the platforms are effective assays, specific cellular responses must be elicited within them. The two representative responses that are elicited are epithelial-to-mesenchymal transition (EMT) and directed cell migration (chemotaxis). Therefore, this chapter briefly describes extracellular signaling and the microenvironment, and it discusses EMT in response to soluble and immobilized signal combinations and chemotaxis as a result of a soluble signal gradient. EMT and chemotaxis are complex phenomena, and greater understanding of these processes could lead to breakthroughs in medical treatment, particularly for cancer.

Signaling and the Microenvironment

In multicellular organisms, cells must communicate with each other in order to coordinate their behavior. By coordinating their behavior, cells work together to assure the well-being of the organism as a whole. Cells communicate with each other via extracellular signaling molecules (external signals), which are produced by cells and transported by various means to target cells. At the target cell, transmembrane receptor proteins bind to the external signal, which activates intracellular signaling pathways at various locations in the cell's interior. Propagation of the signal may be complex, involving many different types of intracellular signaling molecules working in series and

in parallel.[11] As a whole, signaling pathways can initiate, sustain or alter specific cell responses, such as growth, differentiation, apoptosis and migration.

External signals exist in both soluble and immobilized forms. In soluble form, external signals are dissolved in the fluid medium surrounding cells. Some examples of soluble external signals are growth factors, cytokines, and dissolved gases, such as epidermal growth factor (EGF, a regulator of cell growth, differentiation, and proliferation), interleukin-8 (IL-8, a molecule that attracts white blood cells), and nitric oxide (NO, a regulator of smooth muscle contraction), respectively. Immobilized external signals are comprised of molecules of the extracellular matrix (ECM) or proteins anchored to cell membranes. Examples of ECM molecules are proteoglycans, collagen, laminin, and fibronectin.[11]

The local environment surrounding each cell, or microenvironment, presents cells with a diverse array of external signals. The microenvironment consists of the fluid, ECM, and cells that are near to (or in direct contact with) the cell. Scores of external signals have been identified, and to a typical cell, each external signal can vary in space and time. In addition, external signals can exert their effect on cells either alone or in combination with other types of signals. An example of this is in embryonic development, where multiple signaling proteins dynamically segregate or overlap to form the body plan[12] and organs.[13]

Combinations of Multiple Signaling Fields

Understanding cellular response to multiple simultaneously-applied external signals is essential to gaining new insight into cellular responses. Current experimental platforms oftentimes do not fully recapitulate the microenvironment compared to *in vivo* conditions that are rich with chemical and physical signals. When a cell is subjected to many different types of external signals at once, it is subjected to a specific signaling

combination. External signaling combinations can exist as mixtures of soluble signals,[11] mixtures of soluble and immobilized signals[14] or mixtures of signal gradients.[15]

External signal combinations can act as switches to initiate basic cellular functions. Combinations of soluble and immobilized (ECM) external signals have been shown to facilitate and enhance cell growth, cell cycle regulation, and differentiation.[14,16-18] Such responses can come as a result of coupling between pathways emerging from growth factor receptors and integrins; for example, the pathways of epidermal growth factor (EGF) and platelet-derived growth factor (PDGF) receptors interact with the pathways of various integrins through Rho family GTPases, such as Cdc42, Rac, and Rho. These proteins share a number of target effectors that organize cytoskeletal structures, such as lamellipodia and stress fiber formation.[16]

Interestingly, external signal combinations can produce synergistic effects in diverse processes, where the cellular response may be greater than the summed contributions of each individual signal. Examples include ECM remodeling during inflammation[19,20] and modulation of synaptic strength during learning and memory formation.[21,22] Much more combinatorial experimentation of external signals will be required to understand the pathways that lead to additive, antagonistic or synergistic effects.

Gradient Signaling Fields

Concentration gradients exist when the concentration field of an external signal is non-uniform. Gradients of external signals act as directional cues for various cellular functions. Gradients establish the direction that cells migrate;[13,23] gradients also act as a graded field to assign different fates to stem cells at different concentrations within the field.[12] These functions in turn affect larger biological processes, such as wound healing, immune response, and embryonic development.[11] Combinations of external signal gradients have been shown to play important roles in organogenesis[15,24] and neural

mapping (and axon guidance)[25] For example, it has been shown that ephrin-A and ephrin-B form overlapping gradients that affect the guidance of retinal axons. Interestingly, they not only act as chemoattractants, but also act as chemorepellants, depending on the background concentration and receptor expression of nearby neurons.[26]

Also, gradient combinations affect the navigation of immune system cells.[27,28] Despite these observations, the study of signal gradients and their effect on cellular behavior is still a nascent field; many more discoveries will come about through more quantitative and controlled experimentation.

Two Examples of Cellular Response

This work attempts to elicit two types of cellular response; therefore, they are briefly described below. The first is epithelial-to-mesenchymal transition (EMT) in response to a soluble-immobilized signal combination, and the second is cell migration (chemotaxis) in response to a soluble chemoattractant gradient. A common link between EMT and chemotaxis is they are both observed in the context cancer metastasis, which is a complex, multi-step process.[11] EMT and chemotaxis are active fields of research with the potential for high impact discoveries, which could be facilitated by new assay technologies.

Epithelial-to-Mesenchymal Transition (EMT)

EMT is a major change in cellular phenotype, where a cell loses the morphology and gene expression pattern of a normal epithelial cell and instead takes the morphology and expression pattern of a typical mesenchymal cell. Epithelial cells form sheets that line cavities and ducts, and they are tightly connected by E-cadherin transmembrane protein junctions. In contrast, mesenchymal cells express N-cadherin, fibronectin, and vimentin (among other proteins) and display an elongated fibroblast-like morphology, as well as motility and invasiveness.[29] EMT is critical and beneficial to processes like

wound healing in adults[30] and morphogenesis in developing embryos,[31] where cells must migrate to close the gaps in wounds or position themselves during the modeling of tissue, respectively. Interestingly, it is highly suspected that metastatic cancer cells acquire their migrational and invasive characteristics not by genetic mutation, but instead by simply reactivating the EMT program that was pre-encoded for wound healing and developmental purposes.[29]

E-cadherin expression plays a critical role in the induction of EMT. E-cadherins expressed on the membranes of epithelial cells attach to each other, forming adherens junctions that provide mechanical tensile strength to hold the cells together in a sheet. Reduced expression of E-cadherin has been shown to cause changes associated with EMT, allowing cells to break away from the epithelial sheet and migrate.[32] In contrast, the expression of N-cadherin that comes as a result of EMT does not promote cell-cell adhesion, but instead causes the cells to have a greater affinity toward stromal cells (e.g. fibroblasts). Such behavior is implicated in the metastasis of cancer cells of epithelial origin, where the cells detach from the epithelial sheet and invade into the stroma.[33]

Signal Combinations and EMT

The causes of EMT are not well understood. Although, there is evidence that EMT is caused by various combinations of extracellular signals from the stroma, which could be soluble, immobilized or a combination of both.[34] In particular, transforming growth factor-β1 (TGF-β1) is highly-suspected as an extracellular signal for EMT.[35] Also, tumor necrosis factor-α (TNF-α), epidermal growth factor (EGF), hepatocyte growth factor (HGF), and insulin-like growth factor-1 (IGF) are possible causative signals, either acting alone or in combination.

Significance and Challenges of EMT Studies

EMT-related genes or protein products could provide new targets for cancer therapy, which makes the study of EMT particularly significant. The difficulty in understanding EMT (and possibly interfering with EMT in a rational way) is that it is likely caused by various combinations of signaling factors, each initiating EMT through different intracellular pathways. In addition, EMT is a reversible process in which cancer cells are thought to follow a progression through (i) onset of EMT, (ii) invasion into the stroma, (iii) intravasation into the bloodstream, (iv) transport through circulation, (v) extravasation into the stroma at a different site, (vi) colonization of a new tumor, and (vii) reversion to an epithelial phenotype via MET (mesenchymal-to-epithelial transition).[32] Simulating such events in time and space is difficult to perform *in vitro*; however, such difficulty becomes motivation for the development of more sophisticated assay platforms, which can be used to determine the effects of specific, well-controlled signaling combinations on the induction and possible arrest (and reversal) of EMT.

Cell Migration

Cell migration is a complex process in which cells integrate chemical and physical cues to determine how they will move. Included in those cues are multi-directional, overlapping, and time-varying external signaling fields. Cell migration is essential to many biological processes. For example, cell migration is required for animal development. During gastrulation, cells must migrate to relative to each other to create a gut.[36] To develop the nervous system, neural crest cells migrate over long distances (as long as meters) to construct and guide axons to their synaptic targets.[37] Also, cell migration is important in adult animals. White blood cells, such as macrophages and neutrophils, must chemotax towards infection sites to destroy foreign invaders.[38] Osteoclasts and osteoblasts migrate through bone to remodel and renew it.[39] Fibroblasts migrate to damaged connective tissue to repair it.[40] As well, epithelial cells of the intestine migrate in a controlled manner toward the tip of the villi to replace lost

cells.[41] From a pathological perspective, cancer cells must migrate to escape primary tumors and create new ones in other parts of the body (metastasis). Understanding the signaling pathways that govern cancer cell migration may lead to new targets for therapy.[42]

Basic Process of Cell Migration

Directed cell migration is induced by gradients of external signals. Two types of migration are chemotaxis and haptotaxis: chemotaxis, where a cell migrates up a concentration gradient of a soluble signal (a chemoattractant) and haptotaxis, where a cell migrates up a gradient of immobilized ECM proteins. In any case, cell migration begins when the cell senses a non-uniform concentration field and polarizes itself in the direction of the gradient. When a chemoattractant binds to its corresponding transmembrane receptor on the cell, the receptor becomes activated (by phosphorylation) and initiates a signaling pathway intracellularly.

Polarization occurs when a cell assumes an asymmetric morphology (when one can recognize a "front" and a "rear" to it). Once a cell is polarized, migration proceeds via four distinct activities: (i) extension (protrusion) of the cell membrane, (ii) formation of attachments between the substratum (i.e. ECM) and cell, (iii) contractile force and traction, and (iv) release of attachments.[43]

Protrusions

Two types of membrane extension are lamellipodia (two-dimensional, sheet-like) and filopodia (one-dimensional, spike-like).[11] Polymerization of the protein actin provides the protrusive force necessary to extend lamellipodia and filopodia outward from the leading edge of a migrating cell.

Focal Adhesions

Cell-substratum attachments, called focal adhesions (FAs), are formed at the leading edge of lamellipodia and filopodia to anchor the cell to the substratum. Focal adhesions are characterized by the clustering of integrins, which are cell membrane adhesion receptors that link ECM proteins on the cell's exterior to the cytoskeleton in the cell's interior. Focal adhesions are also characterized by the co-localization of several proteins (e.g. focal adhesion kinase (FAK), talin, paxillin, and vinculin) to the FA site that are all implicated in FA formation.[43]

Contraction

Contractile forces are generated by myosin motor proteins. The contractile force is countered by the traction force of FAs with the substratum. The traction force is transmitted through anchor proteins, such as vinculin and talin, which provide the mechanical linkage between integrins and the actin filaments. As a result, a net forward force is generated, causing cell movement.[44]

Release

Throughout the process of migration, actin filaments and FAs disassemble in the rear of the cell as they are constructed in the front;[45] this process is known as "treadmilling." Thus, while a migrating cell moves relative to the substratum, actin filaments and FAs are fixed. Calcium (Ca^{2+}) facilitates the process.[46]

The migration speed of cells is shown to be dependent upon substratum ECM concentration, integrin expression levels, and integrin-ECM binding affinity.[47] Various combinations that counter-balance the three factors will achieve a maximum migration speed. Migration speeds vary depending upon cell type. While a fibroblast migrates at roughly 1 μm/min, a neutrophil can migrate up to 20 μm/min.[48]

<u>Significance and Difficulty in Cell Migration Studies</u>

Our knowledge of the molecular aspects of cell migration is still in the early stages, and many studies yield conflicting conclusions,[49-51] which indicates that more subtle and complex roles for migratory proteins may yet be discovered. As well, despite many advances in our understanding of cell migration in general, many unanswered questions remain. Many of these questions involve the temporal and spatial regulation of intracellular signaling molecules, as well as the morphological and migratory readouts, in response to more precisely-controlled external signaling conditions.[44]

Literature points to a number of knowledge gaps that present major challenges in our knowledge of cell migration:[43,44,52,53] how cells establish and maintain a polarized state, how FAs form and disassemble, how cells recognize their targets, and how spatially and temporally segregated molecular interactions are integrated into a coherent migratory decision-making process. One way to elucidate the interactions between different signaling pathways is to engage more than one pathway simultaneously. The technologies developed in this research will enable the simultaneous generation of multiple, overlapping external signal gradients. By doing so, different types of cell surface receptors will be activated, which then initiate different intracellular signaling pathways.

An interesting line of inquiry is to apply the external signal gradients from different directions. Thus, not only will different signaling pathways be initiated, but also they could be initiated in different locations within the cell. Such conditions will facilitate probing the cellular decision-making process when multiple chemoattractant gradients (and the induced signaling pathways) compete with each other. Furthermore, by time-varying the gradients, temporal characteristics could be observed, such as the speed at which signaling molecules become activated or expressed, as well as how fast they spatially distribute themselves within the cell.

This combinatorial approach is likely to expand our knowledge of how migrational decisions are made, as well as how to identify or predict them from

movement, morphological, and biomolecular readouts. Eventually, the systematic investigation of multiple signaling pathways may lead to the discovery of new integrating molecules (or complexes) or the discovery new functions of known molecules.

In Vitro Screening Tools

The general aspects of cell-based assay platforms are reviewed, beginning with traditional and microfluidic platforms, and then briefly discussing combinatorial signaling platforms and gradient platforms. Specific aspects, as they relate to the devices of this work, are addressed in Chapters 4 and 5.

Traditional Screening Platforms

Control of the *in vitro* microenvironment has been achieved using culture dishes and multi-well plates for over 100 years. These tools have facilitated many spectacular discoveries; however, their use as cellular assay platforms is limited in a number of respects. Principal among these limitations is the inability to quantitatively control spatial and temporal alterations in the cellular microenvironment using standard culture plates (or modifications thereof).[54] This lack of spatio-temporal resolution stems from the difficulty in implementing structures and fluid patterns on the cellular scale using standard methods.

Over the past decade, high-throughput screening systems have been developed as DNA (or protein) microarrays, flow cytometry systems, chromatography and spectroscopy systems, and high-density well plates for ligand binding affinity screens. However, time course measurements of living cells in response to a stimuli or combinations thereof are still commonly performed in well plates. Therefore, traditional cell-based assays continue to face substantial limitations in the form of high cost due to cell and sample usage, as well as technical difficulties like evaporation, which can cause well-to-well growth and phenotype variability.

Microfluidic Systems

Microfluidics has emerged with the potential to overcome many limitations of traditional methods. Microfluidics is the science and technology of systems that flow and manipulate very small amounts of fluids using channels with dimensions of tens to hundreds of micrometers.[55,56] Much of the inspiration for microfluidics is derived from the experience of the microelectronics industry. The invention of the integrated circuit (IC) led to the large-scale automation of computations, fundamentally changing the way people live and work. In turn, microfluidics researchers are investigating whether the automation of chemistry and biology will lead to equally fundamental impacts to science, industry, and society. A major catalyst for microfluidics research came in the 1990s through Defense Advanced Research Projects Agency (DARPA) programs aimed at developing microfluidic systems to serve as detectors for chemical and biological weapons. Since then, microfluidics has grown rapidly and established itself as a distinct research field.

Microfluidics takes advantage of physical phenomena that dominate as systems are scaled from the macro- to micro-scale. One of these is low Reynolds number flow. The Reynolds number (Re) is a dimensionless parameter that compares the viscous and inertial effects in a fluid flow stream through the following relationship,

$$\mathrm{Re} = \frac{\rho U_0 L_0}{\eta} \ (=) \ \frac{inertial}{viscous},$$

where ρ is the fluid mass density, U_0 is the flow speed, L_0 is the characteristic length of the system, and η is the fluid viscosity. In microfluidic systems, the characteristic length is dramatically reduced compared to that of macro-scale systems. The dominance of viscous effects leads to two main results. First, low Re flow is strictly laminar, which makes fluid flows predictable and stable. Second, because of the absence of turbulent

flow, mixing occurs almost exclusively by Brownian diffusion. This enables engineers to numerically simulate microfluidic systems to speed the device prototyping process.

Because of their small size, microfluidic systems have the potential for extremely low sample usage, which is essential for screening with rare compounds or small numbers of primary cells. The size of microfluidic systems also enables them to better mimic the cellular microenvironment (compared to flasks and well plates), since the high surface-to-volume ratio is a better match for those of interstitial spaces and capillaries in the body.

Microfluidic systems have enabled some remarkable studies in the life sciences. For instance, parallel laminar flow streams loaded with different factors have been used to probe localized response and internal diffusion in a cell as it straddles the interface of the two streams loaded with different stimuli.[57-59] Also, large-scale integration through an array of individually-addressable chambers, channels, and valves has demonstrated the potential for highly automated microfluidic devices.[60] Many reviews discuss the considerable efforts of those who apply microfluidics to biology.[10,54,56,61,62]

Tools for Combinations of Multiple, Overlapping Signaling Fields

The customary way to combine uniformly-distributed signaling fields is simply to include the signals of interest in a culture medium, which is then used to immerse cells in a culture well. Recently, the focus upon systems biology and the need for higher-throughput tools has led to arraying techniques (not microfluidic) to scan through multiple signaling conditions in parallel.

For example, Flaim *et al.*[63] developed a technique to study the response of cells attached to different combinations of immobilized ECM proteins. They deposited a 32-spot array of different mixtures of five ECM proteins (fibronectin, laminin, collagen I, collagen III, and collagen IV) on the surface of an acrylamide gel and then seeded cells on each spot to observe each combination's effect on differentiation. Soen *et al.*[64]

developed a method to generate an array of spots on a glass slide that included not only ECM proteins, but also cell surface molecules (CAMs) and soluble external signals. They used the array to observe the effect of different signaling combinations on the differentiation of neural precursor cells.

Although array-based techniques offer the advantage of high throughput, a major limitation is that the external signals cannot be varied in time. In addition, the spot-making techniques immobilize signals to a surface. For signals that naturally occur as soluble proteins, their immobilization to a surface may lead to a physiologically irrelevant condition.

Tools for Gradient Signaling Fields

Traditional methods to generate gradients of signals are the Boyden chamber,[65] Dunn chamber,[66] and under-agarose assay,[67] which are all used for cell migration studies. The three methods are variants of a similar strategy: a soluble signal is introduced to a source on one side of a chamber and allowed to diffuse to the other side of the chamber, establishing a gradient. Cells seeded within the well or chamber then respond to the gradient.

The main disadvantage of the traditional methods is that the source of the signal is non-replenishing and the concentration sink on the other side of the diffusion bridge is not fixed at a constant concentration. Thus, the gradient continually decays into a uniform concentration field, which leads to two problems for analysis. First, since the gradient is decaying, it is difficult to know exactly which gradient (and background concentration) is affecting the cells. Second, for slow-moving cells (e.g. fibroblasts), the gradient may decay to equilibrium before any appreciable observation can be made.[48]

To address these issues, the Whitesides group developed a groundbreaking microfluidic technique to produce stable gradients.[68] In these systems, two input streams of different signal concentrations are fed into a branching array of channels that undergo

multiple generations of splitting and recombining the flows. The resulting output is a set of several parallel laminar streams, each with a slightly different concentration. Brownian diffusion between the streams causes enough blending to produce a continuous concentration profile with a stable gradient. Split-and-recombine systems have been used to study cell migration,[69-72] study neural stem cell differentiation,[73] and generate multiple concentration conditions for parallel cell culture systems.[74,75] A significant limitation of the split-and-recombine technique is that fluid flow must pass directly over cells to establish gradients. The resulting shear stress upon the cells has been shown to bias the direction of cell movement, so that cells begin to migrate in the direction of flow.[76] In addition, flow-induced shear stress in microfluidic systems can induce Ca^{2+} fluxes within cells, indicating that typical microfluidic flow rates could activate unintended intracellular signaling pathways.[77]

With respect to multiple, overlapping gradients, the under-agarose method can be modified to include multiple source reservoirs. Use of this modification has led to remarkable discoveries in signal integration and memory in leukocyte migration;[27,28] still, the method suffers from lack of temporal control and an unstable, decaying gradient. To produce quasi-stable overlapping gradients, a microfluidic multi-injector has been developed, where valves control the pulsatile release of signals into a stagnant chamber.[78] The drawback is that the chamber must be large enough to approximate an infinite reservoir; ultimately, the gradient and background concentration de-stabilize as the chamber fills with the molecules of interest, since it is not replenished with low concentration medium. Also, because the system does not periodically replenish with fresh medium, cells in the chamber may become nutrient-deprived. Two fully-stable opposing gradients have successfully been generated using the split-and-recombine technique.[79] However, the gradients are limited to the direction perpendicular to flow, precluding multi-directional studies.

It is difficult to vary signals in time because it requires the mixing and/or replacement of multiple signal sources to produce the desired signal concentration. Temporal variation of signals is useful to enable within-trial controls (between non-stimulus and stimulus conditions) and to determine the time constants for cellular response and adaptation. Using conventional means, one way to cause a signal change is to simply change the medium in the culture plate. Although straightforward, it requires the preparation of multiple solutions and the changing speed is limited by the speed at which a person or robot can remove and replace media.

Microfluidic approaches have led to some improvements. Fast switching between two gradients has been achieved by integrating two Christmas tree architectures.[80] This arrangement enables fast changes between two conditions, but it is limited in three respects: (i) gradients are limited to two directions, (ii) flows induce shear stress on cells, and (iii) inclusion of more than two gradients requires more space on the chip. To provide a continuum of gradients without occupying more chip space, Lin *et al.*[81] used an on-chip "mixing module" to mix source streams into arbitrary compositions. While this system allows for more concentration levels, it relies upon changes in flow rate at the sources to effect temporal changes. Given the volume of tubing leading from the syringe pump to the chip, changing the flow rate at the source would introduce a significant delay upon changing. Chen *et al.*[82] realized high resolution, time-varying concentration control within a single device by developing on-chip serial dilution networks. The advantage is that one could switch among 16 different concentration levels (4-bit) at any moment without altering the external flow sources; the limitation is that the fluidic network is extremely complex and occupies significant space on the chip.

Needs Addressed

This research focuses on the need for new technologies to enable the scale-out of microfluidic chamber arrays to realize their potential as high-throughput screening tools.

Advances are needed to improve the versatility, microenvironment, and scalability of arrays that screen soluble-matrix combinations. Versatility can be achieved by making the chambers individually addressable, and microfluidic perfusion cultures can benefit by reducing shear stresses (for cell types not physiologically exposed to shear). For gradient signaling, improvement is needed in scalability, as well as creating a microenvironment that combines low shear, low background concentrations, and stable gradients (for better experimental control), which has been difficult for researchers to achieve. A challenge in both tasks is to develop a reliable (and reasonably simple) fabrication process to manufacture the intricate devices required, which is the subject of the following chapter.

CHAPTER 3

FABRICATION OF 3-DIMENSIONAL FLOW NETWORKS

An important goal of this work is to develop microfluidic assay platforms that are conveniently scalable to high-throughput chamber arrays. This requires flow networks that can navigate through the interstices of the array to address rows, columns or individual chambers. To construct such complex flow networks, a fabrication process is developed that realizes through-holes between flow layers in a reliable manner.

3-Dimensional Flow Networks

Most PDMS microfluidic devices consist of a single layer, where flows travel 2-dimensionally. When there is more than one layer, the device is typically fabricated using multilayer soft lithography,[83] which results in layers that are fluidically isolated from each other. Each layer serves as either a layer for flow or a layer for integrated valves. It is also possible to realize 3-dimensional (3-D) flow networks, where flows travel out-of-plane from layer to layer. This enables greater design flexibility and more efficient use of device real estate.

As microfluidic chamber arrays are scaled to higher-throughput formats, 3-D flows become increasingly necessary to deliver fluids to and from chambers. Flow streams may need to occasionally navigate over (or under) other flow streams as they travel through the array. The result is a microfluidic channel network with three-dimensional flows that resemble roadway bridges and underpasses.

A number of methods have demonstrated the construction of 3-D flow networks. One method utilizes photoresist posts that protrude through a layer of PDMS that is coated on the mold.[84] The channels of a second layer of PDMS (usually a thick slab) are then aligned to the posts and the assembly is cured and detached from the mold.

Fabrication attempts based upon the protrusion method are detailed in the following section. Other methods use thin PDMS membranes that are perforated[85] or patterned[86] with through-holes and bonded between thick PDMS slabs. Although reliable at forming through-holes, these methods are designed to join thick slabs (order of mm) of PDMS; therefore, the use of high-magnification objectives with small working distances to observe specimens in the device is not permitted.

Kim *et al*.[87] developed a method to realize 3-D flow networks by compressing PDMS between multilayer photoresist patterns. The compression displaces PDMS from the tops of photoresist features, realizing through holes. Folch *et al*.[88] developed a similar compression-molding technique. A distinct advantage of such methods is that they do not require the alignment of thin PDMS membranes, which easily fold and stretch, making alignment difficult. In this work, a compression-molding technique is developed, which is modified from the works of Kim *et al.*[87] and Folch *et al.*[88] In the following sections, the development process is discussed and the final process is detailed.

Process Development

The fabrication of 3-D flow networks requires the creation of through-holes to permit inter-layer flows. In this case, through-holes are created in multi-layer PDMS devices. The development of the fabrication process involves four approaches to arrive at the final process. The four approaches are detailed below, highlighting the learning gained from each.

Protrusion Method: Attempts and Learning

The protrusion method for fabricating through-holes in PDMS involves spin coating a layer of PDMS onto a master (Si wafer) with photoresist forming channel features and (taller) posts on top of the channel features (see Fig. 5-1). The PDMS is spun to a thickness smaller than the height of the posts but greater than the height of the

channel features. Therefore, the photoresist post protrudes through the top surface of the PDMS. After the PDMS is cured, a second layer of PDMS is aligned and bonded to the first layer, and the bonded assembly is peeled off the Si wafer and bonded to a glass slide or cover slip. The protrusion method was developed by Kartalov *et al*.[84]

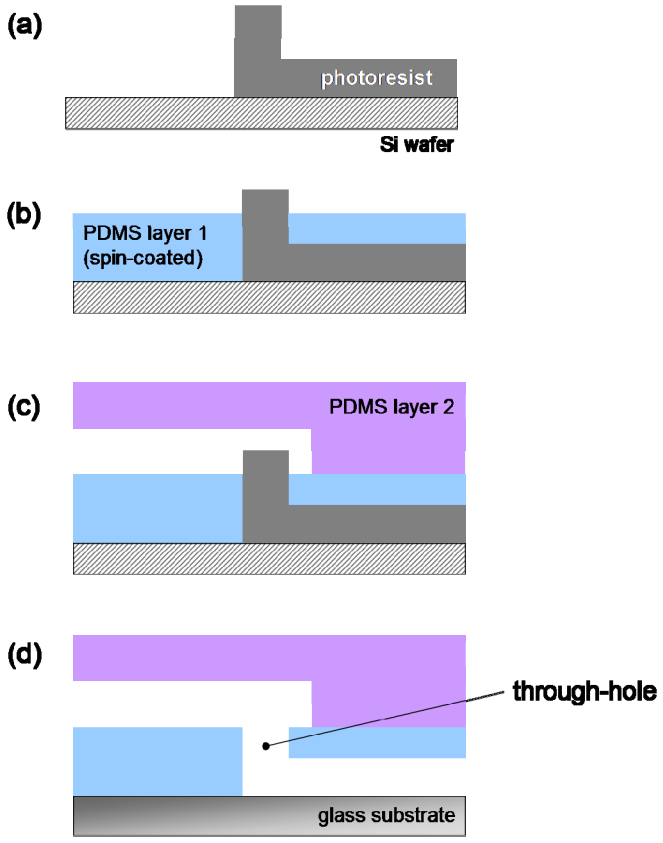

Fig. 3-1 Illustration of protrusion fabrication process. (a) Channel (lower) and post (upper) layers of photoresist (SU-8) are patterned on a Si wafer. (b) PDMS is spin-coated onto the wafer; the photoresist post protrudes above the PDMS surface. (c) A second PDMS layer is bonded to the first layer (usually a thick slab for mechanical support). (d) The two bonded layers of PDMS are peeled off the wafer and bonded to a glass substrate. A through-hole is realized in the location of the photoresist post. Adapted from Kartalov *et al*.[84]

In this work, the protrusion method was first attempted as a means to create 3-D flow networks because, in concept, it offers the convenience of not requiring any additional equipment or fixturing. The process could be performed on already available spin coaters. The process was first attempted by spin coating PDMS (20:1 prepolymer-

to-crosslinking agent) to a thickness of 30 μm onto test wafers with SU-8 (MicroChem Corp., Newton, MA, USA) photoresist patterns (57 μm tall); the PDMS was then allowed to cure. The objective was to see if SU-8 features would protrude above the surface of the PDMS. Scanning electron micrographs were imaged to view the test pieces at an angle from which it could be determined if protrusions were realized (Fig. 3-2). The images show the SU-8 features outlined against the surface of the PDMS. More notably, the PDMS appears to have a curved surface profile.

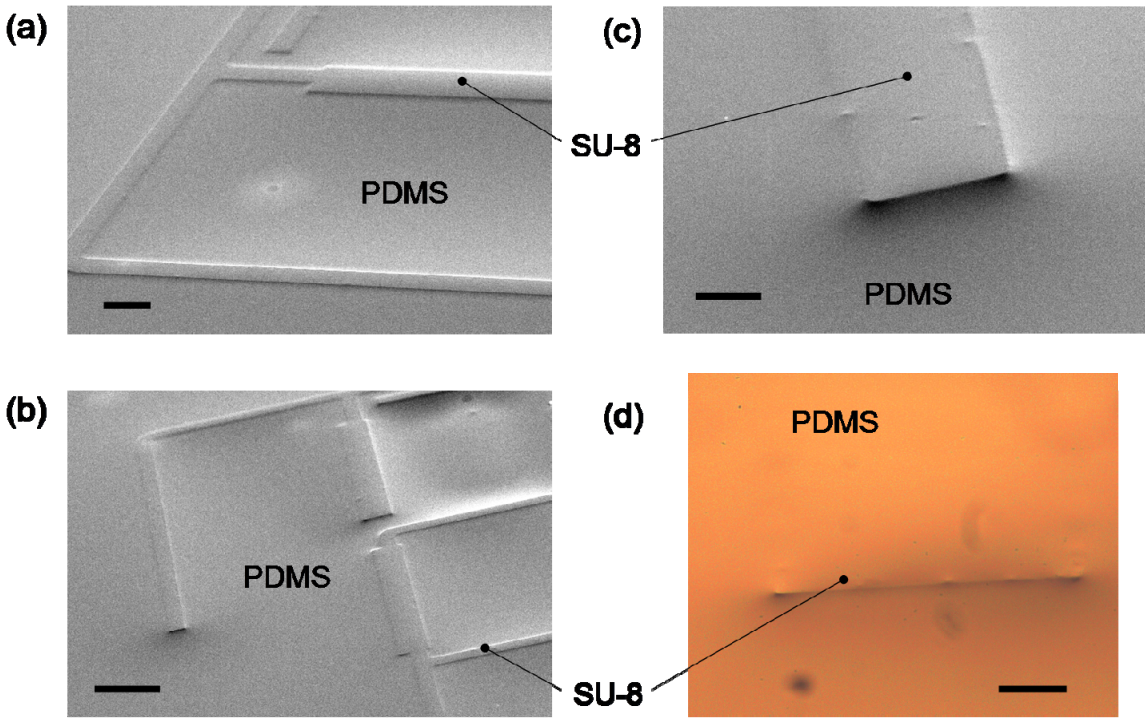

Fig. 3-2 Images of PDMS spin coated on SU-8 features. SEM images ((a)-(c)) show SU-8 test features outlined against PDMS ((c) is zoom of feature in (b)). Shadowing indicates curvature in PDMS thickness profile. (d) Stereo-zoom microscope image of PDMS and rectangular SU-8 feature; shadowing also indicating curvature in PDMS profile. Scale bar 200 μm in (a), 50 μm in (c), and 500 μm in (b) and (d). SU-8 thickness 57 μm; nominal PDMS thickness 30 μm away from SU-8 features and wafer edge bead.

The curvature in PDMS thickness profile was unexpected, as it was not thoroughly addressed in previous work.[84] One possible parameter that could affect the PDMS curvature is the relaxation time given after the spinning step prior to cure. A longer relaxation time would presumably allow the PDMS film more time to reduce in stress and

"flatten-out," forming a more planar surface. However, trials with relaxation times varying between 25 min and 24 hours showed no visible changes in profile. Another possibility is that the curvature could be due to wetting based on surface tensions. PDMS could exhibit low contact angle spreading on epoxies (like SU-8).

Based on the images, the PDMS surface curves nearly to the top of the SU-8 features (most noticeably in Fig. 3-2(b-d)). Because the devices in this work are intended to have channels as low as 7 μm tall, the protrusion process could produce sloped PDMS at each through-hole, which could interfere with proper bonding between layers or disrupt the flow fields of fluids traveling through the channels. These putative failure modes are diagramed in Fig. 3-3. It is also unclear whether a thin layer of PDMS remained on top of the SU-8 features, which could complicate through-hole production. Based on such reasoning, a different method was pursued with the intention of producing a completely flat (planar) surface of PDMS.

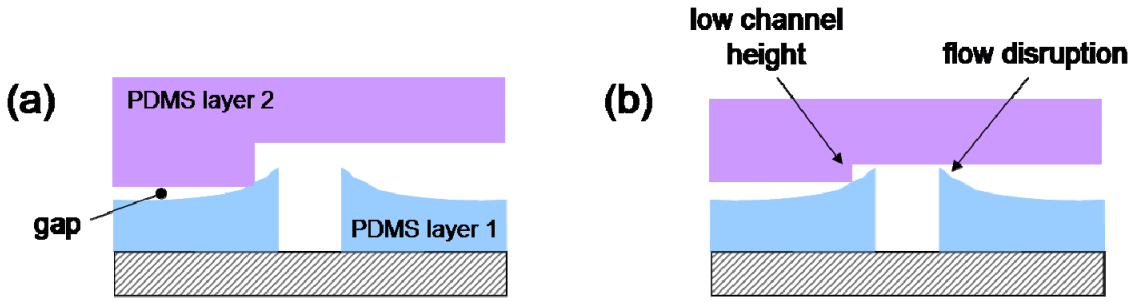

Fig. 3-3 Putative failure modes of protrusion method. (a) Curvature in lower PDMS layer could interfere with proper bonding by forming a gap between PDMS layers, resulting in feature warpage (residual strain) if bond is realized or leakage due to an unrealized bond. (b) For low channel heights (devices in this work utilize channel heights as low as 7 μm), the peak of the curved PDMS profile could disrupt the flow field and change the hydraulic resistance of the channel, as well as interfere with bonding.

The main learning from protrusion process attempts is the observation of the PDMS surface curving upward as it approaches SU-8 features; wetting characteristics could affect fabrication, especially for low channel heights (as previously mentioned). It is worth mentioning that one possible way to reduce PDMS curvature/wetting would be to chemically modify the surface of the SU-8 (e.g. silanization) to increase the contact

angle. This was not pursued, given initial successes with the compression-molding process discussed in the next section.

Compression-Molding: Attempts and Learning

A compression-molding process to realize through-holes was pursued in-parallel with the protrusion method. The compression-molding process begins by spin coating PDMS onto a master mold, which is a Si wafer patterned with photoresist (SU-8) in two layers. The upper layer features define the through-holes (similar to the photoresist posts in the protrusion method). The PDMS is coated thicker than both photoresist layers, and a transparency is laminated to the surface of the PDMS. Pressure is applied by adding weight to (or clamping) rigid plates, displacing PDMS from the top surfaces of the upper photoresist layer and forming a planar PDMS surface. Finally, a second PDMS layer is aligned and bonded to the first layer, and the bonded assembly is detached from the master and bonded to a glass substrate. This method is similar to the techniques described by Folch *et al*.[88] and Kim *et al*.[87] and is diagrammed in Fig. 3-4.

The primary rationale for pursuing the compression-molding process was the potential to realize a planar surface on the first PDMS layer upon which a second PDMS layer could then be intimately bonded. By realizing a planar surface, bonding problems associated with the protrusion method could potentially be avoided and low channel heights could be enabled in the second PDMS layer (per Fig. 3-3).

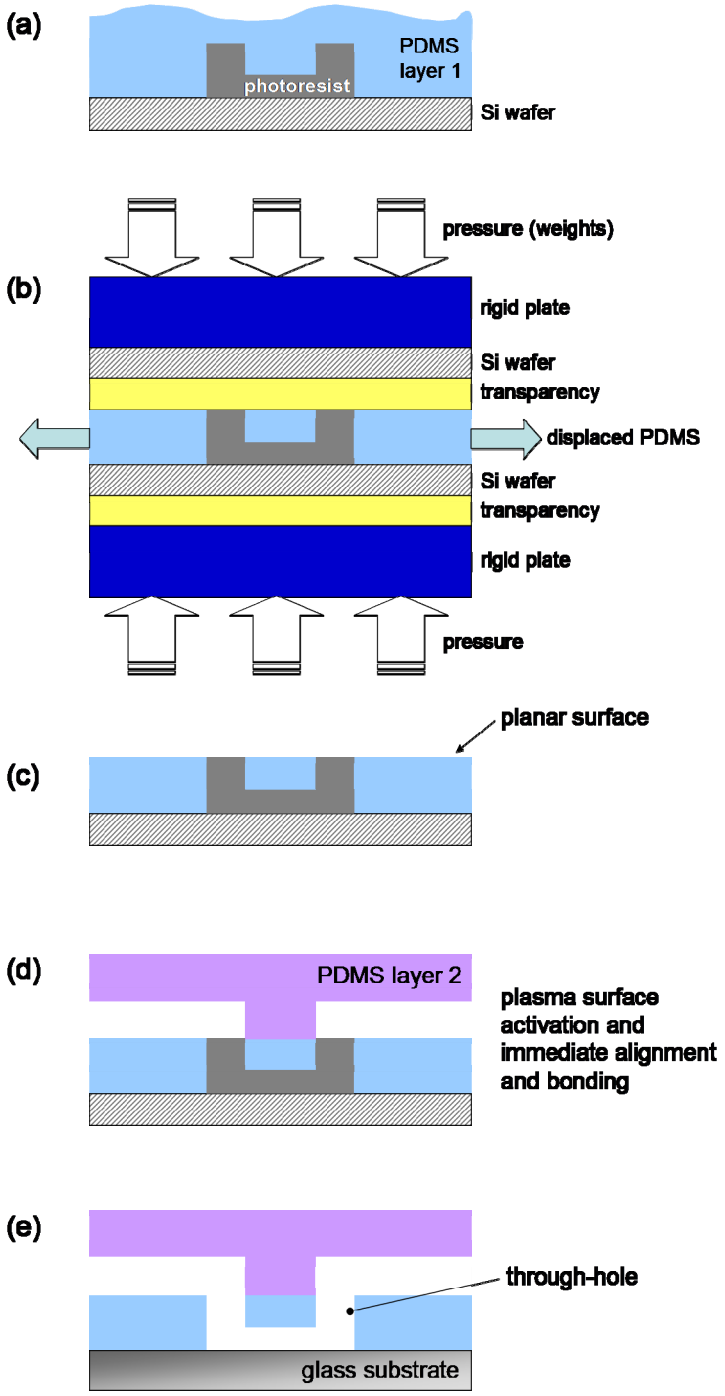

Fig. 3-4 Compression-molding process in summary. (a) PDMS is coated thicker than a two-layer photoresist stack. (b) A transparency is laminated to the PDMS surface, and an assembly of transparencies, Si wafers, and rigid plates is stacked; weight is used to apply pressure to displace PDMS from the top surfaces of the upper PDMS layer. PDMS is fully cured by heating. (c) Stack is disassembled and transparency is delaminated from the cured PDMS surface; a planar surface should result. (d) A second PDMS layer (i.e. thick slab pre-molded with channel network) is aligned and bonded to the first layer. Bonding is achieved by plasma surface activating both layers; as a result, alignment and bonding must occur rapidly (< 1 min). (e) Bonded layers are detached from master and bonded (by plasma surface activation) to a glass substrate. Subfigure (b) adapted from Kim *et al.*[87]

The process was debugged over the course of 20 trials on masters patterned with SU-8 layers with thicknesses of 50 μm and 30 μm for the lower and upper layers, respectively (total stack height being 80 μm, the sum of both). All devices in this work are based on such thicknesses. Several processing parameters were debugged throughout the trials, including but not limited to the relaxation time after PDMS spin coat, transparency lamination method, silanization time for laminated transparencies to assist in delamination from PDMS, assembly stacking method (to prevent slippage), and intermediate steps. All processing parameters are listed in the final modified compression-molding discussion in a later section of this chapter.

The critical learning from compression-molding process development took place in three respects: (i) use of photoresist support posts, (ii) prevention of gas bubble formation during compression, and (iii) thermal processing to enable alignment reworking. While a planar surface is in-principle possible with the compression-molding process, in practice the compliance and softness of the transparencies causes the displacement of PDMS from both upper and lower photoresist surfaces, resulting in a PDMS surface that generally conforms to the topography of the photoresist features. In many cases, the PDMS would be completely displaced from the surface of lower photoresist features, which caused unintentional fluidic interconnect with upper channels when crossing over the lower features. To prevent such interlayer leakage and assure a planar surface, photoresist support posts were integrated into device layouts (Fig. 3-5). Support posts are positioned throughout each device, and for critical locations, where a lower channel crosses an upper channel, support posts are placed between 150 and 300 μm from the crossing point to assure unintentional interconnect does not occur (Fig. 3-5(c)). The use of support posts makes possible a near-planar PDMS surface, enabling intimate bonding between the two PDMS layers without interlayer leakage.

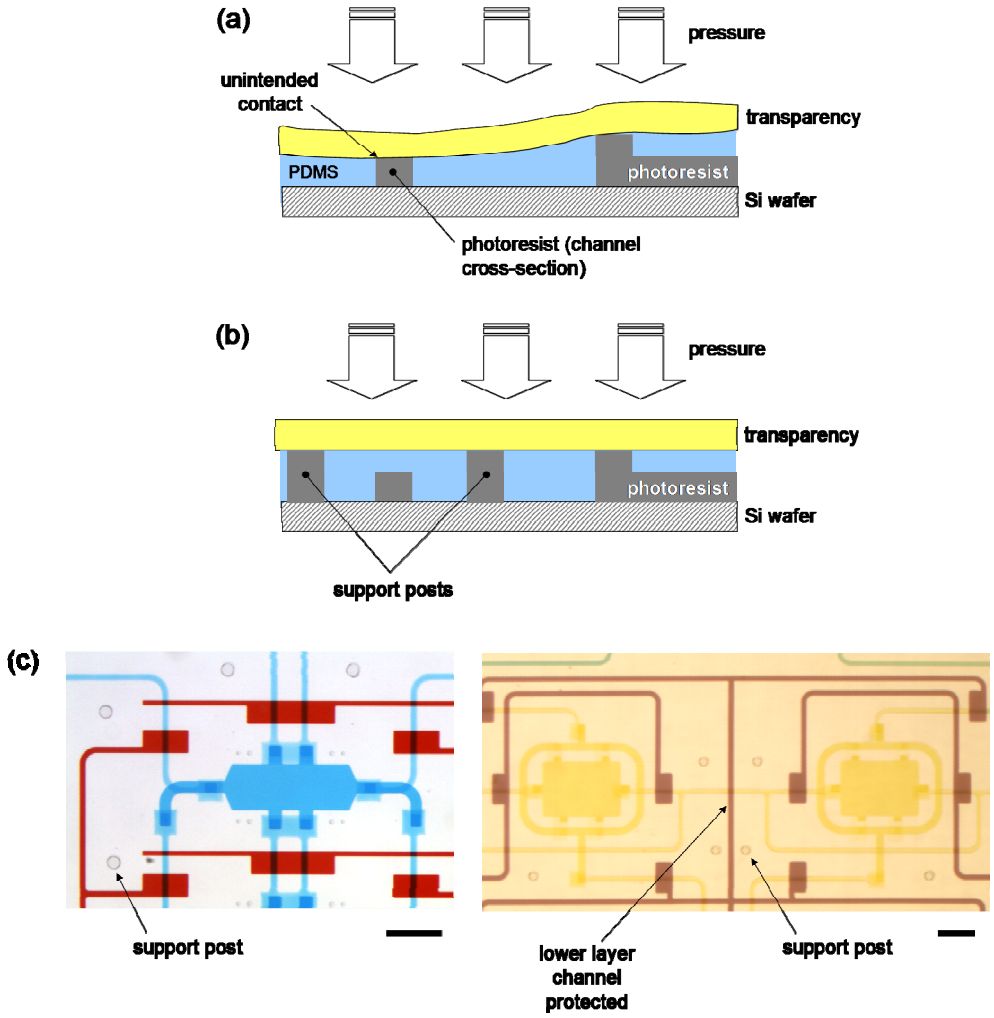

Fig. 3-5 Photoresist support posts. (a) Compliance of transparency causes it to conform to the topography of the tops surfaces of lower and upper photoresist layers when compression takes place. Loss of planarity causes unintentional fluidic interconnect between layers when lower and upper channels cross; results in device failure. (b) Support posts prevent transparency from collapsing on lower photoresist layer. (c) Support posts (small circular features) in devices developed in this work. Scale bar in both panels is 500 μm.

The prevention of gas bubble formation during the compression step is another important learning from this work. In initial trials, transparencies would be laminated to the PDMS surface, taking care not to trap air bubbles; however, numerous gas bubbles would nucleate throughout the device during compression (Fig. 3-6). Such bubbles would merge with through-hole features or cause unintentional fluidic interconnect between layers. One aspect of the compression process is that heat is applied to cure the PDMS. Assuming that uncured PDMS behaves as most liquids, the solubility of

dissolved air in PDMS would decrease as heat is applied, increasing the likelihood of bubble formation. Therefore, prior to processing, PDMS was placed in a vacuum desiccator for 2 hours at ~30 torr to remove dissolved air. This is roughly 4× longer than the typical degassing process to remove large, visible bubbles PDMS prior to casting it in non-compression processes. The extended degassing step effectively ended bubble formation during compression.

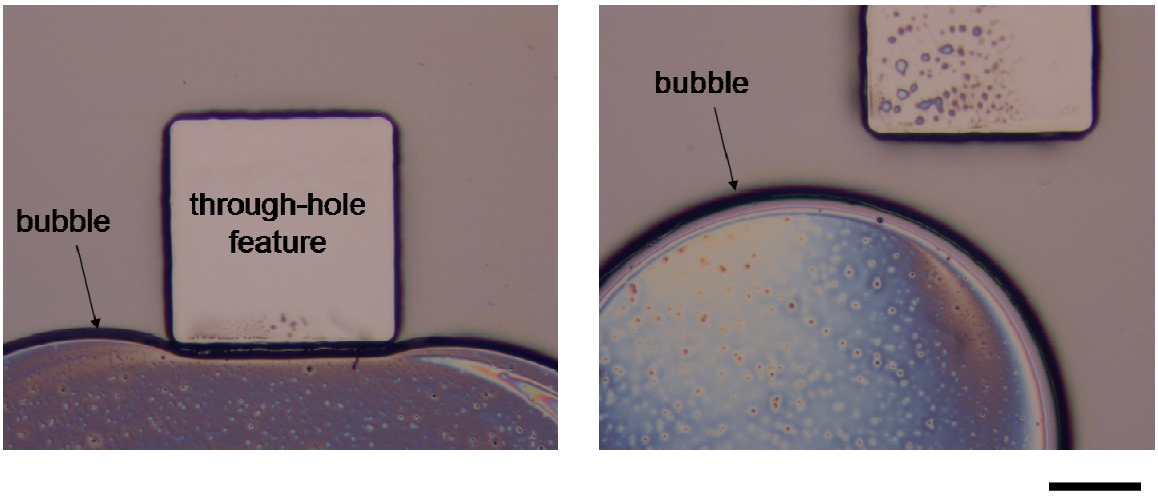

Fig. 3-6 Gas bubbles nucleated in PDMS during compression. Gas bubble nucleation was a major failure mechanism during process development. Subfigures show gas bubbles merging with a through-hole feature (left) and near a through-hole feature (right). Scale bar is 200 μm for both subfigures.

Another learning is the necessity of permitting reworks during alignment and bonding of the two PDMS layers. The prior mentioned work by Kim *et al*.[87] utilized plasma surface activation to bond both layers. Plasma surface activation enables robust covalent bonding between layers; however, the alignment and bond must be completed within 1 min prior to surface oxidation, and the alignment is a "one-shot" event. If the alignment is outside of tolerance, no rework could take place. Alignment time can be extended by immersion of PDMS surfaces in solvents (e.g. ethanol) immediately after plasma activation to shield the surfaces from oxidation. However, from a practical standpoint, the devices in this work were fabricated in batches (7 die per wafer), and if

the wafer was immersed in ethanol after plasma activation, it would likely require the stereo-zoom microscope (used for alignment) to be placed in a highly ventilated environment (e.g. fume hood) due to ethanol vapors emitting from the dish in which the wafer was immersed. Most importantly, since alignment is manual, the ability to rework (peel-off and align again) is important to yield more devices per batch.

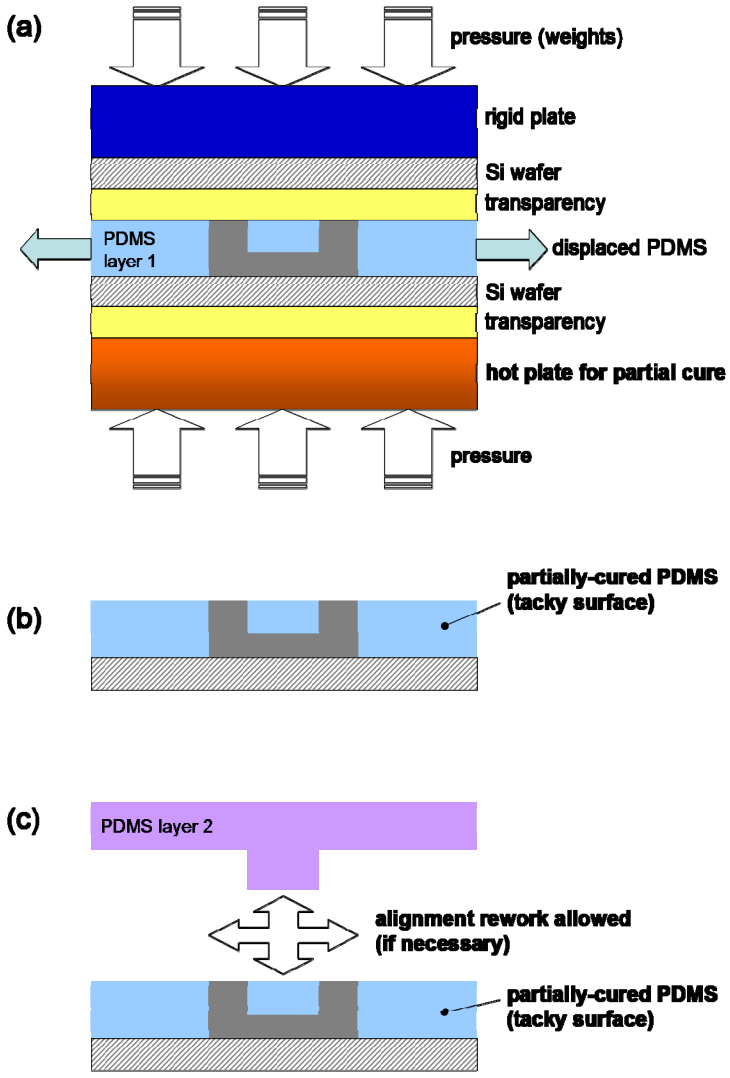

Fig. 3-7 Partial curing of PDMS during compression-molding. Typically, compression-molding involves heating the stacked assembly in (a) in an oven or on a hot plate until the PDMS is fully cured; there is no time limit in the heating process. The tradeoff is that alignment must be rapid (<1 min) and reworks are not possible during alignment. In this work, the heating schedule is set to partially cure PDMS into a solid but tacky surface, providing extra time for alignments and enabling reworks if necessary ((b) and (c)). The layers are then thermally bonded. Rework is useful to maintain yield in manual alignments, and the additional time could be beneficial for automated alignments of large batches of devices per master.

To make reworking possible, the PDMS in both layers was partially cured to the point where they were intact, yet tacky to the touch. To do so, the stacked assembly of transparencies and weights on the lower PDMS layer was placed on a hot plate for a limited time, which was determined to be 10.5 min at 80 °C after some trials of optimization. Partial curing of PDMS is a nonlinear process in time; thus, heating for slightly longer than necessary yields a fully cured PDMS surface that cannot thermally bond with the other layer. On the other hand, heating for too short a time results in still-liquid (mostly-uncured) PDMS, which does not have the mechanical rigidity for successful delamination of the transparency and aligning. Once removed from the hot plate, PDMS cures slowly at room temperature, and the alignment process could proceed without time limitation. If an alignment was out of tolerance, the two sticky PDMS surfaces could be carefully peeled apart, and re-aligned. For manual alignments in this work, x- and y-tolerances were set to ± 50 μm. After aligning all devices, further heating (12 hr at 70 °C) would thermally bond both layers into a single monolithic slab. Typically, in the final process, 2 devices per batch required rework (re-alignment). The average yield up to the alignment step was 4 to 5 devices (out of 7 attempted). Thus, reworking enabled up to a doubling of yield, when compared to a scenario where no rework was possible.

Despite the learning from compression-molding process development, batch yields were less than 1 device out of 7. A single un-realized through-hole would render a device unusable. The dominant failure mode for un-realized through-holes appeared to be thin PDMS membranes residing over the top surface of upper photoresist features (Fig. 3-8). The hypothesis was that the PDMS was not completely displacing from the top surfaces of the photoresist because the pressure was not high enough during compression. Therefore, a system capable of generating higher pressures was sought,

since manually stacking more steel weights (40 lbs force at that point) would become unwieldy.

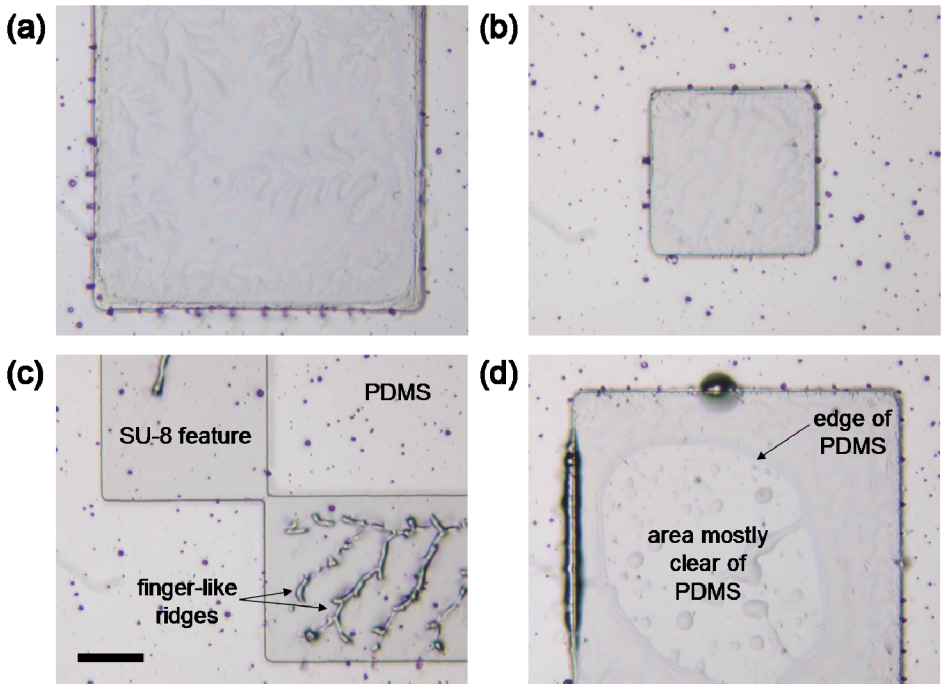

Fig. 3-8 Residual PDMS on the surfaces of SU-8 (photoresist) features after compression-molding. (a)-(b) A thin PDMS membrane on the surfaces of square SU-8 features is visible by its ripples. (c) Finger-like ridges appeared when the PDMS would partially detach off the SU-8 surface when the transparency was being delaminated. (d) PDMS encroaches onto the surface of a square SU-8 feature, leaving only a circular area in the interior clear of PDMS. Residual PDMS was major failure mode while developing the modified compression-molding process, leading to the hypothesis that more pressure was required to clear PDMS off SU-8 surfaces. Scale bar for all subfigures is 200 μm.

Semi-Automated Compression-Molding with NIL: Attempts and Learning

A compression-molding machine, the Nano-Imprint Lithography (NIL) tool (Obducat AB, Malmo, Sweden), was tested as the compression source for device fabrication. The tool is capable of applying pressures up to 80 bar. Also, the tool is capable of applying heat, which would be useful to partially cure PDMS. Both pressure and heating ramps could be programmed, enabling semi-automated operation. PDMS was spin coated onto the wafer to a thickness greater than both photoresist layers (as per other compression-molding trials), and NIL transparencies were laminated to both surfaces of the wafer. The wafer-transparency assembly was loaded into the NIL and pressure-heat sequences were run.

Over several attempts, some minor learning emerged. The NIL was most reliable at maintaining pressures if it was gradually ramped (45 s dwells in 10 bar increments). Faster ramps would cause the pressure to fluctuate and decay to a basal state of 15-20 bar. A pressure of 70 bar was reached on device wafers. Also, partial curing of PDMS was realized using temperature ramps.

The main observation is that the NIL did not successfully make any through-holes. When each wafer was removed, the transparency appeared to conform very precisely to the surface of the photoresist pattern. The NIL is designed to apply very uniform pressure on the stamp and substrate by the use of compressed air as the pressure source. In addition, the two transparencies were sealed together at the edges, preventing PDMS from displacing off the wafer (Fig. 3-9).

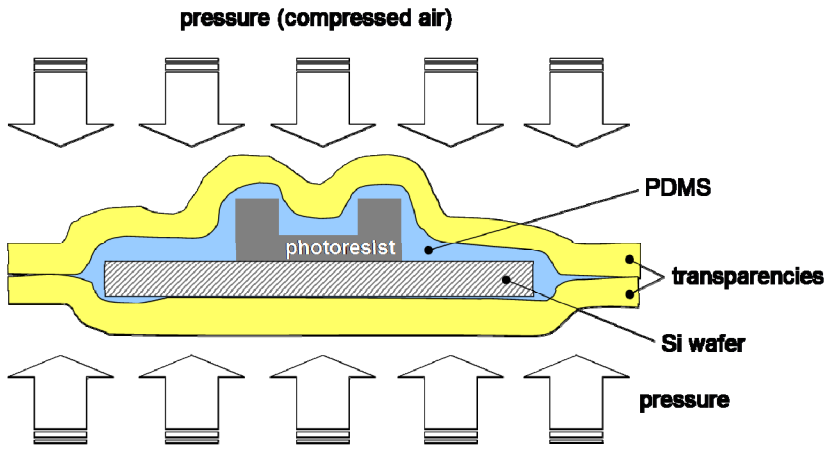

Fig. 3-9 Schematic of highly conformal transparencies after NIL compression. The NIL applies very uniform pressure by way of compressed air. It was speculated that pressure uniformity, as well as the sealing of the transparencies at their edges, could have prevented PDMS from displacing properly from the tops of upper layer photoresist features. This led to a new hypothesis that focusing the pressure over regions with through-holes could completely displace PDMS from the tops of photoresist features.

These observations led to a new hypothesis that the location of pressure, as opposed to pressure in general, could facilitate complete displacement of PDMS from the upper photoresist surfaces. That is, if the pressure was focused over each individual device, rather than over the whole wafer, then it was hypothesized that the PDMS could better displace off the photoresist surfaces because the regions where pressure was not

focused could act as reservoirs where displaced PDMS could collect. To test the hypothesis, small transparency pieces were placed on top of the laminated transparency, directly above each device (Fig. 3-10), thereby focusing the pressure above regions with through-holes. This formed the basis of the final process adopted for this work (modified compression-molding), which is detailed in the following section.

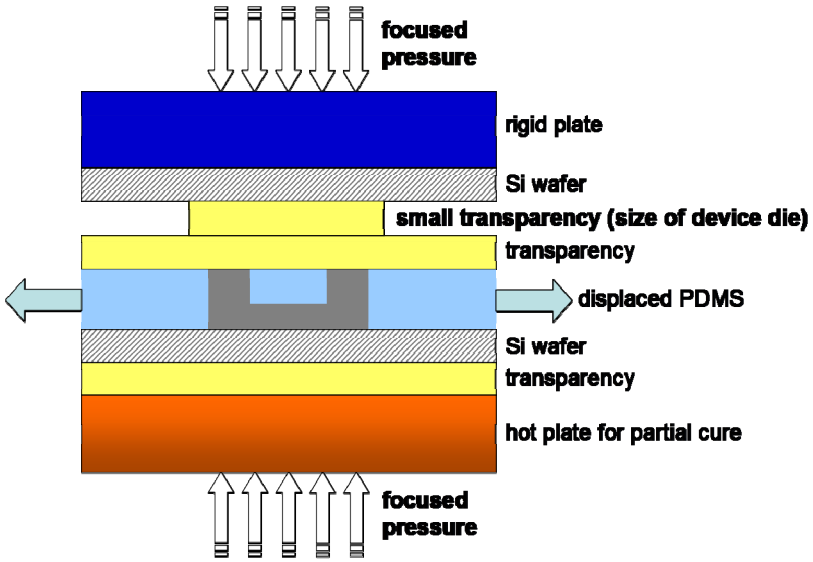

Fig. 3-10 Compression-molding step with pressure localized above device. Pressure is focused only above devices to test the hypothesis that PDMS would better displace off the surface of upper photoresist features because it could collect in areas without focused pressure (reservoirs). Focused pressure formed the basis of the process adopted for all devices fabricated in this work.

Adopted Fabrication Method: Modified Compression-Molding

In this work, 3-D flow networks are realized using a compression-molding process that is a modification of compression-molding techniques described by Folch *et al.*[88] and Kim *et al.*[87] The process developed herein differs in two ways. First, during the compression step, pressure is focused over each device die by the use of small transparency sheets. Focusing the pressure increases yield of through-holes. Second, the alignment step takes place while the two PDMS layers are only partially cured. This allows more time to perform alignments, and it enables reworks if the alignment of bonded layers is out of tolerance.

In general, each device in this work is fabricated using a combination of techniques, including soft lithography,[89] multi-layer PDMS thermal bonding,[83] and through-hole processing.

Fabrication requires two master molds (masters A and B). Each master is a silicon wafer (100 mm diameter) with a photoresist pattern forming device features in positive relief. Photoresist patterns are realized using standard photolithographic methods.[90] Since the master molds are unique to each of the two types of devices developed in this work, details of their fabrication are located in the Methods section of Chapters 4 and 5. For reference, layouts of each type of device are found in Appendix A. In general, for both devices, master A contains a two-layer pattern of SU-8 (MicroChem Corp., Newton, MA, USA) photoresist. The first (lower) layer is 50 μm tall, and its features define the cell chambers, fluid flow channels, and valve control channels (channels that pressurize to close integrated valves; see Appendix C). The second (middle) layer is 30 μm tall and its features define through-holes; it is stacked on top of the lower layer, making the combined height of both layers 80 μm. During the compression step, PDMS is displaced from the surfaces at the 80 μm height.

For both devices, master B contains patterns made of AZ P4620 (AZ Electronic Materials Corp., Branchburg, NJ, USA), a positive-type photoresist. The AZ features are 35 or 25 μm tall (for soluble-matrix array in Chapt. 4 or gradient array in Chapt. 5, respectively) and predominantly define fluid flow channels. AZ features have a semi-circular cross-section, allowing them to be fully closed by integrated valves located throughout the device (see Appendix C for valve actuation description). For the soluble-matrix array, master B also contains SU-8 features 7 μm tall that define perfusion conduits (see Methods in Chapter 4).

PDMS devices (with through-holes) are realized via the following process flow, which is diagrammed in Fig. 3-11 (a wafer-level view of the compression stack is found

in Appendix D and further details are found in Appendix E). Briefly, PDMS (Sylgard 184, Dow Corning Corp., Midland, MI, USA) with a base-to-curing agent ratio of 20:1 is mixed and degassed under vacuum in a desiccator for 2 hours. The PDMS is then spin coated onto master A to a thickness of 200 μm. A mylar transparency is laminated on top of the PDMS; care is taken not to introduce bubbles between the transparency and PDMS. More transparencies are added, including small device-sized transparencies located above device positions. Additionally, a blank silicon wafer, cloth sheets (TechniCloth II, ITW Texwipe, Mahwah, NJ, USA), and steel blocks (total weight ~40 lbs) are placed on the stack to displace PDMS from the top of the tallest SU-8 features. The entire stacked assembly is placed on a flat bake plate (CEE 100CB plate, Brewer Science Inc., Rolla, MO, USA) at 80 °C for 10.5 min. After cooling, the stack is disassembled, and the transparency is peeled off the PDMS surface. Hence, master A is left with a layer of partially cured PDMS that is the same height as the tallest SU-8 features (~80 μm); the tops of such features are devoid of residual PDMS, resulting in well-defined through-holes.

The PDMS on master A is aligned and bonded to a subsequent PDMS layer, which is derived from master B as follows. PDMS with a base-to-curing agent ratio of 5:1 is mixed, degassed (2 hours), and poured onto master B to a thickness of 4 mm. The PDMS is cured at 70 °C in a convection oven for 20 minutes. After cooling, the PDMS is peeled off the master and cut into individual device slabs. Inlet and outlet ports are cored through the slabs using 20G luer stubs.

Each slab is aligned and attached to corresponding locations on the PDMS layer of master A. The two layers are then cured at 70 °C for at least 4 hours (usually 12+ hr) to fully bond into a monolithic device. After cooling, the devices are peeled off the master, and valve control ports are cored through the devices using 21G luer stubs. Finally, each device, along with a glass slide, is exposed to air plasma for 30 sec at 18 W power (Plasma Cleaner PDC-32G, Harrick Plasma, Ithaca, NY, USA), and the two are

brought into contact and irreversibly bonded. Thus, each microfluidic "chip" is comprised of a PDMS device containing all the topographical features (channels, chambers, through-holes, etc.) bonded to a glass substrate. Each device footprint is 24 × 24 mm (for both types of devices). Further processing details are found in Appendix E.

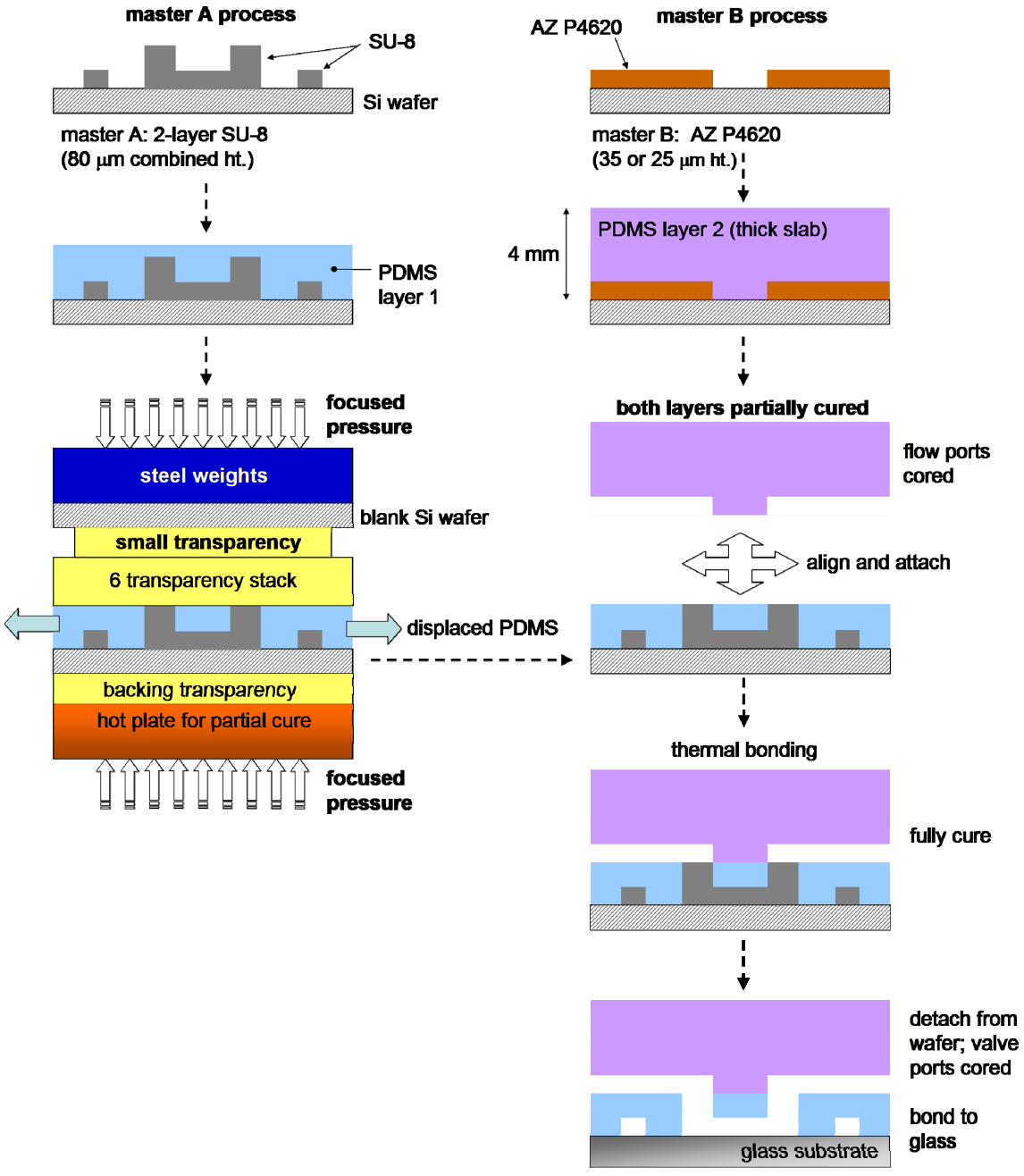

Fig. 3-11 PDMS device fabrication process. Based on modified compression-molding process, including focused pressure compression and partial curing of PDMS layers. All devices in this work are fabricated with the above process.

Discussion

Estimated Yields and Observed Failure Modes

Fabrication can be divided into "front-end" and "back-end" processing. Front-end processing involves all processing steps performed in the cleanroom (up to and including the modified compression-molding process described above), while devices are in batches of 7 carried on a single wafer/master. Back-end processing takes place in a non-cleanroom laboratory, and it involves detaching each device from the wafer, coring valve control ports, and bonding to a glass substrate. More detail on these processes is found in Appendix E.

Table 3-1 Estimated yields in fabrication of chamber array devices.

device design	devices attempted	front-end yield (est.)	final yield (est.)	front-end yield (%) (est.)	back-end yield (%) (est.)	total yield (%) (est.)
soluble-matrix (Ch. 4)	70	35	32	50%	91%	46%
gradient (Ch. 5)	105	67	54	64%	81%	51%
COMBINED	175	102	86	58%	84%	49%

For the two types of devices detailed in this work, 175 were attempted. Front-end yields are obtained from yields reported in laboratory notebooks. Yields for some batches were not reported; hence, front-end yields are considered estimates (not actuals). As a check of the front-end yields, all reported yields for batches of earlier generations of gradient devices were counted, giving a front-end yield of 66%, which is similar to the 64% estimated for the final generation device. Back-end yields were calculated by

counting the number of experiments attempted, assuming that if an experiment is attempted, the device was fabricated successfully. However, some successfully fabricated devices were never used (and therefore never counted), and so the back-end yields are estimates as well.

The estimated front-end yield for the soluble-matrix (Chapter 4) device is lower than that of the gradient (Chapter 5) device. One possible reason is that there are more through-holes in the soluble-matrix array than in the gradient array. Unrealized through-holes were a significant failure mode in front-end processing; if there are more holes in the array, then there is a greater likelihood of a failed (unrealized) hole somewhere within it, stochastically speaking. An alternative reason for the discrepancy in front-end yields is experience. The soluble-matrix devices were fabricated before the gradient ones were; therefore, gradient device fabrication may have benefited from underappreciated (and intangible) gains in skill, which would increase its yield. In addition to front-end yields, there is also a discrepancy in back-end yields. The back-end yield of the gradient device is lower than that of the soluble-matrix one. This could be attributed to a brief period when PDMS-to-glass bonding failed for several gradient devices, which dropped the final yield count.

Failure modes attributed to fabrication are listed in Table 3-2. Frequencies of such failures were not recorded; although, it is recalled that unrealized through-holes were by far the most common failure, despite the use of the modified compression-molding process. One should note that a single unrealized through-hole in a device would render the device unusable (and therefore a failure), and the vast majority of device failures were indeed caused by only one or two unrealized through-holes. The soluble-matrix and gradient devices contain 88 and 54 through-holes, respectively. Thus, as the arrays are scaled, more work is required to improve the compression-molding process (through-hole to through-hole yield) to prevent the device yields from dropping. Further fabrication improvements were not pursued, since the yields were considered

tolerable (for purposes of this work) and it was decided to shift the focus of the work to characterizing and testing the devices with living cells.

Table 3-2 Failure modes observed while fabricating soluble-matrix and gradient devices.

failure mode	fabrication stage	notes
unrealized through-holes	front-end	most common failure mode; detected by observing ripples on top surfaces of photoresist (thin PDMS membrane blocking through-holes) (see Fig. 3-8 for representative images)
gas bubbles on/near critical device features	front-end	occasionally occurred, despite extended degassing (2 hr) of PDMS prior to fabrication (see Fig. 3-6 for representative images)
PDMS peeling off the wafer during transparency delamination	front-end	occasionally the PDMS would adhere more strongly to the transparency than it did to the wafer after partial cure; this was corrected by coating the transparency in silane, while reducing the extent of silanization of the wafer (see Appendix E for details of silanization process)
weak PDMS-to-glass bond (gradient devices)	back-end	weak bonds could not hold 30 psig pressure of valve control channels; changing from glass slides (soda lime glass) to glass cover slips (zinc titania glass) restored adequate bond strength (note: all migration assays were performed with devices bonded to cover glass; thus, glass type is not a confounding factor in analysis)
leaking inlet/outlet port	back-end	occasionally occurred, due to cracks formed in PDMS during port punching process

There is another failure mode to note, although it is associated with design rather than fabrication: successful realization of through-holes is dependent upon the spacing between through-holes. If two through-holes are less than 200 μm from each other (center-to-center), they typically do not form completely. This could be due to slight height differences between the upper photoresist features of each through-hole. If one is taller than the other, it prevents the transparency from laying flat on the shorter one. Thus, the PDMS is not fully displaced. In addition, through-holes in devices in the center of the wafer almost always do not form. This could be caused by not having a fully uniform pressure distribution (among the focused regions) or by slight photoresist height differences from the center to the edge of the master wafer.

Scaling Efficiency and Scaling Rules

Over the past decade, PDMS microfluidic systems have made dramatic progress in their features and functionality. Many systems now incorporate integrated (on-chip) pumps and valves that assist in fluid handling through flow channel/chamber networks. Despite such progress, challenges still remain, particularly in the area of chamber array scalability. One should note, the term "scaling" in this context does not have the same meaning as traditionally interpreted in chemical engineering, where "scaling" typically refers to the pursuit of increasing production by scaling "up" the size/volume of reactor and processing vessels. Instead, scaling in this context is the pursuit of scaling "out" to larger numbers of chambers.

A predominant tenet in microfluidic device design is that flow paths must navigate 2-dimensionally, i.e. the flow paths are restricted to the layer they are in. Scaling to larger numbers of chambers in an array requires proportionate amounts of input/output ports, as well as greater allocations of device real-estate for fluid bussing channels to support the chambers. If flows could navigate vertically (by through-holes) between layers, then scaling efficiency could be increased. An example of this is illustrated in Fig. 3-12. Vertical connectivity between layers enables the creation of overpasses and underpasses so that separate channels can cross without mixing; therefore, efficiencies are gained by a reduction of (i) input/output ports and (ii) real-estate allocation for the same number of chambers.

The scaling rule for number of input/output ports for the architecture in Fig. 3-12(a) would be:

$$N_{ports} = N_{ch} + N_{row},$$

where N_{ports} is the number of input/output ports, $N_{chamber}$ is the number of chambers, and N_{row} is the number of rows in the array. The efficiency of output ports could be improved by merging ports for conditions A, B, and C into a single port. However, this would

come with a cost in fluid handling maneuvers; instead of priming each row through a single port, the inlet ports would need to be used to load conditions A, B, and C, as well as conditions 1-5. For each outlet port merged (removed), four new attachments (and detachments) to fluid sources would need to be executed.

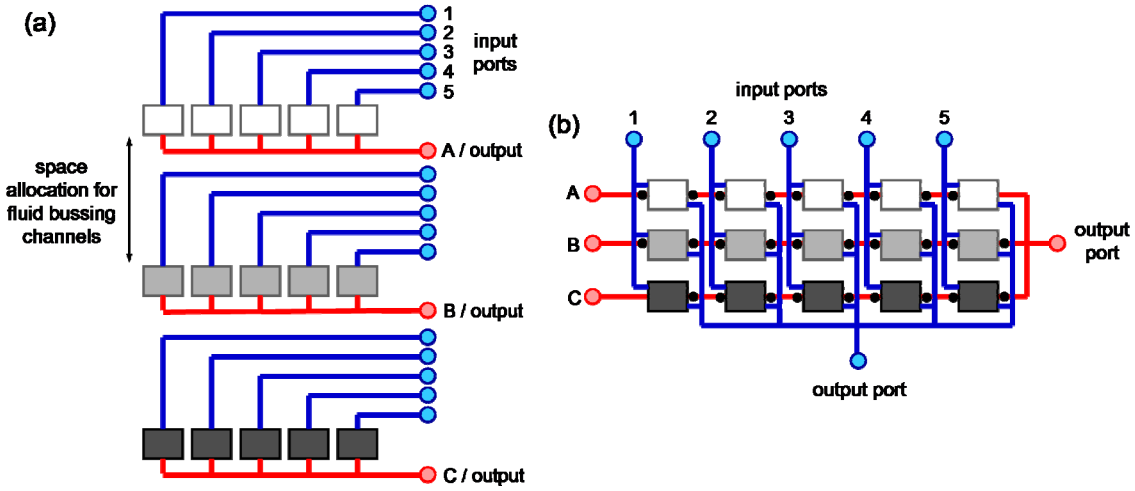

Fig. 3-12 Example of a gain in scaling efficiency using 3-D flows. (a) and (b) illustrate an array of chambers individually addressed with combinatorial conditions. Conditions A-C are primed by rows; then conditions 1-5 are dosed by columns. (a) For a standard 2-D flow network, each chamber requires an input port, as well as more space for bussing channels. (b) Flow layers with vertical connectivity create 3-D flows, reducing input/output ports and space allocations for the same number of chambers and conditions. Small black dots denote locations of vertical interconnect (through-holes). The array detailed in Chapter 4 addresses a similar problem. Macro-to-micro ("world-to-chip") interconnect takes place at input and output ports; hence, the larger circular footprints.

The corresponding scaling rule for the architecture in Fig. 3-12(b), which makes use of 3-D flows, is:

$$N_{ports} = N_{rows} + N_{columns} + 2,$$

where $N_{columns}$ is the number of columns and the quantity 2 arises from the two output ports. If arrays were created based on the row-to-column ratios of standard well plate formats, the scaling rules would result in the plots in Fig. 3-13.

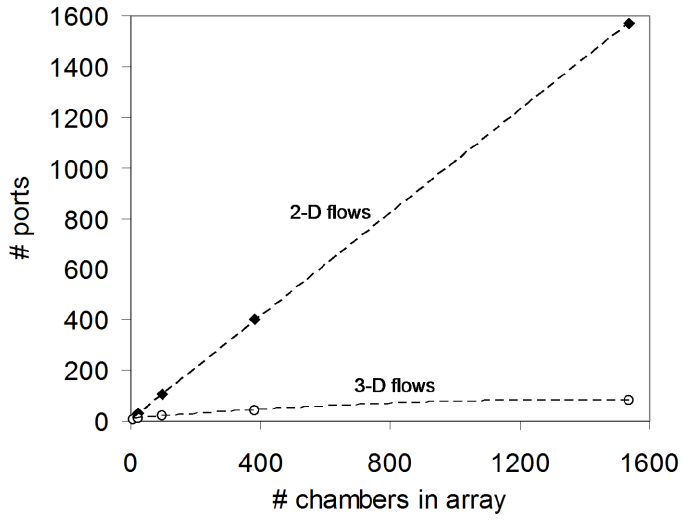

Fig. 3-13 Scaling of inlet/outlet ports for the problem in Fig. 3-12 (combinatorial conditions by rows and columns). For a 2-D flow architecture, the number of ports scales linearly with the number of chambers. A 3-D flow architecture results in the number of ports scaling roughly in the square root of chambers. Numbers of rows and columns for each calculation point based upon standard 6 (2×3), 24 (4×6), 96 (8×12), 384 (16×24), and 1536 (32×48) well plate formats.

The scaling of input/output ports is important in two respects. First, because ports are the "world-to-chip" (macro-to-micro) interconnect points, each port requires a substantial amount of space (footprint) relative to other device features in order to fit the tubes or needles for fluid introduction. For instance, microfluidic systems in this laboratory are designed so that center-to-center spacing between ports is at least 1.5 mm, as opposed to typical channels in the device that could be 50 to 100 μm wide (and spaced at similar distances). As the array scales to more chambers, a 2-D flow architecture would result in an explosion in footprint required for the growth in ports. Secondly, the likelihood of device failure increases with ports. For PDMS microfluidic devices, each port is punched or molded (manually or in a semi-automated way), and plastic tubing or metal needles (luer stubs) of a larger gauge are press-fitted into the hole, forming a tight seal. For this work, a port defect could be a punch that misses its target or a crack propagating radially from the hole that causes a leaky interconnect (see previous section on Yield). For example, one defective port out of every 100 may result in an acceptable yield for small

arrays, but such a rate would drastically decrease yield for arrays approaching 100 chambers, depending on the defect frequency distribution. Therefore, minimizing the number of ports is important for maintaining device yield.

Scaling rules for the additional footprint that must be allocated for fluid bussing channels (denoted in Fig. 3-12(a)) (both in length and quantity) could also be derived, based on design rules for channel widths and spacings (different for each lab and application). Similar to ports, a 3-D flow architecture would result in greater footprint efficiency compared to a 2-D one.

Microfluidic Arrays and Well Plates

The device described in Chapter 4 contends with a variation of the same problem in Fig. 3-12, where different matrix signals are coated by rows and media with different soluble signals are perfused by columns. For microfluidic designers, the motivation to address individual chambers with different combinations stems from the desire to achieve the same level of versatility as conventional well plates. Well plates are extremely versatile, where any combination of conditions can be pipetted into any well. To reduce sample usage and increase throughput, well plates with smaller wells and higher density (up to 1536+ wells per plate) are now offered. Such advances have created challenges, such as the growing effect of evaporation and escalating numbers of fluid handling maneuvers (pipetting, either manual or robotic).[91] Microfluidic systems are well-suited to prevent evaporation, since they are closed systems. In addition, microfluidic systems could redefine the notion of fluid handling; instead of robotic (or human) arms maneuvering pipettes between wells and reloading/cleaning stations, fluid handling could be executed in a microfluidic network by drawing and delivering fluids from desired input ports using on-chip valves (and/or pumps). Automated control of such operations could prove to be more rapid and reliable than current handling methods.

However, the abovementioned benefits of microfluidic systems are severely negated without 3-D flow networks to facilitate individual addressing of chambers. In addition, integrating an on-chip valve network that isolates chambers from each other is critical. It is inconceivable for an experimentalist to tolerate using a well plate with wells that leak among each other (unless such leakage was a deliberately designed as an experimental condition). By the same logic, microfluidic chamber arrays that claim to offer similar versatility (individual addressing) as well plates must demonstrate chamber isolation. The use of on-chip valve networks further amplifies the need for 3-D flows, since flow channels would also have to navigate over (or under) valve control channels.

The pursuit of fabricating 3-D flow networks is not new. Several groups have developed methods to fabricate through-holes and 3-D networks (see beginning of chapter, 3-Dimensional Flow Networks); however, such works have only been for demonstration, and attempts to implement such architectures for specific applications, particularly for cell-based assays, are absent. It is speculated that attempts at specific applications are absent because the creation of 3-D flow networks is challenging even for research groups dedicated to microfluidics; instead, groups may judiciously choose to pursue applications that can be accomplished with 2-D flows. Based on the extent of process debugging in this work, groups could be deterred from pursuing 3-D flow network applications because many "tricks" (the art) of 3-D network fabrication are unreported or under-explored. Moreover, without yield information (actual or estimated), researchers have no basis upon which to judge the amount of work required if they pursue such applications.

This work intends to move microfluidic chamber arrays closer to the goal of one day being as well-accepted as well plates to perform cell-based screens. However, regular use of microfluidic chamber arrays in academic and industrial labs is many years away for a number of reasons. First, there is not yet enough scale in microfluidic arrays. The arrays constructed in this work (8 and 6 chambers in Chapters 4 and 5, respectively)

are small compared to well plates with hundreds or thousands of wells. The largest independently-addressed microfluidic chamber array for cell-based assays contains 96 chambers, but it could only scale in one dimension, cannot continuously perfuse medium to each chamber, and could expose cells to pulses of high shear due to the manner in which it performs medium changes.[92] The work in Chapter 4 attempts to address such issues, but new challenges and technical trade-offs may emerge as researchers continue to scale-out microfluidic chamber arrays.

Second, there is a lack of automation and standardization in macro-to-micro interconnects; fluid sources are connected to ports manually in most settings, and although there are some commercially available microfluidic arrays,[93] the macro-to-micro interconnections for them are proprietary. Without automation and standardization, macro-to-micro interconnections will become a major bottleneck in the usage and dissemination of microfluidic chamber array technology.

Third, microfluidic devices of the complexity in this work are still too difficult for most lay technicians and graduate students to operate. Procedures like device priming and cell loading are labor-intensive and require finesse gained from experience. Once again, lack of technology and standardization in such protocols is a key bottleneck. Another difficulty is in controlling microfludic systems; to perform the assays in this work, a many instruments need to work in coordination. Without a "black box" hardware and software setup, writing custom-software to coordinate syringe pumps, microscopes, x-y stages, on-chip valves, and imaging equipment may prove too difficult for most workers.

Fourth, microfluidic chamber arrays are still not as generalized and versatile as well plates. For example, any well plate can accept either pure liquids or gels, while most microfluidic arrays (including the ones in this work) would require a redesign to specifically accommodate different phases. The concept of generalization, where the same device can be used in different ways, is a key concept for large scale

commercialization. If the same device could perform more and different tasks, the result would be higher manufacturing volumes and lower costs per unit. Ultimately, the goal of microfluidic chamber arrays should not be to replace well plates, but instead to provide an effective alternative, particularly to prevent evaporation, perform complex fluid handling, and reduce sample usage.

General Discussion

As previously mentioned, the modified compression-molding technique detailed in this chapter differs from other techniques in that it focuses pressure in specific areas (device locations) and aligns using partially cured PDMS.

Focused pressure results in all through-holes being successfully realized in roughly 60% of devices fabricated (front-end yield). This is an improvement over attempts without such modifications (yielding less than 15% of devices), presumably because it assists in displacing PDMS from the tops of SU-8 features by providing a nearby reservoir between devices into which PDMS can collect. We also use soft cloths (Texwipes) in the stack, further improving the through-hole yield by providing a more uniform distribution of pressure across the master and over each device.

In addition, the PDMS is partially cured (in lieu of fully cured) so it can be thermally bonded to a subsequent PDMS layer (from master B). The thermal bonding technique provides ample time (up to 3 hrs, since PDMS cures slowly at room temperature) to properly align the two PDMS layers. This differs with air plasma bonding, which affords far less time (<1 min. after plasma surface activation). Extra time is beneficial, particularly for manual alignments, or for aligning multiple devices on a single master, which could take more than a minute to complete (whether manual or automated). Another difference is that plasma bonding is a “one-shot” event. If the layers are aligned outside of tolerance, there is no way to rework. On the other hand, partially cured PDMS layers permit reworking.

An added feature made possible by the 3-D flow network is the seeding and attachment of cells onto the surface of the underlying (supporting) substrate of the device (in this case, glass). To elaborate, one consequence of the on-chip push-up valves is that cells approach each chamber from the top flow layer. For cells to make contact with glass in the chamber, they must travel by way of through-holes from the top layer (with the PDMS surface) to the bottom layer (with the glass surface). Otherwise, cells would seed in the top layer on a surface made of the bulk material of the device (PDMS), as is the case for other microfluidic cell culture arrays.[92,94]

The devices in this work are designed with the default option to seed cells on glass or other rigid substrate. This is necessary if high-magnification microscope objectives with small working distances are utilized (requiring substrate thicknesses comparable to cover slips). Nevertheless, if one desires for cells to grow on PDMS or another soft material, it can be coated to the appropriate thickness on the substrate prior to attaching the device.

A limitation of the modified compression-molding technique is that it is a batch process that currently requires manual alignments. This problem affects all 3-D flow network fabrication processes. In this case, manual alignment of each device (being 24×24 mm) requires roughly 5-10 min. However, it is reasonable to assume that the devices could be manufactured in larger volumes in a more automated fashion, given that multilayer PDMS devices (also requiring alignments) are commercially available.[93]

Images of fully-fabricated devices showing through-holes are found in Figs. 4-3 and 5-2. Close-up views of through-holes are shown below in Fig. 3-14.

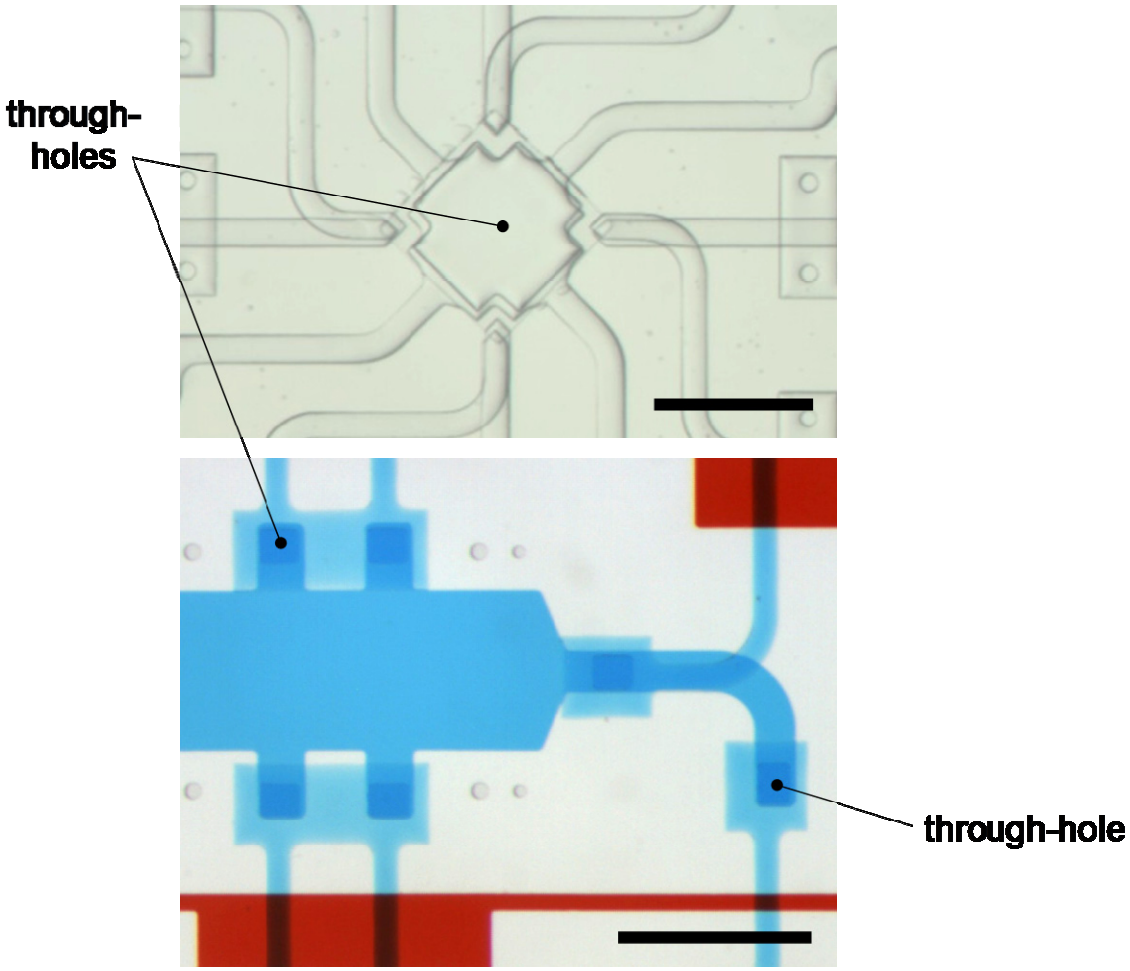

Fig. 3-14 Through-holes in finished devices. Top subfigure shows an earlier generation device with a 500 × 500 μm square through-hole. Lower subfigure shows through-holes (100 × 80 μm) in soluble gradient device (Chapt. 5). The two types of microfluidic chamber arrays based upon the modified compression-molding process contain 88 and 54 through-holes each (for the soluble-matrix and gradient designs, respectively). Both scale bars are 500 μm.

Chapter Summary

This chapter reviews the development of a process to produce through-holes for vertical connectivity between flow layers (3-D flows) in microfluidic chamber arrays. Specifically, this work explores two previously reported fabrication methods (protrusion and compression-molding), develops yield-enhancing modifications (for compression-molding), and estimates the resulting device yields. Efficiencies provided by 3-D flows for array scaling (and associated scaling rules) are discussed. In addition, ongoing challenges that hinder widespread use of microfluidic chamber arrays in academic and

industrial laboratories are discussed. The following chapters (4 and 5) describe attempts to apply microfluidic chamber arrays with 3-D flow architectures as actual cell-based assays.

Table 3-3 Chapter 3 summary.

advances / contributions
1. a modified compression-molding process for production of through-holes in PDMS microfluidic chamber arrays based on two yield-improving features * (a) focused pressure over devices (realizing through-holes, up to 88 in an array) (b) alignment using partially-cured PDMS layers (enabling reworks)
2. first microfluidic chamber arrays utilizing 3-D flows that are designed and tested for *specific* applications (cell-based assays described in chapters 4 and 5), rather than simple flow network demonstrations
main learning
1. for the protrusion through-hole method, curvature (wetting) of PDMS near photoresist posts could complicate fabrication (especially for upper layers with low channel height)
2. photoresist support posts are critical to maintaining planarity and preventing unintentional interconnect between channels at underpass/overpass points (for compression-molding methods)
3. gas bubble nucleation during compression can be minimized by extending the time of degassing PDMS in vacuum
4. very uniform pressure, such as that provided by compressed air (NIL), could hinder through-hole formation (leading to the focused pressure hypothesis)
challenges / limitations
1. current arrays are small; greater scale is required to prove viability as industrial screening platforms, and new technical challenges may emerge as scaling is attempted
2. lack of automation and standardization in macro-to-micro interconnect hinders large scale adoption of microfluidic technology
3. arrays are too complex to be operated by lay technicians; a "black box" approach is necessary
4. arrays are still not as generalized and versatile as well plates
5. fabrication method is a batch process requiring a manual alignment; it must be automated (at least semi-automated) for commercial production

* Note: fabrication process and resulting 3-D flows are featured (and process detailed) in published work.[95]

CHAPTER 4

A MICROFLUIDIC CHAMBER ARRAY FOR STUDYING CELLULAR RESPONSE TO COMBINATIONS OF MATRIX AND SOLUBLE SIGNALS

This chapter describes the development of a microfluidic cell culture array with unique versatility and parallelization for trials requiring perfusion cultures. A rectangular chamber array in a PDMS device is realized with three attributes: (i) continuous perfusion; (ii) independently-addressable chambers and subarrays; and (iii) flow paths that forbid cross-chamber contamination. These attributes are made possible by the 3-D flow architecture described in Chapter 3. Versatility is achieved via subarray, row, column, or single chamber addressing for the following: incubation with adsorbed molecules; perfusion of different media; seeding or extraction of cells; and assay staining. Moreover, culture surfaces are shielded from direct perfusion to minimize shear-induced cell changes. Device operation is demonstrated by culturing alveolar epithelial type II (ATII) cells in different combinations of matrix and soluble signals within the 2×4 chamber array. After culture, staining is performed to ascertain responses to each signal combination. By loading and culturing cells to different conditions, in addition to performing post-culture assays, it is shown that this prototype array and its 3-D flow architecture could facilitate combinatorial screening and form the basis of larger arrays for basic and industrial research.

Specific Motivation and Objectives

Over the past several years, numerous works have demonstrated the utility of microfluidic arrays as screening tools to culture cells in diverse microenvironments.[96-102]

Interest in microfluidic systems arises from the prospect of very low sample usage, highly-parallelized experiments, and well-controlled culture conditions, all of which are facilitated through miniaturization. With respect to microenvironments, the screening of cellular responses to simultaneous stimulation of soluble and extracellular matrix (ECM) cues is a broad line of inquiry that is particularly useful in studying phenotype transitions. One example is epithelial-to-mesenchymal transition (EMT), which is implicated in numerous developmental and pathological processes. Greater understanding of phenotype transitions could lead to new therapeutic approaches, facilitated by microfluidic arrays with new capabilities.

Microfluidic chamber arrays have been developed in many forms, and most can be categorized into one of three generalized architectures. First, there are open array architectures, where all chambers are fluidically linked, allowing flow and diffusional transport among chambers.[103-107] The extent of cross-chamber communication (convective or diffusional) is determined by the flow rate, flow direction, and device geometry. Second, there are architectures isolated by rows/columns, where flow is restricted to individual rows (or columns) by valves or other barriers.[108-112] Therefore, only communication among chambers within rows (or columns) is possible. Signals secreted from cells in upstream chambers may be a concern, the extent of which depends upon the signal and its concentration, which in turn is determined by cell density, secretion rate, and flow velocity. Third, there are architectures where the chambers are completely isolated from each other and individually addressed. This eliminates cross-chamber communication by extensive use of on-chip valves and delivery channels.[92,94]

In addition to the general array architecture, the chamber design is also an important feature, particularly with respect to shear stress.[113] Undesired shear-induced cell behavior can be minimized by the use of flow barriers[104] or by recessing the chamber from the main flow path.[103,110]

In this work, a microfluidic array architecture is introduced that demonstrates a novel combination of attributes: continuous-perfusion through each chamber, no cross-chamber communication (i.e. contamination), and chamber shielding to reduce shear stresses experienced by cells. At the same time, a high degree of versatility is offered, as well as experimental parallelization. We demonstrate the operation of this device by observing the effect of extracellular matrix (ECM) proteins fibronectin (Fn) and laminin (Ln), in conjunction with soluble transforming growth factor- β1 (TGF-β1), on alveolar epithelial cells. This requires a combinatorial experimental setup that takes advantage of the attributes of our device design.

Device Design

The array device is comprised of three layers. The bottom layer contains flow channels, cell chambers, and control channels (for on-chip valve actuation). The middle layer contains through-holes that connect the top and bottom layers. The top layer contains flow channels, as well as conduits that allow flow into the protected areas of chambers (Fig. 4-1).

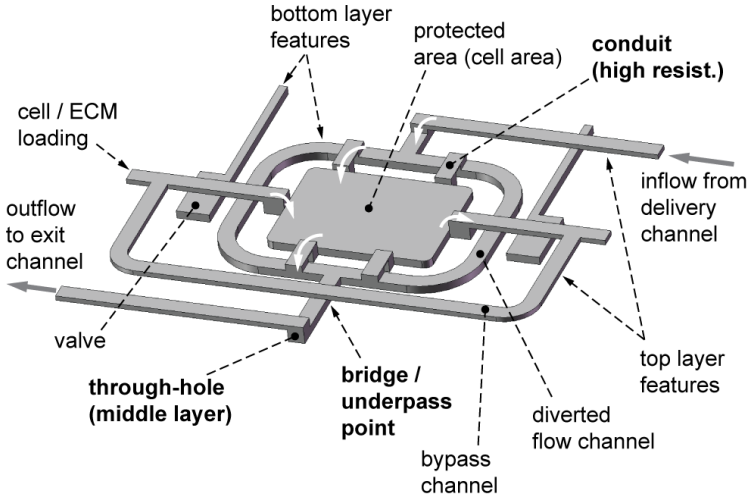

Fig. 4-1 Schematic of device architecture. Three-dimensional flow network requires through-holes (middle layer) that fluidically connect top and bottom layers. White arrows indicate selected locations where flow travels 3-dimensionally. (i) Chamber is continuously-perfused by inflowing medium. (ii) Cross-chamber communication is avoided; fresh medium from a delivery channel (not shown) flows through the chamber and into an exit channel (also not shown). (iii) High-resistance conduits on chamber ceiling shield the protected area from the majority of flow. The chamber, along with supporting channel network, is repeated to realize a 2×4 prototype array device.

Three attributes

The first attribute is continuous perfusion. Continuous perfusion is desirable because it offers greater control of the cellular microenvironment when compared to traditional static culture. The concentration profile of any soluble signal of interest could be spatially and temporally controlled, whether the signal is pre-loaded into the medium or is secreted by cells in the chambers. Such control has proven useful in eliciting more physiological responses from a variety of cells in culture.[114-119]

The second attribute is the implementation of flow paths that forbid cross-chamber contamination. Flow paths are arranged such that once a streamline passes through a chamber, it does not pass through any other chambers before exiting the device. Therefore, there is no cross-talk from chamber to chamber, which eliminates the confounding effects of signals from neighboring chambers. This is especially important when cells are known to be highly-sensitive to signals present in other chambers (i.e. conditions) of the array or when the sensitivity of the cells to such signals is unknown. Additionally, fluid handling systems used with traditional well plate arrays are subjected to thorough cleaning procedures to minimize carryover contamination between wells.[91,120] For microfluidic arrays to yield biologically significant data, they must (among other things) meet or exceed the rigor of traditional systems in avoiding contamination.

The third attribute is a chamber design that reduces the shear stress applied to cells by shielding them from direct flow. One example of a shielded chamber is by Lee *et al.*,[104] where the majority of perfusing medium is diverted around a wall-like barrier, which surrounds a protected area where cells reside. Narrow conduits (gaps or mini-channels) in the barrier allow a small fraction of the overall flow to penetrate through the protected area and transport nutrients to the cells. The fraction of flow is determined by the hydraulic resistance of the conduits, which in turn is determined by their geometry. The chamber designed in this work is conceptually similar to the one just described.

However, there is a notable difference: the chamber is designed so that flow enters and exits the protected area through conduits on the ceiling, a different plane from where the cells are attached. Flow must travel in three dimensions – vertically upward, horizontally across a conduit, then vertically downward. Two conduits serve as inlets at the upstream end of the chamber, and two serve as outlets at the downstream end (Fig. 4-1). The purpose is to avoid cell migration or proliferation into the conduits, which could block the flow path. This is especially likely for cells that require seeding at high densities (i.e. epithelial cells).

Modes of operation

A key philosophy in designing the array is not only to combine the three attributes above, but also to provide considerable versatility to the user. Such versatility is demonstrated through multiple modes of operation and chamber addressing configurations. Figure 4-2 diagrams four basic modes of operation: (i) incubation of chamber surfaces with selected extracellular matrix (ECM) molecules; (ii) loading of cells into chambers; (iii) perfusion of selected growth media; and (iv) assay of cellular response to culture conditions. In addition to the addressing configurations illustrated in Fig. 4-2, other configurations can be implemented in order to generate more combinations of culture conditions or increase replicates. For instance, different cell types could be loaded into separate rows, as opposed to a single cell type.

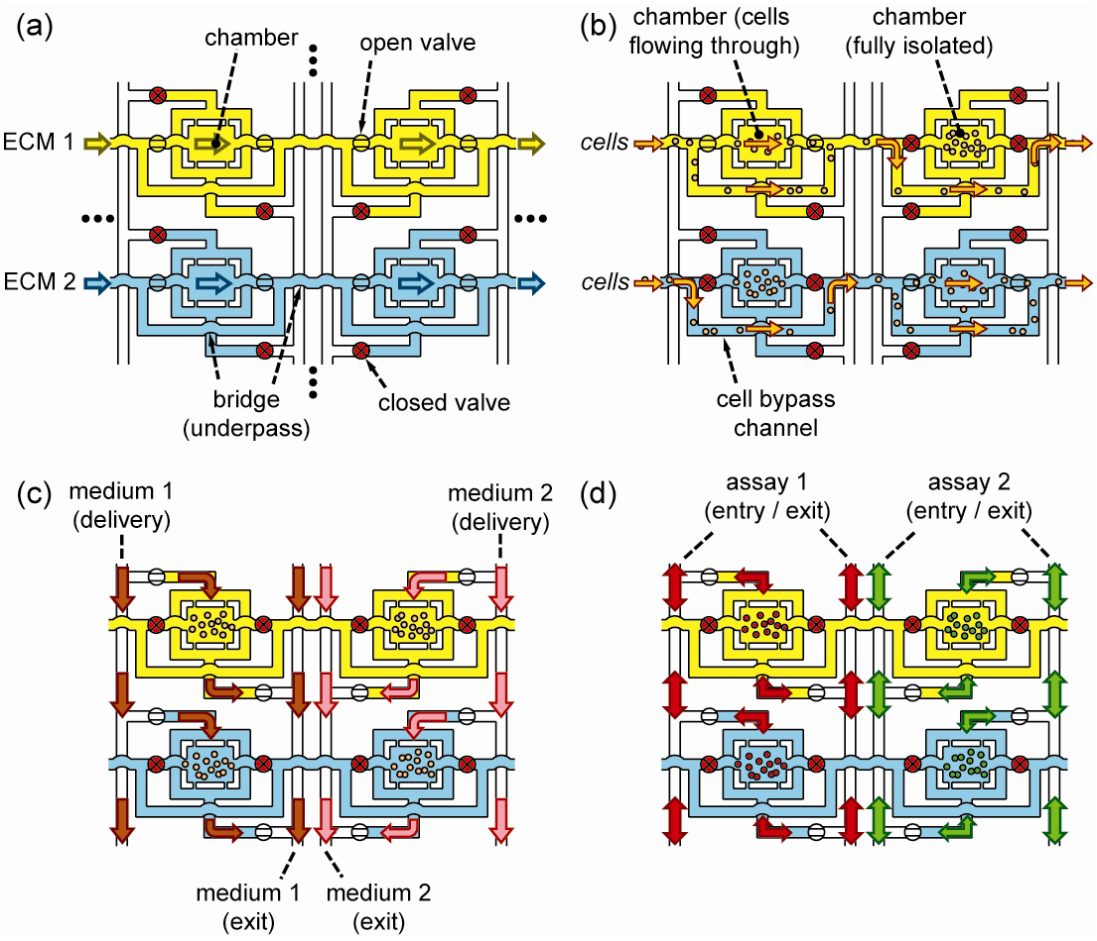

Fig. 4-2 Selected modes of operation shown in a subarray of 4 chambers. (a) ECM incubation: matrix molecules adsorb to chamber surfaces by rows or individual chambers. (b) Cell loading: cell suspension flows into rows, and chambers are isolated (individually or together) to confine cells. Cells attach and spread. (c) Culture: Perfusion of different media by columns. Channel architecture directs flows over/under other flows to avoid cross-chamber communication. (d) Assay: Solutions flow through the entry or exit channels to label cells with desired probes. Illustrations not to scale.

A compelling feature of the array is the ability to address individual chambers. Individual addressing is possible because four on-chip valves regulate flow into each chamber (two for column flow and two for row flow). When all four valves are closed, the chamber is fully isolated from the rest of the array. As a result, the experimentalist is given the opportunity to assign conditions or query a response with a high degree of chamber specificity. If desired, different ECM molecules, cell types or assay reagents could be addressed to each chamber. As shown in Fig. 4-2(b), independent addressing is particularly useful during cell loading. As the cell suspension flows across a row, the cell

density tends to vary spatially, which is troublesome when the objective is to load each chamber with roughly the same number of cells. If the cell density in a chamber is unsuitable, then the valves can be opened momentarily and then closed again to sample a new set of cells. This can be repeated until the appropriate density is achieved. Furthermore, once a chamber is isolated, the flow of cells to other chambers continues uninterrupted, since cells can travel around isolated chambers via bypass channels. It is important to note that the ability to load cells by individual chambers also implies the ability to extract cells from an individual chamber of interest after the culture is completed.

Methods

Fabrication

Fabrication begins with the creation of two master molds on Si wafers. Master A contains a two-layer pattern of SU-8 (MicroChem Corp., Newton, MA, USA), a negative-type photoresist. The first layer is 50 μm tall, and its features define the "bottom" device layer. The second layer, which is patterned on the first layer, is 30 μm tall with features defining the "middle" device layer (i.e. through-holes). Master B contains patterns made of both AZ P4620 (AZ Electronic Materials Corp., Branchburg, NJ, USA), a positive-type photoresist, and SU-8, which define the "top" device layer. CAD layouts of the bottom, middle, and top layers are shown in Fig. A-1 (Appendix A). The AZ P4620 features (35 μm tall) define flow channels. These channels have a curved, almost semi-circular cross-section, allowing them to be fully closed by push-up valves located throughout the device (Appendix C). The SU-8 features on master B (7 μm tall) correspond to conduits (four for each chamber) that allow perfusion through the chamber ceilings (Fig. 4-1). Final devices are made of PDMS using the modified compression-molding process described in Chapter 3 (and in Appendix E).

Simulation of chamber flow field

The chamber is designed to provide continuous perfusion while protecting cells from adverse shear stress. To achieve these effects, a barrier is used to divert the majority of flow around a protected area where cells grow. Conduits (with high hydraulic resistance) on the ceiling of the chamber are intended to allow adequate mass transport through the protected area to nourish cells without undesired shear. To validate this rationale, a 3-dimensional finite element model of the chamber is constructed using the COMSOL software package (Multiphysics 3.3, COMSOL AB, Stockholm, Sweden).

The geometry of the model represents a half chamber, which exploits the two-fold symmetry of the design. All boundary conditions are no-slip, except for the inlet, outlet, and symmetry boundaries. Flow is driven by imposing a pressure drop between the inlet and outlet (positive pressure at inlet boundary and zero pressure at outlet boundary). The Navier-Stokes equations are solved at a variety of flow rates, using water as the medium. The resulting flow fields are used to generate flow velocity profiles and compare residence times through the diverted and protected areas of the chamber (Fig. 4-4 later).

Cell culture off-device

RLE-6TN cells (ATCC, Manassas, VA, USA), a rat-derived ATII cell line, are maintained in D-MEM/F-12 medium (Gibco 10565, Invitrogen, Carlsbad, CA, USA) with 10% fetal bovine serum and 1% penicillin/streptomyocin. Cells are incubated at 37°C and 5% CO_2, and medium is changed every 48-72 hours.

Prior to each trial, cells are detached from their culture flask using trypsin-EDTA solution (0.25% w/v trypsin and 0.53 mM EDTA, Gibco 25200, Invitrogen, Carlsbad, CA, USA). Once the cells are detached, excess medium is added, and the suspension is centrifuged. The supernatant is aspirated, and the cells are resuspended in medium to a density of $\sim 3 \times 10^6$ cells/mL and loaded into the device.

Microscope setup and supporting apparatus

Device preparation, cell loading, and assays are performed on a DM IRB/E inverted microscope (Leica Microsystems GmbH, Wetzlar, Germany) at 10X or 20X magnification in phase contrast mode or fluorescence mode. Hollow stainless steel pins (L-shaped, 21G) are press-fitted into device ports and are connected to flexible plastic tubing (PE-60) for fluid and pressure delivery. Perfusion is driven by syringe pump (PHD 2000, Harvard Apparatus, Holliston, MA, USA). Pressurization of on-chip valves is regulated by off-chip miniature solenoid valves (Hargraves Technology Corp., Mooresville, NC, USA) attached to a pressure source at 30 psig. Images are captured using a digital CCD camera (ORCA C4742-95-12, Hamamatsu Photonics K.K., Hamamatsu City, Japan). Valve actuation and image capture are computer-controlled using a custom-designed interface written in the LabVIEW programming environment (National Instruments Corp., Austin, TX, USA).

Device preparation and cell culture in-device

Devices are prepared to culture cells under four different signal combinations: Fn only, Ln only, Fn with TGF-β1, and Ln with TGF-β1. Fn and Ln (33016 and 23017, respectively, Invitrogen, Carlsbad, CA, USA) solutions used for incubation are both 50 nM concentration in phosphate buffered saline (PBS). When present, TGF-β1 (R&D Systems, Minneapolis, MN, USA) concentration is 5 ng/mL.

Each device is pre-filled with PBS. To prevent on-chip valves from introducing gas bubbles into the device during experiments, each valve is filled with water. Solutions of ECM protein are introduced through row inlet ports, and each solution is addressed to selected chambers by opening the appropriate on-chip valves. The ECM is incubated at 37 °C for 1 hr to allow matrix molecules to adsorb to chamber surfaces. Following ECM adsorption, the device is filled with heat-denatured BSA solution (1% w/v in PBS) and incubated at room temperature for 30 min to block surfaces from non-specific binding.

The device is then flushed with additional PBS, and rows are isolated from each other with on-chip valves.

Cell suspension is then introduced into the inlet of each row and flows through all chambers in the row. Cells are confined to a chamber by closing its chamber isolation valves. Bypass channels allow cells to travel around closed chambers to other chambers. If the density or distribution of cells in a chamber is unsatisfactory, the isolation valves can be momentarily re-opened and closed to sample another set of cells.

The device is transferred from the microscope to an incubator at 37 °C and 5% CO_2. Medium is introduced into medium inlet ports and perfuses through each column at 0.3 μL/min.

Cell Assays

All assays are performed after 48 hrs in culture in device. Cell viability is determined by staining with two-probe LIVE/DEAD® solution (L-3224, Invitrogen, Carlsbad, CA, USA) prepared to manufacturer's specifications (2 μM calcein AM and 4 μM ethidium homodimer-1 in PBS). LIVE/DEAD solution is introduced to the device through an assay port (denoted in Fig. A-1), flow is stopped, and the stain is incubated for 30 min before imaging.

To characterize differences in spreading and cell shape in response to culture conditions, actin cytoskeletons are labeled with Texas Red®-X phalloidin (T7471, Invitrogen, Carlsbad, CA, USA) and imaged. The following washes are flowed through the array: (i) fix with 4% v/v paraformaldehyde in D-MEM/F-12 medium for 15 min; (ii) PBS rinse; (iii) acetone permeabilization for 10 min; (iv) PBS rinse; and (v) phalloidin in PBS (160 nM, prepared by manufacturer's protocol) for 20 min. Flows are ~1 μL/min. Washes are performed by alternating the introduction of the different solutions through the assay/exit ports.

To characterize differences in the extent of epithelial junction formation, immunofluorescent staining for E-cadherin is performed. The following washes are flowed through the array: (i) fix with 4% v/v paraformaldehyde in D-MEM/F-12 medium for 10 min; (ii) PBS rinse; (iii) Triton X-100 (0.5% w/v in PBS) permeabilization for 10 min; (iv) PBS rinse; (v) goat serum (10% v/v in PBS) blocking for 15 min; (vi) primary antibody (36/E-Cadherin, BD Transduction Laboratories, San Jose, CA, USA) in PBS+0.2% w/v Tween (PBST) static incubation for 12 hours overnight; (vii) PBST rinse; (viii) secondary antibody in PBST (Alexa Fluor® 488-conjugated goat-anti-mouse, Santa Cruz Biotech Inc., Santa Cruz, CA, USA) static incubation for 1 hr; and (ix) PBST rinse. Optimization of the protocol showed that Triton X-100 permeabilization produces higher-quality fluorescent images (more visible staining) compared to acetone permeabilization. All flows are ~1 μL/min, and the introduction of different solutions is alternated between assay/exit ports.

Data analysis

To quantify morphological differences, cells are traced by polylines using image processing software (Image-Pro 6.1, Media Cybernetics Inc., Bethesda, MD, USA). Circularity and area of cells is calculated for each culture condition (30 randomly selected cells per condition, 10 from each of 3 trials). Circularity, C, is defined as $C = 4\pi A/(P^2)$, where A is cell area and P is cell perimeter. A circularity of 1 corresponds to a perfectly circular shape.

For LIVE/DEAD assays, cells emitting on each fluorescent channel (green/red) are counted for each condition (6 trials per condition), and percentages live/dead are calculated.

All statistical analyses are performed by multi-variate ANOVA using Prism software (GraphPad Software Inc., La Jolla, CA, USA). A Tukey's posthoc test is performed.

Results and Discussion

A microfluidic living cell array is introduced, comprised of 8 culture chambers that do not cross-communicate, are continuously perfused, and are designed to protect cells from undesired shear stresses. This unique set of capabilities is demonstrated by culturing alveolar epithelial cells in pairwise combinations of matrix (Ln or Fn) and soluble (TGF-β1 +/-) signal conditions within the array and observing certain cellular responses. Because TGF-β1 induces the expression of numerous soluble factors, including more TGF-β1,[35,121] cross-contamination among chambers in the array must be prevented for proper experimental control. Otherwise, cross-chamber contamination by soluble factors, including TGF-β1, would induce confounding phenotypes. The features introduced herein make it possible for well-controlled interrogation with different signaling combinations in a versatile, scalable, and rectangular chamber array format.

Device characterization

An array device loaded with colored dyes (water as carrier fluid) is shown in Fig. 4-3. Individual addressing offers the versatility to load different cells or adsorb different matrix molecules in each chamber (Fig. 4-3(b-c)). Also, individual addressing allows the experimentalist to fine-tune the cell density in each chamber by momentarily re-opening and closing chamber isolation valves to sample different sets of cells as they flow into the device; this process is essential to achieve uniform cell densities across chambers for the experiments performed in this work. Figure 4-3(d-f) shows how flow travels through the chamber. Flow enters from a common delivery channel and is expelled into a common exit channel that does not feed into other chambers. Careful inspection of Figs. 4-2 and 4-3 reveals that a 3-dimensional flow network is vital to prevent cross-chamber contamination in an array that is continuously-perfused and has a rectangular configuration. We use the strategies demonstrated in Fig. 4-3 to adsorb different matrix molecules by rows, perfuse TGF-β1-containing medium to specific columns, and attain

the desired cell densities during cell loading for the experiments summarized in the Methods section.

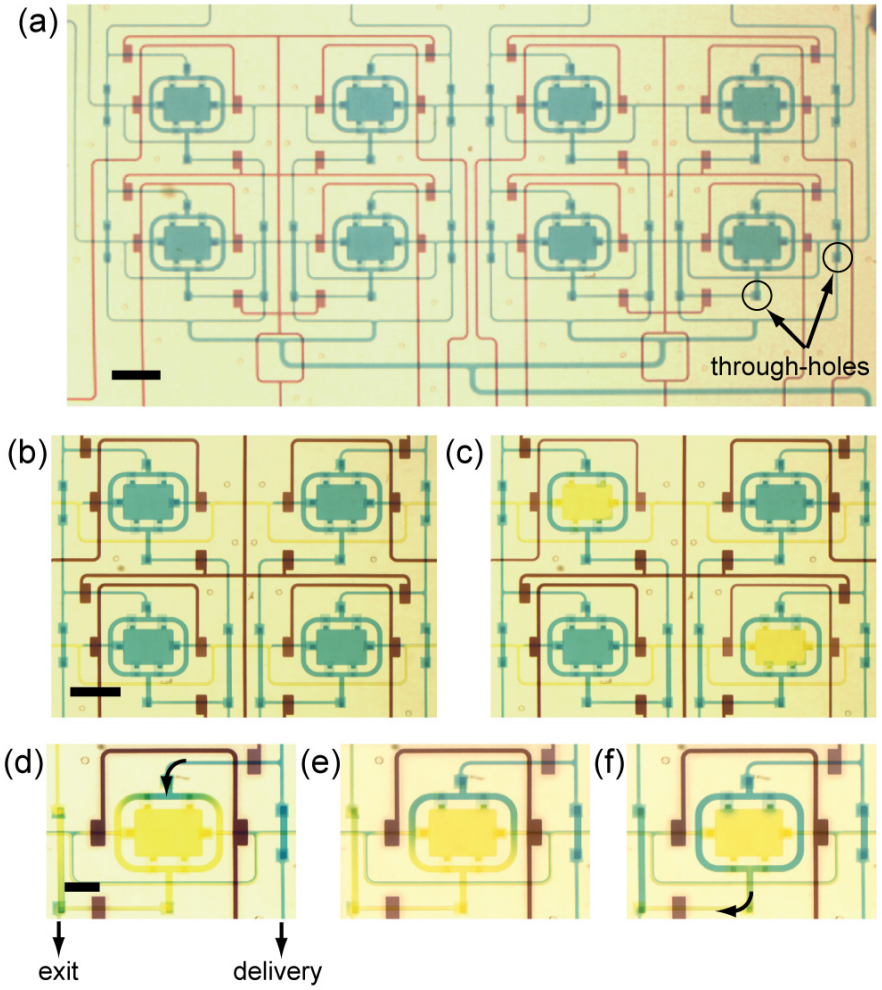

Fig. 4-3 Flow characterization with colored dyes. (a) Prototype device is a 2×4 chamber array. Blue dye loaded in 3-D flow channel/chamber network; darker square features indicate through-hole locations. Purple dye in valve control channels. (b-c) Chambers can be individually addressed with ECM, cells or assay solution. Yellow dye displaces blue dye in 2 chambers. (d-f) Cross-chamber communication avoided by routing flow through each chamber from delivery channel to exit channel (curved arrows). Upper-right valve is opened and blue dye flows through chamber. Images at 5, 10, and 20 sec after valve opens at experimental flow rate. Flow into the protected area is markedly slower due to high-resistance conduits. Scale bars: (a-c) 1000 µm, (d-f) 500 µm.

Figure 4-4 shows results of the chamber flow field simulation. Integration of velocities at selected boundaries shows that approximately 10% of the total flow through the chamber travels through the protected area (1-to-9, protected-to-total flow ratio). The balance of flow travels through the diverted flow channels. In addition, shear stresses are

calculated on the surface of the chamber at experimental flow rates. Too much flow can result in high velocity and high shear, which may induce confounding cellular responses; on the other hand, not enough flow will reduce nutrient and gas exchange, which may also affect cells adversely. Having the shielded chamber design allows sufficient convective mass transfer and yet avoids direct shear on the cells inside the chamber. Fig. 4-4 shows that shear stress on most of the chamber surface is less than 0.005 dyn cm^{-2}. As well, in interstitial spaces, shear stresses are expected to be small (compared to other *in vivo* contexts[113]), although the fibrous 3-dimensional extracellular matrix makes precise estimates of shear stress difficult.[122] Interstitial fluid velocities of less than 1 μm min^{-1} have been measured, which indicates very low flow (and correspondingly low shear).[123]

Because the array was designed as a prototype to demonstrate initial proof-of-concept, the array is small (2×4) relative to other arrays reported in literature. Scaling the array to larger sizes will require more control channels (and corresponding outlet ports) for the additional chambers. A device of greater scale may increase the complexity of the device, as discussed in Chapter 3 (Discussion); however, academic[92] and industrial[93] laboratories have shown that such additional complexity could be manageable.

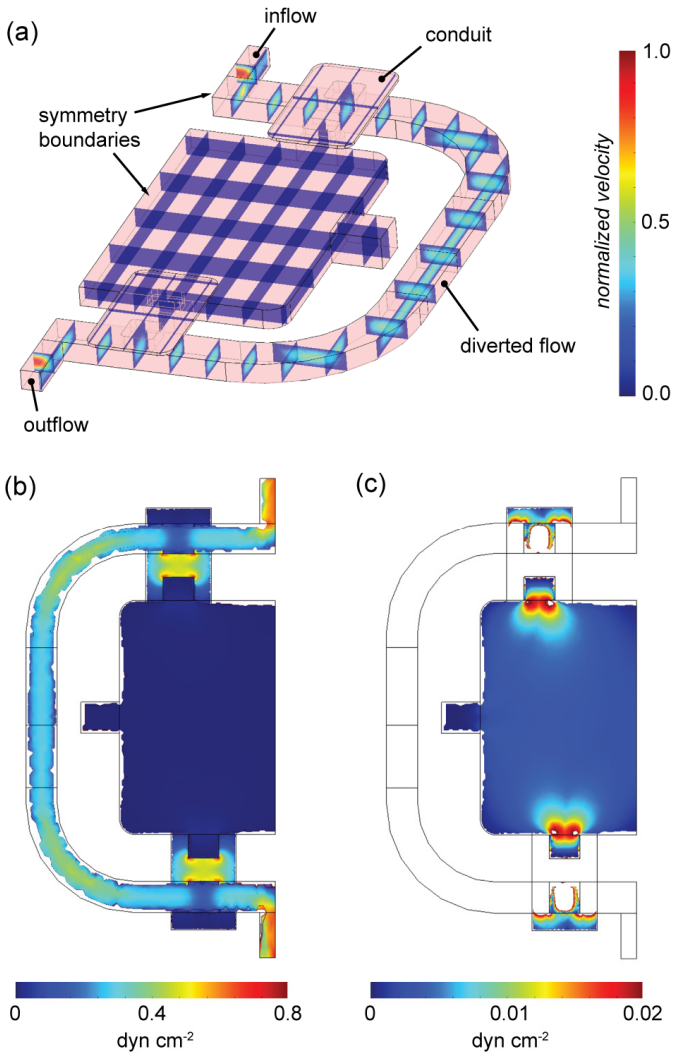

Fig. 4-4 Simulation of chamber flow field. (a) Oblique view of model geometry with solution shown in slice plot. Volumetric flow rate through diverted channel estimated as 90% of total flow (10% perfuses through protected area). (b) Shear stress field at floor of the chamber, solved using experimental flow rate. Shear on diverted surfaces is over an order of magnitude greater than in protected area. (c) Same solution as (b) with heat plot re-scaled to visualize shear stress in protected area; >85% of surface area less than 0.005 dyn cm^{-2}.

ATII response to soluble-matrix signal combinations

The array is used to elicit responses of ATII cells when subjected to four different soluble-matrix signal combinations, particularly ones that have been demonstrated to lead to three different cellular responses; specifically, maintenance of epithelial phenotype, cellular apoptosis, and epithelial-to-mesenchymal transition (EMT). EMT is a process where fully differentiated epithelial cells undergo a transition to a mesenchymal

phenotype, resulting in fibroblast-like and myofibroblast-like characteristics. EMT can be induced by a number of extracellular signals,[35] individually or in combination, and EMT is known to play a role in development and tumor invasion.[32,124,125] In addition, EMT is observed in response to epithelial stress or injury in a variety of tissues, where it is involved in repair and scar formation.[126,127] EMT in the context of epithelial injury and fibrosis is not well understood, and recent literature is just beginning to address its underlying mechanisms.[128]

With respect to the cell line used in this work, EMT of ATII cells has been implicated in idiopathic pulmonary fibrosis (IPF).[128] IPF is a condition characterized by excessive ECM deposition, resulting in interstitial scar tissue, loss of tissue compliance and ultimately decreased gas exchange across the alveolar epithelial barrier. Under normal conditions, ATII cells perform multiple roles in the lung associated with proper homeostasis and repair; in response to injury to the alveoli, ATII cells proliferate and differentiate into ATI cells. However, in fibrosis, ATII cells appear to undergo EMT, driving the cells toward a fibroblastic (mesenchymal) phenotype. This increases the number of ECM-depositing mesenchymal cells in the interstitial space and further perpetuates the fibrotic condition.

Elevated levels of active TGF-β1 and deposition of a provisional matrix rich in Fn are prominent components of pulmonary fibrosis, whereas a matrix rich in Ln is typical of homeostatic physiological conditions. Previous studies have demonstrated that ATII cells undergo markedly different behavioral responses to TGF-β1 depending on their underlying substrate.[128] In the presence of TGF-β1, ATII cells adhering to Ln-rich matrices undergo apoptosis, whereas on Fn-rich matrices they exhibit EMT-like events. Given the different possible responses to combinations of matrix (Ln or Fn) and soluble (TGF-β1 +/-) signals by ATII cells, such signal combinations were chosen as models for the proof-of-concept trials in this work to demonstrate usage of the chamber array. Chambers were incubated with Fn or Ln and perfused with medium with and without

active TGF-β1. All signal combinations were present in each array and repeated by subarray, and assays are performed to observe and measure responses. It should be noted that experiments are solely intended to elicit different responses for each signal combination for purposes of demonstrating array operation, and assays performed are not meant to represent the full set of assays required to conclude that specific phenotypes, such as EMT, are observed.

Cell morphologies in response to each signal combination after 48 hrs in culture are shown in Fig. 4-5. Cells cultured on Ln in the presence of TGF-β1 show either contracted morphology or elongated morphology. Cells cultured on Fn in the presence of TGF-β1 show similar elongation, resembling a fibroblast-like phenotype. For cells cultured on Fn in the absence of TGF-β1, a similar fibroblast-like morphology results. This is consistent with reports showing that Fn is capable of driving differing phenotypes for multiple cell types and inducing EMT in alveolar cells; however, it does not conclude a specific phenotype.[128-131] Cells cultured on Ln in the absence of TGF-β1 show a round, semi-cuboidal morphology and are arranged in an orderly monolayer, appearing to show an epithelial morphology on-chip, consistent with culture using conventional methods in cell culture flasks. In the Ln with TGF-β1 condition, cells with contracted, round morphologies exist with highly-elongated cells (fibroblast-like), causing the relatively wide variation in circularities for that condition. The differences in the means of observed circularities among the four signal combinations (pairwise comparisons) achieve varying levels of statistical significance, as shown in Fig. 4-5(e).

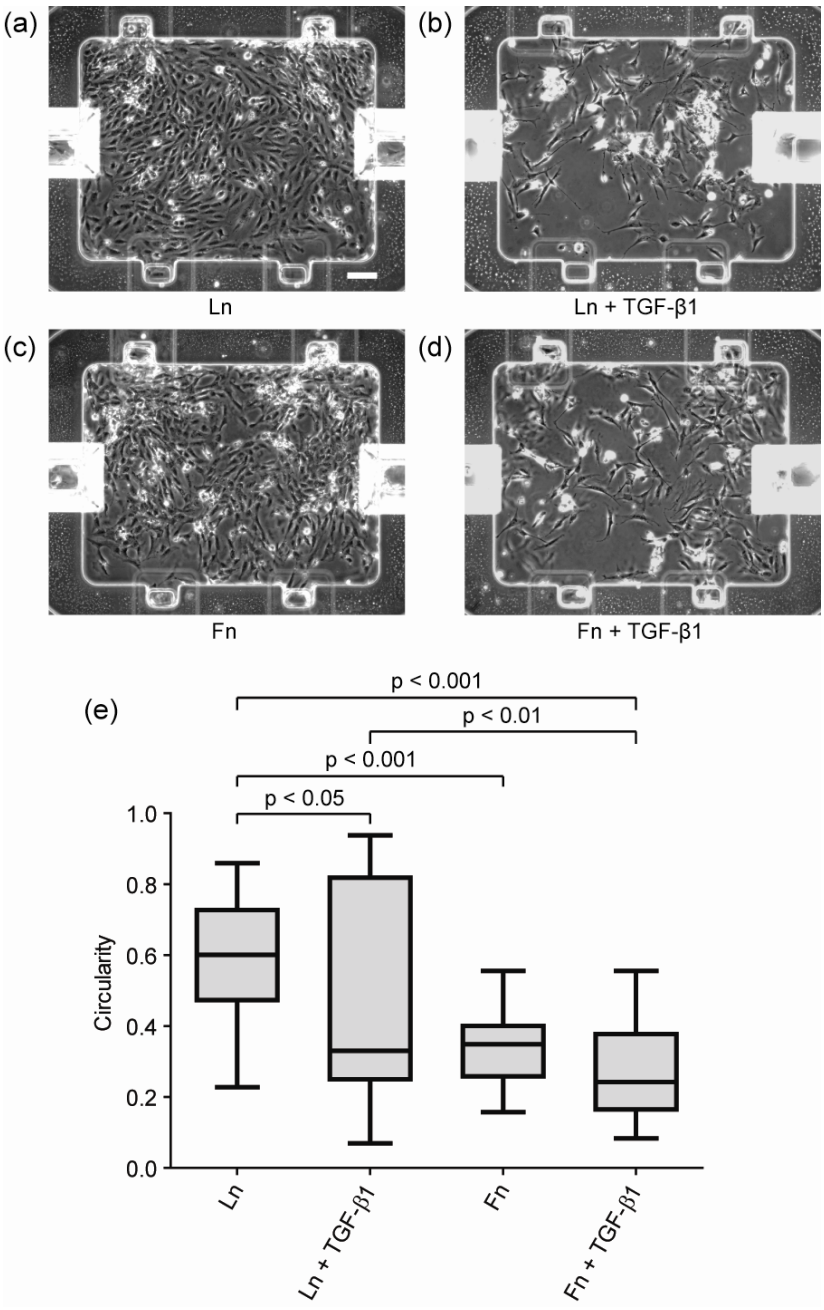

Fig. 4-5 Phase contrast images (representative) of ATII cells after 2 d culture. Matrix and soluble factor signaling combinations of (a) Ln, (b) Ln + TGF-β1, (c) Fn, (d) Fn + TGF-β1. Monolayer with extensive cell-cell contacts suggests epithelial phenotype in Ln condition. Lower relative density suggests decreased proliferation and/or apoptotic events for Ln + TGF-β1 condition. (e) Box plot of cell circularity for each signal combination. Calculated from traces of 30 randomly selected cells (3 trials, 10 per trial) for each signal combination. Boxes span 25th to 75th quartiles (median line inside) with lower and upper extreme values noted by whiskers. Significant p-values in brackets. Scale bar 100 μm.

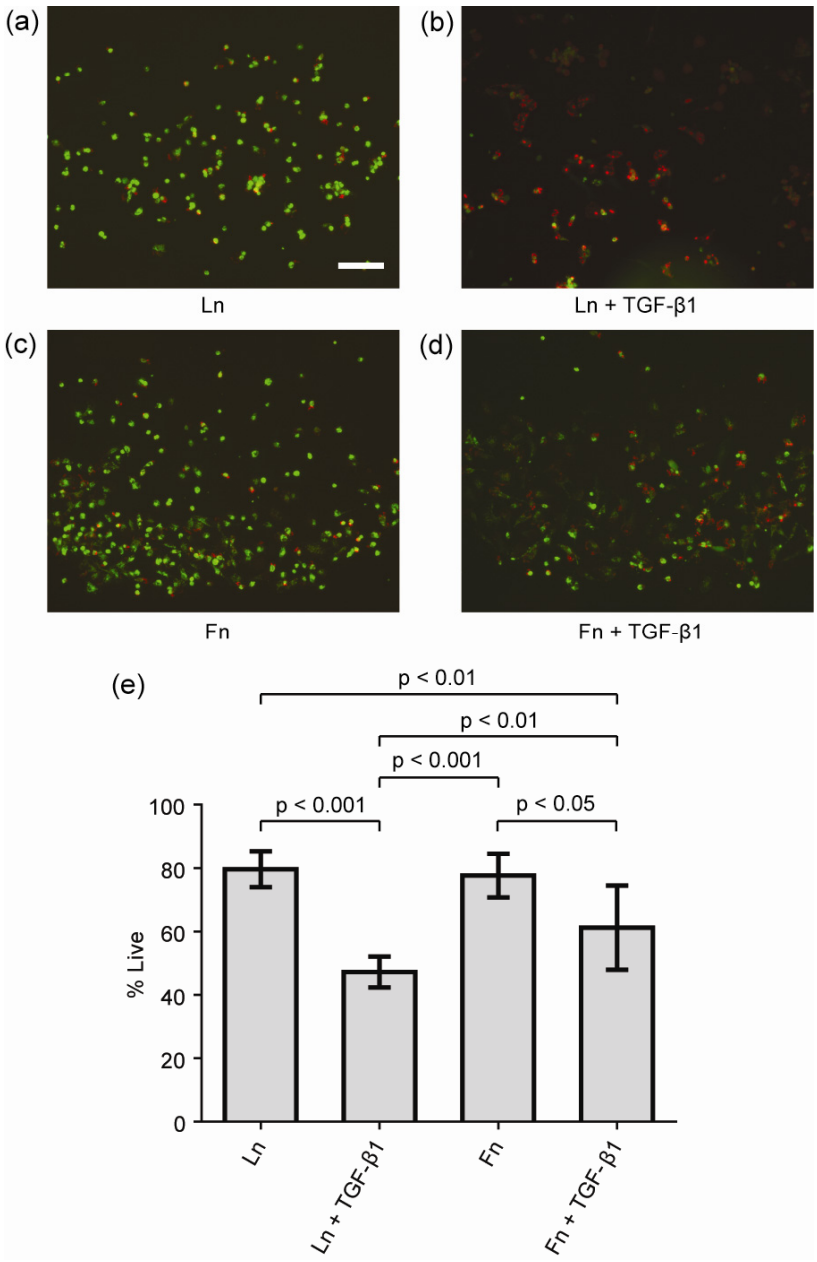

Fig. 4-6 LIVE/DEAD fluorescent staining of ATII cells after 2 d culture. Representative fluorescence images (green/red composite overlays) showing entire chamber for each matrix and soluble factor signaling combination: (a) Ln, (b) Ln + TGF-β1, (c) Fn, (d) Fn + TGF-β1. (e) Percentage of live (green) cells for each condition (6 trials each); error bars show SD. Significant p-values in brackets. Scale bar 100 μm.

To quantify cell viability for each combination of soluble and matrix cues, cells are stained with LIVE/DEAD fluorescent probes (Fig. 4-6). Without TGF-β1, cells are predominantly viable. For conditions perfusing TGF-β1, larger fractions of cells are stained with the "dead" stain (red stain, Fig. 4-6(b) and 4-6(d)). The greatest "dead"

staining is measured for cells on Ln in the presence of TGF-β1; if the stain is correctly indicating cell that are dying, it would be consistent with a previously mentioned report.[128] However, to definitively ascertain whether cells are dying, a number of other assays must be performed (see Limitations subsection).

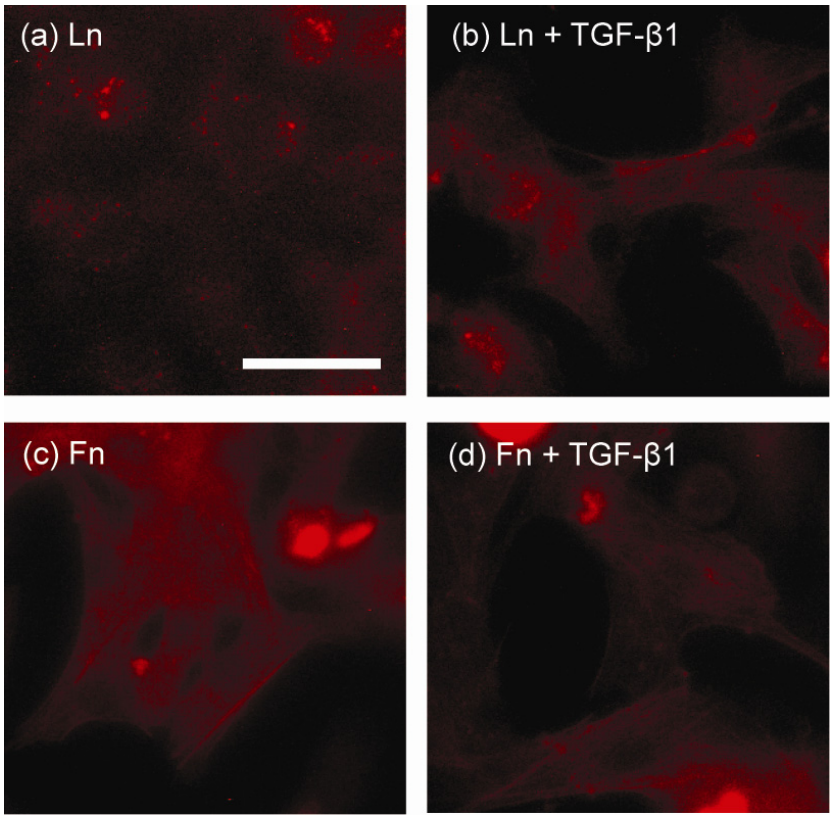

Fig. 4-7 Cytoskeletal staining of ATII cells after 2 d culture. False color fluorescent images of F-actin stained with Texas Red-phalloidin for each matrix and soluble signaling combination: (a) Ln, (b) Ln + TGF-β1, (c) Fn, and (d) Fn + TGF-β1. Possible stress fiber formation prominent in Fn conditions (with and without TGF-β1). Scale bar 50 μm.

To further characterize the morphological differences observed for each signal combination, cytoskeletal organization and stress fiber formation is visualized in cells by staining F-actin with Texas Red phalloidin (Fig. 4-7). Stress fiber formation is a direct indicator of cell contractility and indirect indicator of mesenchymal-like phenotypes. There appear to be qualitative differences among some conditions. Lines of staining are observed in the two combinations with Fn (with and without TGF-β1) (Fig. 4-7(c-d)). In

contrast, diffuse and spotty staining is observed in cells on Ln (no TGF-β1) (Fig. 4-7(a)); no lines of staining are evident.

Cells are also stained for the presence of epithelial cell-cell junctions. Junctions are marked by cell-cell adhesion proteins (e.g. E-cadherin) concentrated at cell edges. To visualize E-cadherin, cells are immunofluorescently-labeled and imaged at each condition (Fig. 4-8). Labeling of E-cadherin in the three combinations with Fn and/or TGF-β1 (Fig. 4-8(b-d)) appears to show nuclear localization and diffuse staining throughout the cells. ATII cells with epithelial characteristics would not show such staining, but instead they would show strong localization of staining at cell-cell junctions.[132,133] The Ln (no TGF-β1) (Fig. 4-8(a)) condition typically shows slightly less staining throughout the cell and occasional localization of E-cadherin at cell-cell contacts and cell edges, suggesting a qualitative difference between the Ln only condition and other three conditions.

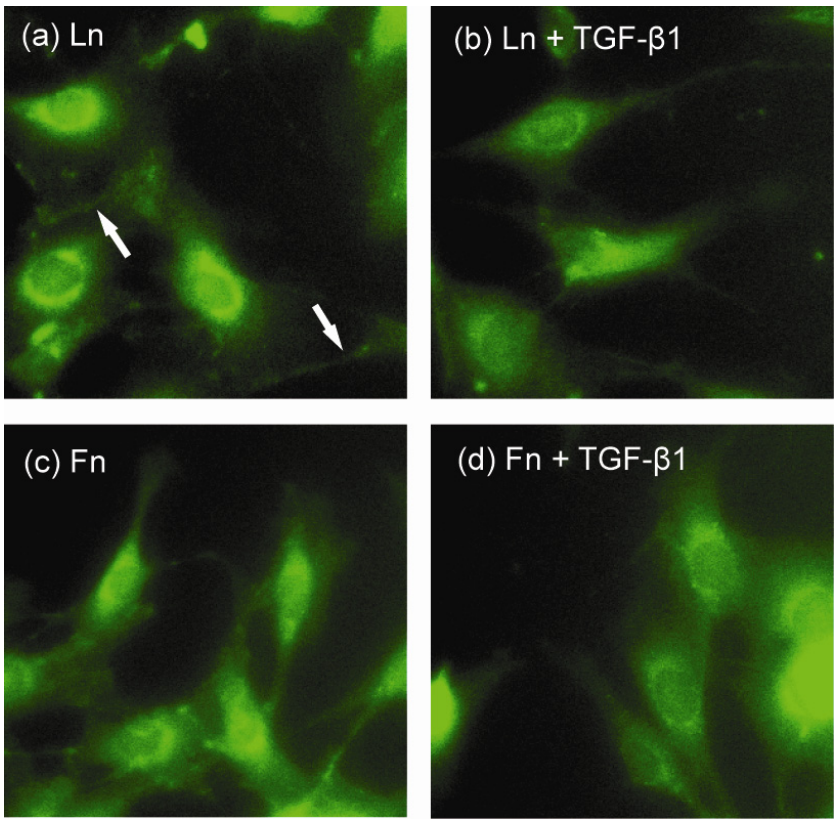

Fig. 4-8 Cell-cell junction formation of ATII cells after 2 d culture. False color images of immunofluorescently-labeled E-cadherin. Arrows in (a) indicate localization of E-cadherin at cell-cell contacts and cell edges. Scale same as in Fig. 4-7.

Limitations of Data and Confirming Phenotypes

Taken together, the data suggest differences among the four conditions as measured by circularity and LIVE/DEAD staining, as well as qualitative differences in cytoskeletal staining and E-cadhering staining. However, the data are not adequate to conclude that particular phenotypes are observed. For example, although cells undergoing apoptosis may exhibit greater membrane permeability, which LIVE/DEAD staining is intended to indicate, apoptosis must be confirmed through assays that complement the cell permeability test. Such additional assays include caspase activation assays, DNA fragmentation assays, and annexin V staining. Similarly, morphological readouts (circularity/elongation) and F-actin staining are not adequate to conclude whether one observes a mesenchymal phenotype; assays to detect expression of a variety of mesenchymal markers, such as α-smooth muscle actin, fibronectin, N-cadherin, and vimentin, must be performed. Furthermore, morphological readouts and the staining of E-cadherin are not adequate to confirm the existence of an epithelial phenotype. The expression of other surface marker or internal markers is required, such as epithelial cell adhesion molecule (EpCAM) and various cytokeratins.

Additional assays required to confirm specific phenotypes (or phenotype transitions like EMT) could be facilitated by an array with more chambers. Because the chamber array in this work is efficiently scaled and can address specific chambers (individually, by rows, by columns or by subarray), additional assays and required replicates could be performed in a single, scaled-out array.

Regarding the quality of assays performed, the F-actin and E-cadherin staining could be improved. Visualization of both stains could be improved by using a camera with higher resolution and lower background noise. For F-actin, a brighter, higher-affinity stain could be utilized, such as an Alexa Fluor®-based stain. Both stains could

be improved by further optimization of the protocol. For E-cadherin, the permeabilization agent and incubation time, as well as the times for primary and secondary incubation, most likely require further refinement. It should be noted that optimized protocols from a well plate or flask may not be applied with the same success in microfluidic chambers. The difference in size scale (chamber volumes are 37.5 nL) could affect incubation times due to changes in stain/antibody depletion and transport.

Chapter Summary

In this work, a prototype microfluidic chamber array is designed to combine three attributes: (i) continuous perfusion of media through chambers, (ii) a channel and chamber network that forbids cross-chamber communication/contamination, and (iii) low shear stresses on cells in the chambers. The array can also be scaled in both the x- and y-directions and provides considerable versatility regarding individual chamber, row, column, and subarray addressing. The combination of three attributes, scalability, and versatility is novel to microfluidic chamber arrays. The technology that enables such characteristics is a 3-D flow network (vertical layer-to-layer interconnectivity) that is constructed using the fabrication method developed in Chapter 3.

Experiments are performed whereby ATII cells are cultured in four different soluble-matrix signaling combinations to demonstrate the operation and application of the prototype array. Quantitative differences in responses to signal combinations are observed via morphological readouts (circularity) and LIVE/DEAD staining, while qualitative differences are visualized via F-actin and E-cadherin staining. In addition, limitations of the data in confirming phenotypes are discussed.

This work tests the array as a unique platform to culture cells under combinations of signals, and experiments suggest that the array can provide days-long culture (2-4 days) conditions and elicit cellular responses comparable to conventional culture and imaging. Furthermore, the array allows for replicates and controls to be perform on the

same chip at the same time. The array architecture is particularly well-suited to present soluble-matrix signal combinations in order to ascertain differences in cellular response. Moreover, the device can be extended to other cell types and transitional phenomena.

Further Work

Currently, the size of the array is small (8 chambers). Further scaling of the array would not require more alignment steps; however, more flow ports and valve control channels will be required (see Discussion on scaling in Chapter 3). To achieve the high versatility demonstrated in the prototype device, every 4 new chambers would require 5 more valve control channels and 2 additional flow ports. No additional exit ports or cell/ECM loading ports would be required, so long as scaling occurs in the x-direction. For scaling in the y-direction, every new row of chambers would require 2 additional cell/ECM loading ports. The number of valve control ports could be reduced, depending on the level of specificity required in chamber addressing (individual, row, column or subarray).

A potential challeng of scaling is that alignment of PDMS may become more difficult, since it is elastomeric and stretchable. Thus, small stresses could introduce large strains across die that are relatively large. In this work, the 8 chamber array is contained in a PDMS footprint of 24 × 24 mm (roughly an inch squared). At that footprint, stretching did not appear to significantly affect alignment; nonetheless, alignment rework due to stretching (slight observed warpage) does occur occasionally. It is conceivable that another 2 rows of chambers could be added to the same footprint (making a 16 chamber array). Further scaling must take into consideration alignment tolerances and constraints. Scaling is not inconceivable, as multilayer (non-3-D flow) PDMS microfluidic devices are being made commercially,[93] which may speed the invention novel "world-to-chip" interconnect technology to ease the scaling process. However, as scaling proceeds, new (and unexpected) challenges may emerge.

Also, the array must be further tested with a variety of cell lines and signal conditions for which responses are already known from conventional culture systems. This work only tested one cell line and four signaling conditions as a proof-of-concept for device operation. More testing and comparison of the responses will uncover previously unknown characteristics and limitations of either this microfluidic or conventional culture methods.

Provided the device is scaled to higher-throughput levels and validated against a larger set of signal conditions and cell lines, massively parallel interrogation of soluble-matrix signaling could be performed to uncover new mechanisms by which cell fates and phenotypes are determined in embryonic development, cancer, fibrosis, tissue repair, and other soluble-matrix contexts.

Table 4-1 Chapter summary.

advances / contributions
1. device: novel combination of three attributes, as well as x-y scalability and versatile addressing (chamber, row, column, subarray), in a microfluidic chamber array *   **(a) continuous perfusion**   **(b) cross-chamber communication/contamination forbidden**   **(c) low shear stresses on cells in chambers**
2. application: first reported testing/proof-of-concept of a microfluidic device with a 3-D flow network for use as a cell screening platform *   **(a) 3-D channel networks in previous literature are for fluid flow demonstration only (no application)**   **(b) 3-D flow architecture in this work applied to array for culturing cells in different soluble-matrix signal conditions; different responses are observed among signal conditions**
challenges / limitations
1. current prototype array is small (8 chambers); greater scale is required to show viability as a screening platform, and new technical challenges may emerge as scaling is attempted (from Chapter 3)
2. array (and scaled-out versions) must be tested further with different cell lines and signal conditions to compare responses with conventional culture systems
3. data from trials in this work are insufficient to conclude specific phenotypes; more assays are required to confirm mesenchymal or epithelial phenotypes, as well as EMT-specific markers
4. protocols for F-actin and E-cadherin require improvemets; in general, staining protocols could be specific to microfluidics

* Note: Design, fabrication, and testing are published work.[95]

CHAPTER 5

MODULATING SOLUBLE GRADIENTS USING SEQUENTIALLY PULSED DELIVERY IN A MICROFLUIDIC CHAMBER ARRAY

A novel microfluidic chamber array is introduced that generates gradients intended for chemotaxis studies. The two core technologies upon which it is developed are sequentially pulsed delivery and a 3-D flow channel architecture. The two technologies combined enable the production of soluble concentration gradients with a unique and useful set of characteristics. Furthermore, the device can be efficiently scaled to encompass larger chamber arrays and is fabricated from a single material with a single alignment step. The gradients are characterized by fluorescence measurements, and the device is tested as a chemotaxis assay by applying a serum gradient over human breast cancer cells and measuring migrational and morphological responses.

Motivation: Gradients and Gradient-Generating Devices

The directed migration of cells, or chemotaxis, is a critical component of many processes in normal physiology and in disease. Such processes include embryonic development,[134-137] tissue repair,[138-140] immune surveillance,[141-143] and cancer metastasis.[144-146] Chemotaxis is guided by concentration gradients of extracellular chemical stimuli, where motile cells travel toward or away from higher concentrations of a chemotactic stimulus (chemoattractant or chemorepellant, respectively). For eukaryotic cells, chemotactic gradients are sensed both spatially and temporally through signaling networks that internally amplify the external gradient information.[147] These signaling networks orchestrate cytoskeletal organization, formation of pseudopodia, and morphological polarization in a manner that biases the movement of cells in the direction of the gradient.[147-151] Because chemotaxis is a highly complex and integrative

biomolecular-biophysical phenomenon, many of its features and mechanisms remain poorly understood, despite a tremendous expansion of knowledge in cell migration over the past two decades. Consequently, chemotaxis continues to be an actively-studied field, the results of which could ultimately lead to novel and more effective approaches to treat numerous diseases and medical conditions.[152]

To study chemotaxis *in vitro*, a variety of assays have been developed. Each type of assay utilizes tools and methods that embody a unique approach for establishing the assay conditions (i.e. gradient and cellular microenvironment), as well as observing, measuring, and characterizing cellular response. Traditional chemotaxis assays include the Boyden chamber (transwell assay),[153] Zigmond chamber,[154] and Dunn chamber.[66] Also of note are the under-agarose assay[155,156] and micropipette-based assays,[157-159] which permit greater control over gradient positioning and presentation of multi-directional combinatorial gradients. These systems have greatly contributed to our understanding of chemotaxis, and their usage continues to be popular today due to ease-of-use, scientific acceptance, and commercial availability.[160-163]

However, the capabilities of traditional assays are inherently limited in some key respects, one of which is gradient instability. The gradients of transwell, Dunn, Zigmond, and under-agarose assays are unable to stabilize because their sources and sinks force toward equilibrium, causing the concentration profile to continually evolve (rising and decaying) over time. As a result, assay times are restricted to a few hours,[161,163] and correlating cellular responses to specific gradient conditions is largely unfeasible. Traditional assays are also vulnerable to gradient instability arising from physical perturbations (e.g. mechanical, evaporative, and thermal), which can easily distort or destroy the desired concentration profile. In addition to gradient instability, the geometrical configuration and optical properties of popular assays (transwell and under-agarose) obstruct high-resolution, quantifiable imaging of single cells, limiting such assays to end-point or population-based analyses.

The emergence of microfluidic systems has led to considerable progress in chemotaxis assays. Because their fluid flows are laminar, microfluidic systems can generate predictable and stable concentration gradients, which can surmount the limitations of traditional assays or enable entirely new lines of study.[101,164] Furthermore, microfluidic systems have demonstrated the potential for massive parallelization and greatly reduced sample usage, leading to higher throughput and lower cost experimentation.[92,165-167] Microfluidic chemotaxis assays and gradient-generating devices take a variety of forms and approaches, and many of these are highlighted in reviews.[161,163,168,169]

Flow-Based and Free-Diffusion-Based Microfluidic Gradient Devices

Flow-based and free-diffusion-based systems are the two major categories of microfluidic chemotaxis assays,[168] and their characteristics play a crucial role in the formulation of this work's design objectives. Therefore, the driving mechanism, benefits, and limitations of both categories are described to provide a framework for our design rationale.

Flow-based systems rely upon diffusion among multiple parallel flow streams to produce gradients. The flow streams are loaded with media containing different signal concentrations, which is typically achieved by the use of an upstream mixing network that splits and recombines the flow streams over multiple generations. When the streams meet in a chamber, lateral diffusion between the streams produces a signal gradient perpendicular to the direction of flow. The flow-based concept is an elegant and seminal invention in microfluidic chemotaxis assays,[170] distinguished by the superb stability and predictability of its gradients. Hence, flow-based systems have been used to study cellular response to signal gradients in a broad range of contexts.[103,171-174]

Flow-based systems face a number of limitations, depending on study requirements. First, cells may exhibit undesired responses to shear stresses caused by the

flow streams that pass directly over them. Second, diffusion between flow streams causes the slope of the gradient to decrease with each downstream location in the chamber. This limits the number of replicate conditions/locations available per device (subject to flow rate and slope tolerance). Furthermore, it is difficult to create dense arrays of chambers with identical gradients in flow-based systems. The difficulty arises from the spatially changing gradient, which limits downstream arraying of chambers, as well as the upstream mixing network, which requires considerable on-chip space and can only feed into a single chamber at a time. Consequently, flow-based systems are not amenable to the construction of in-line or 2-dimensional chamber arrays that are desirable for high-throughput screening applications.

In contrast, free-diffusion-based designs produce a signal gradient by way of diffusion from a source to a sink across a central chamber, where cells are monitored. The source and sink are either flow channels (loaded with high and low signal concentrations, respectively) or passive reservoirs. The defining features of a free-diffusion-based system are porous barriers with high fluidic resistance, which partition the chamber from the source/sink. The barriers shield the chamber from convection; therefore, mass transport becomes diffusion-dominated, and at steady-state, a gradient is established. Free-diffusion-based systems have been developed using barriers that take a variety of forms, including microcapillary channels (or gaps),[175-177] membranes,[178-182] and hydrogels.[183]

Free-diffusion-based systems combine the benefits of a low shear microenvironment and a stable gradient. However, such systems can be limiting in two respects. First, the high fluidic resistance of the barriers can restrict the range of concentrations the gradient can span. Ranges that span roughly 0.35 to 0.70 normalized concentration (minimum to maximum) have been reported for microcapillary-based[177] and hydrogel-based[183] systems, while the balance of concentrations occurs within the barriers. Second, free-diffusion-based systems are often hybrid designs composed of

dissimilar components that are required to construct the porous barriers. Such hybrid systems could frustrate attempts to achieve cost-effective, high-volume manufacturing that is often necessary for successful commercialization. The needs of some chemotaxis experiments require low shear and the full range of concentrations in the gradient; hence, a new design is necessary.

Device Design

A prototype microfluidic device is designed with an in-line array of 6 chambers to study the migrational response of cells to soluble signal gradients. Figure 5-1(a) is a schematic of 3 chambers in the array, as well as their supporting channel network and integrated valves. The objective is to produce gradients that are fully stable and provide exceptionally broad spatial and temporal controllability to experimentalists. An additional and equally important objective is to present the gradients in a chamber array that can be efficiently scaled to larger in-line or 2-dimensional arrays while minimizing fabrication complexity (Table 5-1).

Table 5-1 Design objectives and corresponding features.

OBJECTIVE	FEATURE
general	❖ stable gradient ❖ low shear (convection-free)
gradients – temporal and spatial control	❖ switchable on-off ❖ capable of low basal concentrations ❖ adjustable curvature (linear to concave)
array – parallelization and throughput	❖ identical gradients across chambers ❖ efficient array scalability
fabrication – minimized complexity	❖ single material ❖ single alignment step

To achieve the objectives, the design makes use of a 3-dimensional channel architecture that implements sequentially pulsed delivery. Sequentially pulsed delivery

represents an approach to generating gradients that is markedly different from the approaches of flow-based and free-diffusion-based systems.

Sequentially Pulsed Delivery Concept

The concept of sequentially pulsed delivery is depicted in Fig. 5-1. Two input flows with different signal concentrations are positioned on each side of the chambers. Four stages of a flow pulsing sequence are shown, illustrating how the flows alternate on each side. Flows are stopped at the specified times by integrated monolithic valves.[83] The valves actuate and de-actuate in manner such that the flows never occur at the same time; when flow occurs on one side of the chambers, the other side is completely fluidically isolated with a closed valve. Hence, the trajectory of each flow pulse is confined to the channel on its respective side and does not penetrate into the chambers. This protects the chambers from cross-convection that would arise from asymmetries in pressure or fluidic resistance.

The purpose of alternating flows is to periodically replenish each side with its input concentration (Fig. 5-1(c)). Replenishments are frequent enough so that the concentration on each side is effectively constant, which in turn provides a steady driving force for diffusion across the chamber. Thus, a stable gradient forms.

Low Shear Microenvironment

The absence of cross-convection through the chambers is not only intended to aid in establishing a stable gradient, but also meant to create a microenvironment that is effectively shear-free (see Fig. 5-4). The objective is to better resemble physiological conditions for cells in interstitial spaces, stem cells, neurons, and other cell types that do not experience significant fluid flows. For these cell types, shear-induced responses could confound analyses or lead to cell damage and death.[113,184]

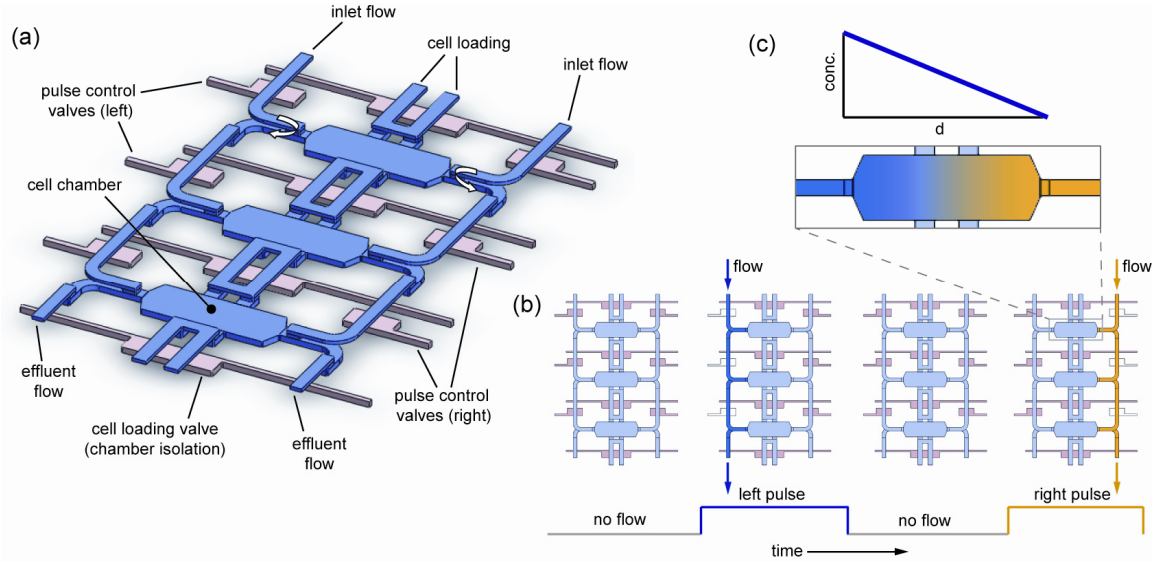

Fig. 5-1 Concept of sequentially pulsed delivery along three chambers in the array. (a) Chambers (blue), flow channels (blue), and valves (pink) form a 3-dimensional network. Media (with or without chemotactic stimulus) are input along sides, while cells are loaded via central channels. Flow travels along the sides of the chambers and vertically between layers via through-holes (curved arrows). Integrated valves, exclusive to the bottom layer, regulate flow in the top layer channels. (b) Four phases of the pulsed flow sequence. Sequence begins with all valves closed, then left side valves open to release flow pulse with high concentration (dark blue). All valves close again; then right side valves open release a flow pulse with low concentration (dark yellow). The sequence repeats throughout the experiment. (c) Flow pulses replenish each side with their respective input concentrations, establishing effectively constant boundary conditions. A gradient forms via diffusion-dominated mass transport.

Temporal and Spatial Control of Gradients

The objective of providing broad temporal and spatial control over gradients is addressed by three specific features. First, gradients can be turned on and off, which makes it possible to perform within-trial controls and enables studies of cellular adaptation and response to rising and dissipating gradients.[147] Gradients are turned on and off by flow selection routers that use integrated, on-chip valves to select which input flows are directed into the device (Fig. 5-2(b)).

Second, gradients are able to approach basal concentrations of zero. This is meant to address the limitation of restricted concentration ranges in free-diffusion-based designs, where minimum and maximum scaled concentrations in the chamber can be substantially greater than zero and lesser than 1, respectively, when measured in

normalized concentration (assuming zero for sink and 1 for source) at steady-state. Sequentially pulsed delivery is designed to enable studies to simulate physiologically relevant conditions using gradients that straddle low basal concentrations, while at the same time presenting a low shear microenvironment. Such conditions could test cellular response to an advancing front of diffusing signals from a distant point source (shallow gradient near zero) or a nearby point source (steep gradient near zero).[185,186] Gradients with low basal concentrations are possible because sequentially pulsed delivery eliminates the need for a porous barrier to shield the chamber from convection.

Third, the design makes it possible to adjust the curvature of the presented concentration profile. Although cells have shown migrational response to profiles of various shapes, eukaryotic cells have shown the greatest response to concave profiles with polynomial or exponential fits.[174,187] It is hypothesized that by modulating the valve actuation times in the pulsing sequence, the curvature of the profile can be adjusted from linear to concave. Valve actuation times are easily adjusted in a custom-written cycling program to test the hypothesis.

Chambers, Array, and Fabrication Approach

There are three important design objectives that relate to parallelization, scalability, and the fabrication approach of the device. First, all chambers in the array are intended to present identical gradient profiles, which enable replicate conditions and the potential for large-scale parallelization. Chambers with identical gradients are designed to address the aforementioned limitation of spatially changing gradients in flow-based designs, and they come as a result of the sequentially pulsed flows approach and a 3-dimensional channel architecture that delivers similar flow conditions to each chamber.

Second, the chamber array is designed to be conveniently scaled-out to larger in-line or 2-D arrays. Efficient scalability is facilitated by the 3-D flows architecture, which resembles roadway bridges and underpasses (bridge-and-underpass architecture)

(described in Chapter 3). The architecture enables flow streams to navigate over (or under) other streams by traveling vertically between layers, making it possible to construct intricate delivery networks that can weave around various obstacles (i.e. valves, chambers, other channels) to feed the proper flows to rows and columns of chambers. Scalability is designed into the device in anticipation of future design iterations that would offer greater experimental throughput.

Finally, the device is designed to be made of a single bulk material (poly(dimethylsiloxane) (PDMS)) and fabricated by way of a single alignment step. The objective is to minimize fabrication complexity in order to increase the likelihood of successfully realizing future versions of the device with massively scaled-out chamber arrays. In particular, we aim to avoid the use of hybrid structures (e.g. separate membrane or hydrogel components in PDMS), which is characteristic of many free-diffusion-based systems. Use of components made of different materials has led to multi-layer designs, requiring multiple stacking or alignment steps that interface hard and soft materials during fabrication.[178,179,181-183,188] Instead, this work employs a modified compression-molding technique and an all-PDMS thermal bonding process, requiring one alignment step (see Methods below, as well as full description in Chapter 3).

Methods

Fabrication

Devices are fabricated using soft lithography,[89] multi-layer PDMS thermal bonding,[83] and through-hole processing. Fabrication requires two master molds (masters A and B). Each master is a silicon wafer (100 mm diameter) with a photoresist pattern forming device features in positive relief. Photoresist patterns are realized using standard photolithographic methods.[90]

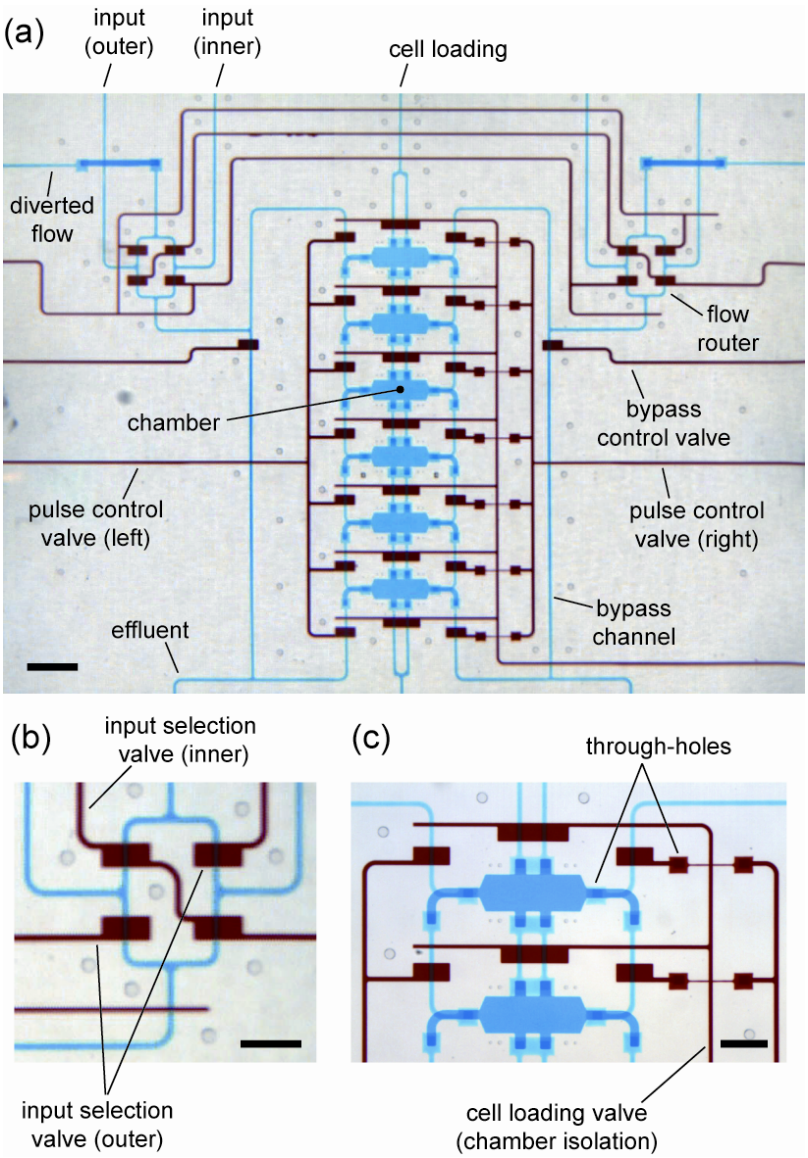

Fig. 5-2 Fully fabricated device loaded with colored dyes for visualization of chamber array and 3-D channel network. Blue dye is loaded in flow channels; red dye is loaded in valve control channels. (a) Overview of the device. Flow of inputs is selected by routers – one pair of inputs (inner or outer pair) is directed into the chamber network, while the other is diverted. Pulse control and bypass valves work synchronously to pass flow along chamber sides or to effluent (preventing over-pressurization). Pulse control comprises 7 interconnected valves on each side of chamber array. (b) Magnified view of the right flow router, indicating which valves direct inputs into chamber network. (c) Magnified view of chambers. Chamber isolation valves are permanently closed after cell loading. Scale bar is 1000 μm in (a) and 500 μm in (b) and (c).

Master A contains a two-layer pattern of SU-8 (MicroChem Corp., Newton, MA, USA), a negative-type photoresist. The first layer is 50 μm tall, and its features define the bottom device layer, containing chambers and parts of the channel network (flow and

valve). The second layer, which is patterned on the first layer, is 30 μm tall with features defining the middle device layer (i.e. through-holes). Master B contains patterns made of AZ P4620 (AZ Electronic Materials Corp., Branchburg, NJ, USA), a positive-type photoresist, that define flow and valve channels (25 μm tall). These channels have a semi-circular cross-section, allowing them to be fully closed by push-up valves located throughout the device.

Devices are made by aligning and thermally bonding two molded layers of PDMS (Sylgard 184, Dow Corning Corp., Midland, MI, USA) derived from masters A and B. Through-holes are realized by the modified compression-molding process described in Chapter 3.

Numerical Simulations

Flow Field and Shear Stresses

When flows are sequentially delivered, valves actuate and de-actuate in a manner such that flows on either side of the chambers cannot occur at the same time, i.e. when pulse control valves open to allow flow on one side, valves on the other side are closed. Thus, the chambers are protected from cross-convection, and shear stresses on cells attached to the surface of the chambers should be insignificant. To simulate this rationale, a 3-dimensional finite element model of the chamber is constructed using the COMSOL software package (Multiphysics 3.5a, COMSOL AB, Stockholm, Sweden).

The model geometry consists of a single chamber, along with side flow channels and connecting through-holes for layer-to-layer flow. The geometry is discretized into approximately 80,000 elements to ensure sufficient resolution to accurately model the curvature of parabolic flow profiles and minimize interpolation in solution plots. The portion of the sequence when flow is allowed along one side of the chamber is simulated by specifying all boundary conditions as no-slip, except for inlet and outlet boundaries at

the beginning and end of the flow path on a chosen side. Flow is driven by imposing a pressure drop between the inlet and outlet (positive pressure at inlet boundary and zero pressure at outlet boundary). The Navier-Stokes equations are solved to obtain the velocity field at steady-state, which is used to calculate shear stresses on the chamber's surface (Fig. 5-4).

Diffusion-Only Gradient Formation for Comparison with Experimental Data

A one-dimensional finite element model of the chamber is constructed using the COMSOL software package to simulate the formation of a concentration gradient by diffusion only. The boundary conditions are alternated between insulation and concentration to mimic a pulsing schedule where pulses are of equal duration (15 s each). The model geometry consists of a line, with each end corresponding to the side flow through-holes. A transient model is simulated following the equal pulse flow sequence. From time is 0 to 15 seconds, the left side boundary condition is set as concentration (arbitrarily set to 1) and right side boundary is insulated. Both boundaries are set as insulated from time 15 to 90 seconds. Right side boundary is changed to zero concentration (0) from time is 90 to 105 seconds, while left side remains insulated. Both boundaries are set as insulated again from time 105 to 180 seconds, which completes a single cycle. Diffusion equations are solved to obtain the concentration profile along the line over time. The 180-second cycle is repeated until steady-state profiles are achieved. Each time a boundary condition is changed, the resulting solution is stored and used as the initial condition for the following calculation/simulation. The diffusion coefficient used in the model is reported for 70 kDa dextran in PBS.[189]

Gradient Characterization Using a Fluorescent Marker

Soluble concentration gradients in the chambers are verified by way of fluorescence measurements. Dextran (70,000 MW) labeled with Oregon Green (D-7172,

Molecular Probes Inc., Eugene, OR, USA) is dissolved in aqueous buffer and pulsed along one side of the chambers. A sequence of fluorescent images (GFP filter set) is acquired to record the formation of the dextran gradient and the time to steady-state. Sequences are acquired at different flow rates and flow pulsing schedules to determine the effect of those parameters on the gradient (Fig. 5-5).

Cell Culture Off-Device

MDA-MB-231 cells (HTB-26, ATCC, Manassas, VA, USA), a human mammary adenocarcinoma cell line, are maintained in Leibovitz's L-15 medium (Gibco 11415, Invitrogen, Carlsbad, CA, USA) with 10% fetal bovine serum and 1% penicillin/streptomyocin. Cells are incubated at 37 °C in humidified air, and medium is changed every 48-72 hours. Cells are passaged with trypsin-EDTA solution (0.25% w/v trypsin and 0.53 mM EDTA, Gibco 25200, Invitrogen, Carlsbad, CA, USA), and the morphology and proliferation rate of cells is monitored over passages to verify consistent behaviour.

Prior to each trial, cells are serum-deprived by changing medium to L-15 with 0.1% w/v bovine serum albumin (BSA) (A9418, Sigma, St. Louis, MO, USA) (hereafter referred to as base medium) for 12 hours. Then cells are detached from their culture flask using EDTA solution (Versene, Gibco 15040, Invitrogen, Carlsbad, CA, USA). Once the cells are detached, excess base medium is added, and the suspension is centrifuged. The supernatant is aspirated, and the cells are resuspended in base medium to a density of ~1 $\times 10^6$ cells/mL and loaded into the device.

Experimental Setup

Device preparation, cell loading, and image acquisition are performed on a DM IRB/E inverted microscope (Leica Microsystems GmbH, Wetzlar, Germany) at 10× magnification in phase contrast mode (Fig. B-1, Appendix B). The device is mounted to

a motorized x-y stage (Ludl Electronic Products Ltd., Hawthorne, NY, USA) to translate it through a 6-position circuit to image each chamber in the array. Hollow stainless steel pins (L-shaped, 21G) are press-fitted into device ports and are connected to flexible plastic tubing (PE-60) for fluid and pressure delivery. Flow is driven by syringe pump (PHD 2000, Harvard Apparatus, Holliston, MA, USA). Pressurization of on-chip valves is regulated by off-chip miniature solenoid valves (Series 188, ASCO Valve Inc., Florham Park, NJ, USA) attached to a pressure source at 30 psig. Images are acquired using a digital CCD camera (ORCA C4742-95-12, Hamamatsu Photonics K.K., Hamamatsu City, Japan). Valve actuation, stage movement, and image acquisition are computer-controlled using a custom-designed interface written in the LabVIEW programming environment (National Instruments Corp., Austin, TX, USA).

Device Preparation, Cell Loading, and Incubation In-Device

Each device is pre-filled with phosphate buffered saline (PBS). To prevent on-chip valves from introducing gas bubbles into the device during experiments, each valve is filled with water. Fibronectin (Fn) (Gibco 33016, Invitrogen, Carlsbad, CA, USA) at concentration 8 μg/mL (in PBS) is introduced through the cell loading port. The chamber array is filled with Fn solution, and it is incubated at 37 °C for 1 hr to allow matrix molecules to adsorb to chamber surfaces. Following adsorption, the device is filled with BSA solution (2% w/v in PBS) and incubated at room temperature for 45 min to block surfaces from non-specific binding. Base medium (L-15 with 0.1% w/v BSA) is then introduced to the input ports and flushed through the device.

Cell suspension is then introduced into the cell loading channel and flowed through the chamber array by gentle pressure. Cells are stopped and confined to their chambers by closing the cell loading and pulse control valves. If the density or distribution of cells is unsatisfactory, the valves can be momentarily re-opened and closed to sample another set of cells.

The device is transferred from the microscope to an air incubator at 37 °C. Cells are incubated in the device for 12 hours to allow full attachment and spreading on the substratum prior to image acquisition.

Experiment and Image Acquisition

After incubation, the device is re-mounted to the microscope stage, and experimental media are introduced to the input ports. The medium entering the ports is either base medium or base medium loaded with FBS (16000, Invitrogen, Carlsbad, CA, USA), which is intended to be a chemotactic stimulus. The device is covered by an optically transparent enclosure (made of PDMS) into which is fed humidified air to prevent gas bubble nucleation in the device. A heating fan maintains the system at 37 °C.

Each experiment is made up of two stages. The first stage acts as a within-experiment control wherein the flow pulsing sequence is engaged but there is no FBS. Images of each chamber are acquired in 3 min intervals for 6 hrs. The second stage begins immediately after, wherein the flow pulsing sequence continues and a gradient of FBS is presented to the cells. The gradient is turned on by changing the selected input flows at the flow routers. Images are also acquired in 3 min intervals for 6 or more hrs, depending on experiment. Images for each chamber are then compiled into a sequence for image processing.

Image Processing and Cell Tracking

Cells are segmented in each image from their respective backgrounds for morphological and tracking analysis. We apply a heuristic involving image registration, image division, flattening, and cell segmentation through the use of MATLAB (The MathWorks Inc., Natick, MA, USA) and Image-Pro 6.1 (Media Cybernetics Inc., Bethesda, MD, USA) algorithms. Fig. 5-3 illustrates the process for a typical image. The image is registered to a background photo (cells absent) and divided by the background to

obtain a normalized image. The resulting image is processed through a flattening algorithm to reduce illumination irregularities present throughout the sequence and within individual frames (Fig. 5-3(c)). Programming code for segmentation algorithm is found in Appendix I.

To segment cells, we take advantage of the characteristics of phase contrast microscopy, where cell pixels follow a bimodal intensity distribution. Protrusions (cell membrane extensions) have lower intensities than the median, and therefore are segmented by selecting pixels below a predefined intensity threshold (protrusion threshold). The contours of cell bodies (cell bulk containing the nucleus) have higher intensities than the median, and therefore are segmented by selecting pixels above a separate predefined intensity threshold (body threshold). Segmented protrusions and cell bodies are found in Fig. 5-3(d-e), respectively. Extraneous debris is identified using an area filter and removed. Fig. 5-3(d) shows the resulting protrusions after morphological dilation using an isotropic structuring element to minimize cell fragmentation. The same morphological techniques are applied to the cell bodies in Fig. 5-3(e). The protrusion and body images (Fig. 5-3(d-e)) are superimposed, and the result (Fig. 5-3(f)) is dilated to further minimize fragmentation and then flood-filled to close gaps. Morphological erosion is applied to shrink the dilated segments, followed by an additional debris filter (Fig. 5-3(f)). The resulting image is overlaid on the flattened image to verify segmentation accuracy (Fig. 5-3(g)).

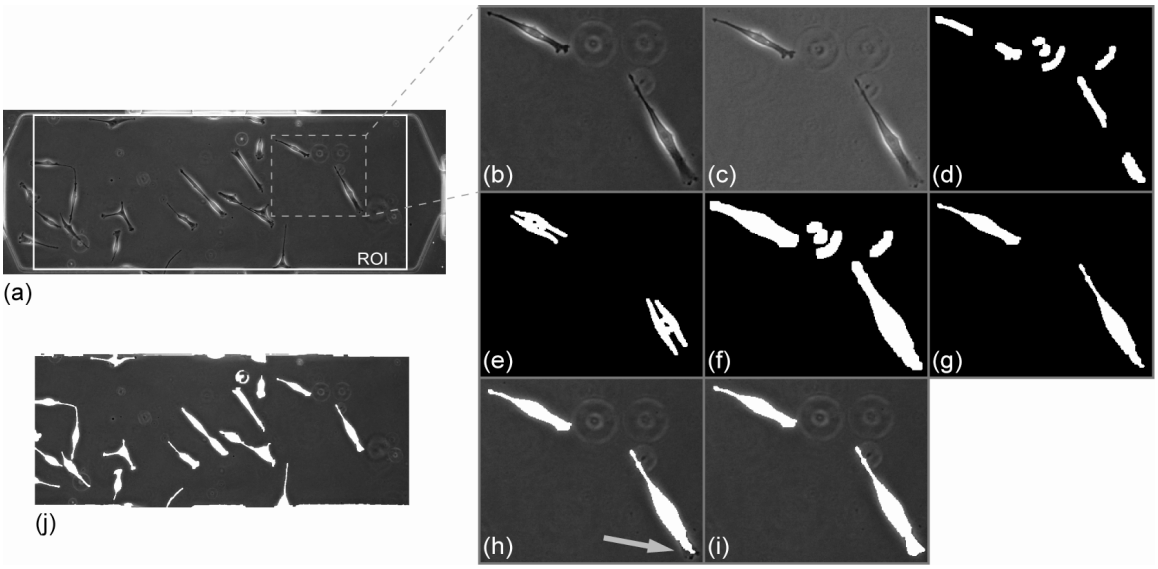

Fig. 5-3 Cell segmentation. (a) Representative phase contrast image, prior to cell segmentation, with applicable region of interest (ROI) (white border). (b-i) Magnified insets for clarity. (b) Original phase contrast image. (c) Background divided and flattened image. (d) Segmented protrusions, followed by dilation. (e) Segmented cell body contours, followed by dilation. (f) Superimposition of (d) and (e), followed by dilation and flood-fill operations. (g) Completed segmentations as a result of debris filter and erosion operations. (h) Segmented objects overlaid on flattened image from (c); under-detection denoted by arrow. (i) Hand-correction of under-detection. (j) Full image of segmented well. Scale: ROI rectangle is 1000 μm in x-direction.

After segmentation, cells are selected for analysis, hand-corrected, and tracked. Hand correction is applied to under-detected cells by manual placement of 4-10 sided polygons (Fig. 5-3(h)). Corrections apply to undetected protrusions and gaps in segmentation, and they are required for approximately 10-20% of all segmentations. The sequence is then tracked using the semi-automatic tracking algorithm in Image-Pro. The algorithm calculates trajectories for cell centroids as well as numerous morphological readouts. Data are then compiled for statistical analysis. Cells that make contact with other cells (or walls), divide, undergo apoptosis, or fail to attach are excluded from analysis (roughly 20-40% of cells in each well).

Data Analysis

Data are derived from 3 replicate trials (devices) with 6 identical chambers per device. Migrational and morphological data are collected from a total of 148 cells, which

generate 243 cell tracks. First, the chemotactic index (CI) of cells for the entire region of interest (ROI) for each trial is calculated (Fig. 5-8). Then, the ROI is divided into 4 spatial sections, and each data point for CI, speed, area, and circularity is calculated from non-overlapping subsequences of 7 consecutive photo frames, and each data point is binned into one of the 4 sections in the chamber (Fig. 5-9). Division into 4 sections is arbitrary; the chamber could be divided into more or fewer sections depending on whether there are enough cells (and corresponding tracks) in each section to produce results with meaningful statistical information. Area and circularity are calculated as the average from each set of 7 photos, and speed is calculated by dividing the root-mean-square displacement by the time interval spanning the 7 photos (18 min). CI is defined as

$$CI = \frac{d_{grad}}{d_{accum}},$$

where d_{grad} is the net displacement in the direction toward the gradient source (x-dimension) and d_{accum} is the accumulated distance traveled over the 7 photo set. Circularity is defined as

$$circularity = \frac{4\pi A}{p^2},$$

where A is cell area and p is cell perimeter.[190]

All statistical analyses are performed by ANOVA using Prism software (GraphPad Software Inc., La Jolla, CA, USA). Tukey's posthoc tests are performed.

Results and Discussion

In this work, a prototype device for the study of directed cell migration is designed, fabricated, characterized, and tested to measure chemotaxis with living cells. The device consists of an in-line array of 6 cell observation chambers, integrated on-chip valves, input selection routers, and supporting fluid delivery network. The objective is to create a microenvironment presenting soluble concentration gradients to study

chemotaxis that exhibits a unique and useful combination of characteristics that has not previously been demonstrated. The characteristics are: (i) fully stable signal gradients, (ii) no flow-induced shear stresses, (iii) concentration profiles that can approach a basal concentration of zero, (iv) gradients that can be switched on-off with minimal delay, and (v) concentration profiles whose curvature can be adjusted conveniently. Additional and equally important objectives are for the device to demonstrate (i) identical gradients in all chambers, (ii) efficient scalability to larger in-line or 2-D arrays, and (iii) a fabrication process requiring only a single alignment step. Two core technologies are developed and implemented in the device. First, sequentially pulsed delivery is used as the physical mechanism by which soluble gradients are generated. Second, a 3-D flow network is realized that enables the scale-out of chamber arrays for potentially large-scale parallelization.

Simulation of Chamber Flow Field

The purpose of simulating the chamber flow field is to calculate shear stresses on the chamber floor during normal device operation. In concept, the chamber design and use of sequentially pulsed delivery should prevent significant flow-induced shear stresses on cells during migration experiments. The motivation for engineering a microenvironment with minimal shear stresses is to provide an adequate model for physiological contexts where fluid flow is very small; such contexts occur in the interstitial spaces throughout connective tissue and in the brain.

A 3-D finite element model is used to calculate the velocity field when a flow pulse occurs on one side of the chamber. Since flow cannot occur on both sides simultaneously (by definition of sequentially pulsed flows), the model reflects the only situation where convection occurs in the chamber region. The side channels are designed so that flow approaches the chamber from an upper layer, travels vertically downward into a lower layer channel, and continues downstream in the same channel. The other

side of the chamber is fluidically isolated by integrated on-chip valves to prevent flow through the chamber.

The velocity plot of Fig. 5-4(a) shows the simulation of flow confined to one side of the chamber. The volumetric flow rate of 2.5 μL min^{-1} is chosen to model conditions in cell migration experiments. The resulting shear stress field on the chamber floor is plotted in Fig. 5-4(b), showing shear stresses less than 0.0005 dyn cm^{-2} across the entire chamber (heat plot) during pulse flow.

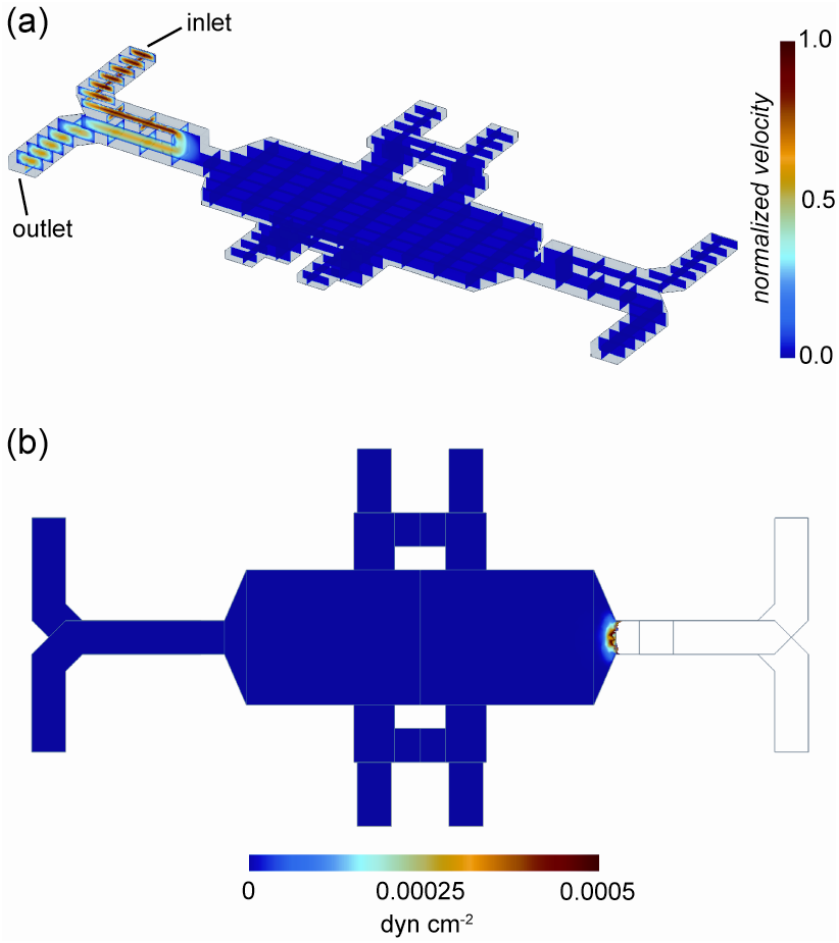

Fig. 5-4 Simulation of chamber flow field during a flow pulse. (a) Oblique view of 3-D model geometry with solution (velocity field) shown in slice plot. Heat plot visualizes how flow is confined to the path on the side of the chamber. (b) Shear stress field at the floor of the chamber, solved using a 2.5 μL min^{-1} flow rate (highest experimental flow rate) through the inlet and outlet. Shear stresses are very low in the chamber; less than 0.0005 dyn cm^{-2}.

In comparison, *in vivo* shear stresses of 10-100 dyn cm^{-2} have been reported on vascular endothelial cells in blood vessels (a high shear context), while less than 2 dyn cm^{-2} has been reported for hepatocytes (mid-shear context).[113] In interstitial spaces, shear stresses are expected to be smaller, although the fibrous 3-dimensional extracellular matrix makes precise estimates of shear stress difficult.[122] Interstitial fluid velocities of less than 1 μm min^{-1} have been measured, which indicates extremely low flow (and correspondingly low shear).[123] As well, human neural stem cells have been successfully cultured in microenvironments with shear stresses estimated at 0.0005 dyn cm^{-2}.[172] Therefore, the very low shear stresses shown in Fig. 5-4 suggests an assay platform whose most appropriate application would be to model interstitial and other low flow contexts (compared to other microfluidic gradient-generating devices).

Characterization of Gradient Formation

Four design objectives relate to concentration gradients generated in the device. They must be fully stable, switchable on-off, able to approach zero basal concentration, and adjustable in curvature. The intention is to provide unprecedented control and experimental versatility to researchers. To verify that the gradients meet the design objectives, they are characterized by observing the transport of fluorescently-labeled dextran dissolved in aqueous medium (PBS) undergoing sequentially pulsed flows. Experiments measured the evolution and stability of gradients by time-lapse fluorescence photography.

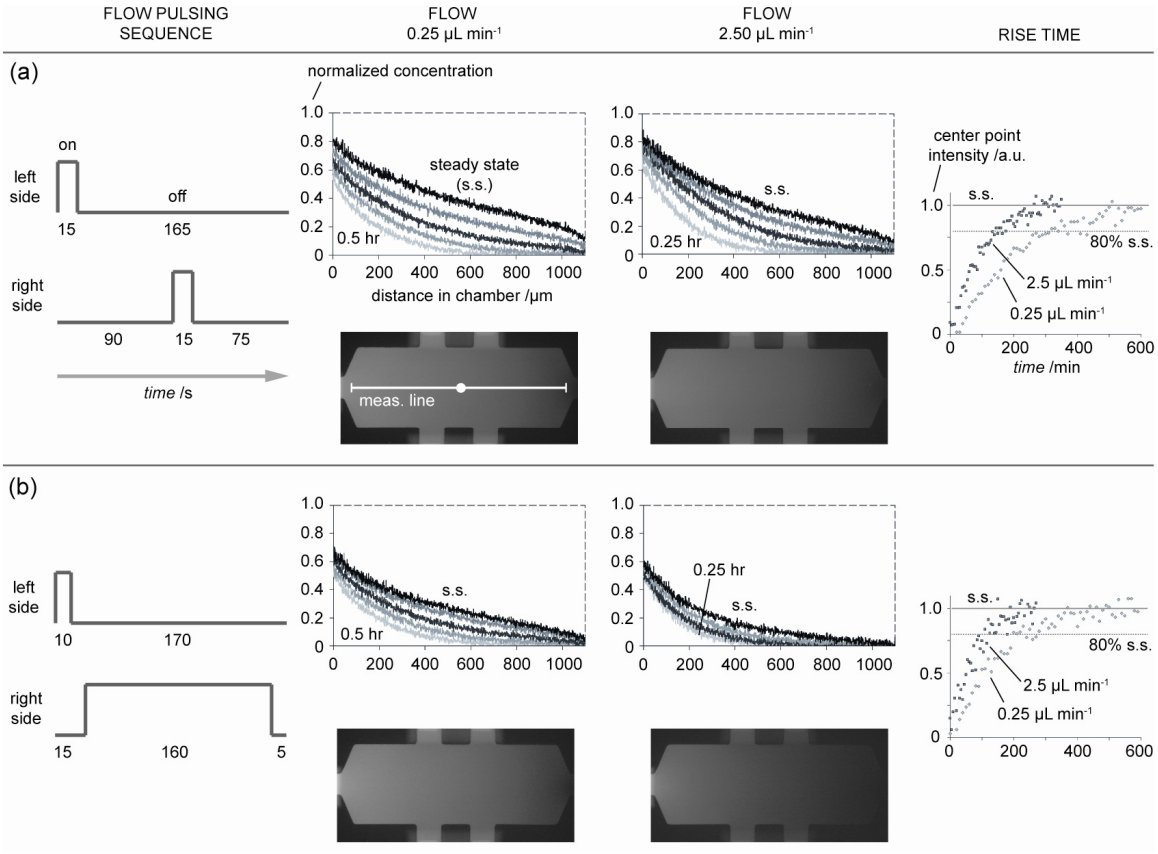

Fig. 5-5 Gradient formation and steady-state profiles measured via fluorescence imaging. Medium loaded with fluorescently-labeled dextran (70,000 MW) is pulsed along one side of the chambers. Results of four combinations of flow pulsing sequence and flow rate are shown. (a) A pulsing sequence with equal pulse times (15 s per pulse) generates a near linear profile at the lesser flow rate (0.25 µL min^{-1}) and slightly curved profile at the greater flow rate (2.5 µL min^{-1}). Fluorescence photographs of chambers at steady-state are shown; measurement line (1100 µm) indicates where intensity profiles are measured. Time-to-steady-state (rise time) as measured from the center point is shown far right column. The greater flow rate results in a faster rise time (time to 80% of steady-state ~120 min and ~300 min for 2.5 µL min^{-1} and 0.25 µL min^{-1}, respectively). (b) A pulsing sequence with unequal pulse times generates slightly curved profiles at the lesser flow rate and noticeably curved (and concave) profiles at the greater flow rate. Also, rise times generally decrease (~100 min and ~220 min to 80% of steady-state for greater and lesser flow rates, respectively). Curves for lesser flow rate (two left gradient plots) correspond to 0.5 hr, 1 hr, 2 hrs, 4 hrs, and steady-state (from bottom curve to top curve). Curves for greater flow rate with equal pulsing (upper right gradient plot): 0.25 hr, 0.5 hr, 1 hr, 2 hrs, and steady-state. Curves for greater flow rate with unequal pulsing (lower right gradient plot): 0.25 hr, 0.5 hr, 1 hr, and steady-state. Note: Rise times are demonstrative only, as they will vary depending on the molecular weight/size of the signal used in experiments.

Observations

Two parameters are investigated to determine their effect on the formation and shape of gradients. These are the flow rate and the pulsing schedule. The flow rate is

varied to determine if convective penetration into the chamber can assist (or disrupt) gradient formation. The pulsing schedule is varied to simulate unequal periodic concentration boundary conditions, particularly if a longer period for the sink side causes decay and loss of gradient stability or curvature of the profile at a new steady-state. Figure 5-5 summarizes the results; Fig. 5-5(a) (top row) shows results for a flow pulsing schedule where the left and right pulses are equal in duration, while Fig. 5-5(b) (bottom row) shows results for a pulsing schedule where the pulses on the right side (non-dextran side) are significantly longer than the left. Within each subfigure are concentration plots at two flow rates (0.25 μL min^{-1} vs 2.5 μL min^{-1}), and each plot shows multiple concentration profiles at different time points as the gradient forms from a zero concentration initial condition. The time-to-steady-state (rise time) at each condition is determined by measuring the fluorescence intensity in the center of the chamber at numerous time points as the gradient forms (right column of Fig. 5-5).

Near linear steady-state concentration profiles result from the equal pulsing schedule (Fig. 5-5(a), although the higher flow rate shows slight curvature at steady-state. This could be due to penetration of a convective component into the chamber. The time-to-steady-state (rise time) decreases significantly with the higher flow rate. In Fig. 5-5(b), the unequal pulsing schedule appears to maintain a near linear (slightly curved) steady-state concentration profile at the low flow rate; however, the profile shows dramatic curvature at the high flow rate. Instead of a linear fit, the profile exhibits curvature more akin to a polynomial or exponential function. Again, the higher flow rate decreases the rise time significantly. Comparing the rise time profiles in both pulsing schedules shows a slight decrease with the unequal schedule. Times to 80% of steady-state with the equal flow pulses are ~120 min and ~300 min for 2.5 μL min^{-1} and 0.25 μL min^{-1}, respectively. Corresponding values for the unequal pulsing schedule are ~100 min and ~220 min.

Therefore, the results suggest that the flow rate has a general effect on the rise time. Higher flow rates could enable slight convection to penetrate into the chamber, adding to diffusive transport. Also, there is a switch-like relationship between pulsing schedule and flow rate. That is, the pulsing schedule has little effect on the curvature at a low flow rate, but there is a dramatic effect on curvature at a high flow rate. Once again, this effect could be driven by the addition of a slight convective component to transport by the greater velocities. A more exhaustive screen of the parameter space could reveal the thresholds where the profile curvature shows greatest sensitivity to pulsing schedule-flow rate combinations. Gradient formation can be measured at flow rates spanning at least three orders of magnitude (e.g. 0.1 to 10 $\mu L\ min^{-1}$) at higher resolution with pulsing schedules scanning different left-right flow ratios. Changes to the duration of full periods should be investigated also.

Discussion

The ability to change the curvature of the concentration profile from linear to exponential is an important feature, as it enables the creation of a microenvironment that mimics diffusion from a point source (signal release) into an infinite reservoir (interstitial space). Although curved concentration profiles have been engineered using flow-based gradient devices,[174,187] the resulting microenvironment produces shear stresses due to the convection required for gradient generation. Furthermore, to switch between an exponential and linear gradient, flow-based systems require that the upstream mixing network be redesigned. At the same time, free-diffusion-based systems producing a stable concentration gradient are limited only to linear profiles. This work introduces a gradient-generating technology that exhibits both low shear and curved profiles, which could enable new types of studies that can model additional physiological conditions. In addition, changing between a linear and exponential gradient requires only a change in flow rate, rather than a different device design.

The results also demonstrate that the gradients can be switched on and off. In order to perform the characterization, a flow selection router upstream of the chamber array first chooses a flow stream without fluorescent dextran, and upon initiation of the photo sequence, the router selects the input streams with the probe. The ability to switch gradients on and off could enable studies of cellular response to rising and dissipating gradients or repeated bursts of gradients, which could shed light on adaptive cellular decision-making processes.[191,192] Also, gradient switching provides a within-trial (within-population) control condition, enabling the experimentalist to collect response data before and after initiation of the gradient. This could increase the total amount of data for the same trial, saving time or enabling more experimentation with a given number of cells. However, the utility of gradient switching is limited by the rise time, which in turn is determined by the diffusion coefficient of the signal. Rise times should be appropriate to the cell system and response being studied, as each cell type and response could operate at differing time scales.

The rise times are measured using 70 kDa dextran, which is chosen as a representative molecular weight. However, external signaling proteins vary significantly in their molecular weights; for example, epidermal growth factor (EGF) is ~6 kDa, while platelet-derived growth factor (PDGF) is ~25 kDa, and fibronectin is ~440 kDa. According to the Stokes-Einstein relationship and assuming that proteins are spherical (simplifying assumption), the diffusion coefficient is inversely proportional to the cubed root of molecular weight. Taking EGF as an example, its rise time would be less than half (0.44) that of the dextran, assuming transport is purely diffusive. Therefore, the rise times reported in these data are solely demonstrative, as it will vary depending on the size of the signal of interest.

The results show the attainment of two other objectives that are critical to the suite of capabilities offered by the device. First, the rise time plots in Fig. 5-5 show that intensities approach a steady-state, which demonstrates gradient stability. Second, basal

concentrations can approach zero, which is most evident from the high flow rate or unequal pulsing conditions. This is significant because it has been shown that some cells respond best to shallow gradients with low basal concentrations,[185,192] and producing microenvironments that mimic such gradients, while at the same time presenting low shear, may position the technology in this work as a key tool to query cellular response under such conditions. Other microfluidic platforms generating stable gradients must trade-off the conditions; free-diffusion-based systems are low shear, but cannot reach zero concentration, while flow-based systems can achieve zero concentration, but introduce shear.

Comparison of Concentration Profiles to Diffusion-Only Model

Fluorescence profiles are compared to a diffusion-only model (see Methods section for model details) to ascertain whether gradient formation is purely diffusion driven. Figure 5-6 shows comparisons at two different flow rates (0.25 and 2.5 μL min^{-1}). The measured plots are copies of the plots in Fig. 5-5(a) (top row with the equal flow pulsing schedule). Figure 5-6(a) shows that the model and experimental plots match well as the gradient forms at the 1 and 2 hr time points. At later time points (4 hr and steady-state), the model plots approach a linear shape, which is expected for a diffusion-only model. However, the measured plots deviate slightly from linearity (exhibiting some concavity). In Fig. 5-6(b), measured plots rise significantly faster than those of the model. This can be attributed to the greater flow rate (2.5 μL min^{-1}, 10× greater than in Fig. 5-6(a)). However, at steady-state, the measured plot falls below the model, showing more concavity than in Fig. 5-6(a).

The rough agreement between measured and modeled plots during gradient formation in Fig. 5-6(a) suggests that at low flow rates (0.25 μL min^{-1}), the transport of soluble species is mostly diffusion-driven. At higher flow rates, the dramatic differences in measured and modeled plots suggest that transport is driven not only by diffusion, but

also by convective effects. Such effects also appear to increase the concavity of the measured plots as flow rate is increased. Although convection could be a component in the transport, simulation of the flow field at the high flow rate (2.5 μL min^{-1}) shows that shear stresses remain low on the chamber cell culture surface (Fig. 5-4). Error in the measured plots could come from fluorescence measurement variation, as well as general chamber-to-chamber or device-to-device variation, which is discussed in the following section. Error could also be caused by use of an inaccurate diffusivity in the model.

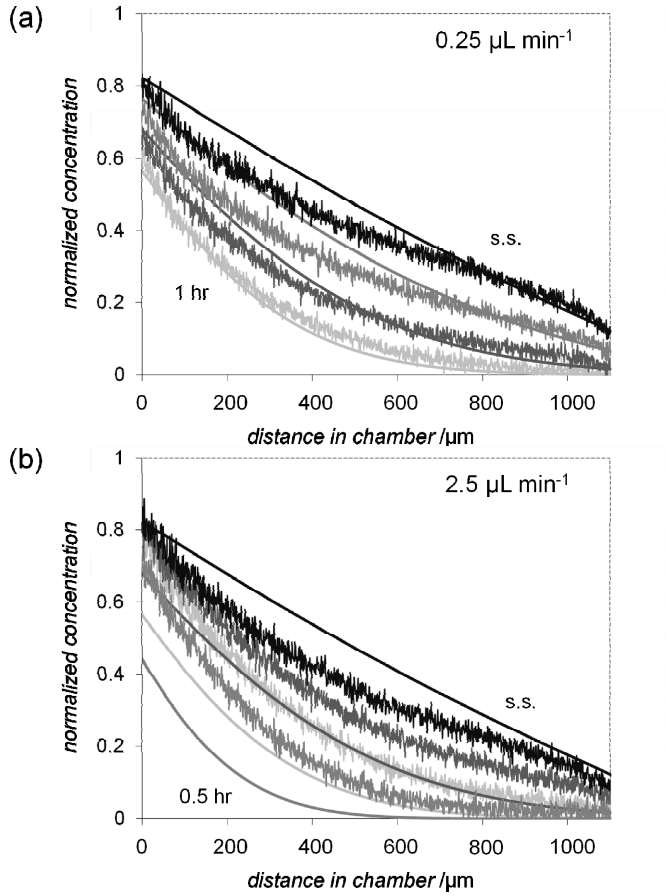

Fig. 5-6 Comparison of concentration profiles for numerical modeling and measured data. Measured results (noisy curves) of flow pulsing schedule in Fig. 5(a) and two flow rates (0.25 μL min^{-1} and 2.5 μL min^{-1}) are shown in comparison with a one dimensional numerical model of diffusion only (smooth curves). (a) The measured pulsed data corresponds with the model at the lower flow rate during the initial start up. As the plots approach steady state (s.s.) the diffusion model approaches a linear plot and the measured data still exhibits a slight concave shape. (b) Measurements at the higher flow rate produce curved profiles that deviate noticeably from the diffusion model after the first hour. Note: Corresponding time points for measured and modeled plots share the same gray level. Plots in (a) correspond to 1 hr (bottom), 2 hrs, 4 hrs and steady-state. Plots in (b) correspond to .5 hr (bottom), 1 hr, 2 hrs and steady-state. Model uses diffusion coefficient of 70 kDa dextran as measured in literature (2.3×10^{-7} cm^2 s^{-1}).[189]

Concentration Profile Variation

Designing chamber arrays with identical gradients is an important objective, as it can address the limitation in flow-based systems where the concentration profile changes from location to location in the downstream direction. Identical gradients in all chambers enhances the replication (and hence parallelization) potential of the array. In practice, variation in concentration profiles exists, and it can be treated in two ways: (i) chamber-to-chamber variation (within a device) and (ii) device-to-device variation. Observations of both types of variation are summarized in Fig. 5-7. Concentration profiles of all 6 chambers across 6 devices are measured at the experimental pulsing schedule and flow rate condition (see Fig. 5-5(b), unequal pulsing at 2.5 μL min^{-1}).

A possible cause of chamber-to-chamber and device-to-device variation are obstructions in the upstream or downstream flow channels feeding the chambers, which could be caused by small fabrication defects or particles that flow into the devices and get lodged in the flow path. Such events could cause the flow rate to deviate from the intended target, making the flow rates on each side of chambers different, leading to shifting or bending profiles. In addition, fluorescence measurement error may be contributing to the variation, such as fluorescent light source fluctuations and camera noise. In addition, inexact alignment of normalizing images (full bright and full dark) to measured images could cause registration/shift errors.

Comparison of the measured variation with other methods or devices is difficult. The gradient in transwell (Boyden chamber) assays typically spans only 10 μm, the profile is not stable, and (because of its vertical orientation and small pore sizes) it is difficult to measure its concentration profile. Other standard gradient-generating tools, like the Zigmond or Dunn chambers also cannot produce stable profiles; thus, deciding which profile (time point) is used for comparison may be subjective. Moreover, literature does not report the variation in profiles in microfluidic gradient devices. From an

engineering standpoint, it is reasonable and ultimately necessary to understand device variation; however, in microfluidics, such analysis has not yet become a standard procedure. One could attempt to construct devices reported in literature and perform experiments to determine the variation, but such activities could prove time-consuming and difficult to replicate, owing to the experience and specific expertise required for such work.

For the chambers and devices in this work, knowing the upper and lower bounds of concentration (based on SD or other % confidence intervals) could be helpful to develop rules for the size of spatial sections (resolution); based upon the variation in concentration at a specific x-location, x-tolerances (+ and -) could be established to define what the experimentalist deems as an equivalent concentration condition. Thus, sections could not be made smaller than the span of such tolerances; if so, adjacent sections could be considered redundant conditions.

Another way to look at profile variation is from the cell standpoint. It has been reported that eukaryotic cells can sense spatial differences in concentrations as low as 2-10% from one side of the cell to the other (down to cell widths of 10-20 μm).[147] The noise in the fluorescence measurements makes it difficult to ascertain gradients on the length scales of cell widths, but the use of low noise cameras could lead to new and more precise understanding of migrational responses to slight differences in gradient and concentration. Also, little is known about the affect of background concentration on migrational responses, although some have begun to investigate it.[187]

One possible way to approximate the gradients and estimate errors (similar to Fig. 5-7) is to fit the concentration plots with polynomials, and then find the gradient at each location. The standard deviation in gradient could be estimate in that manner, and it could be compared to the magnitude of the gradient at the location. If the standard deviation large enough to cast uncertainty about whether there would be a cellular

response, it should be noted. Although, the sensitivities of different types of cells should not be assumed to be the same.

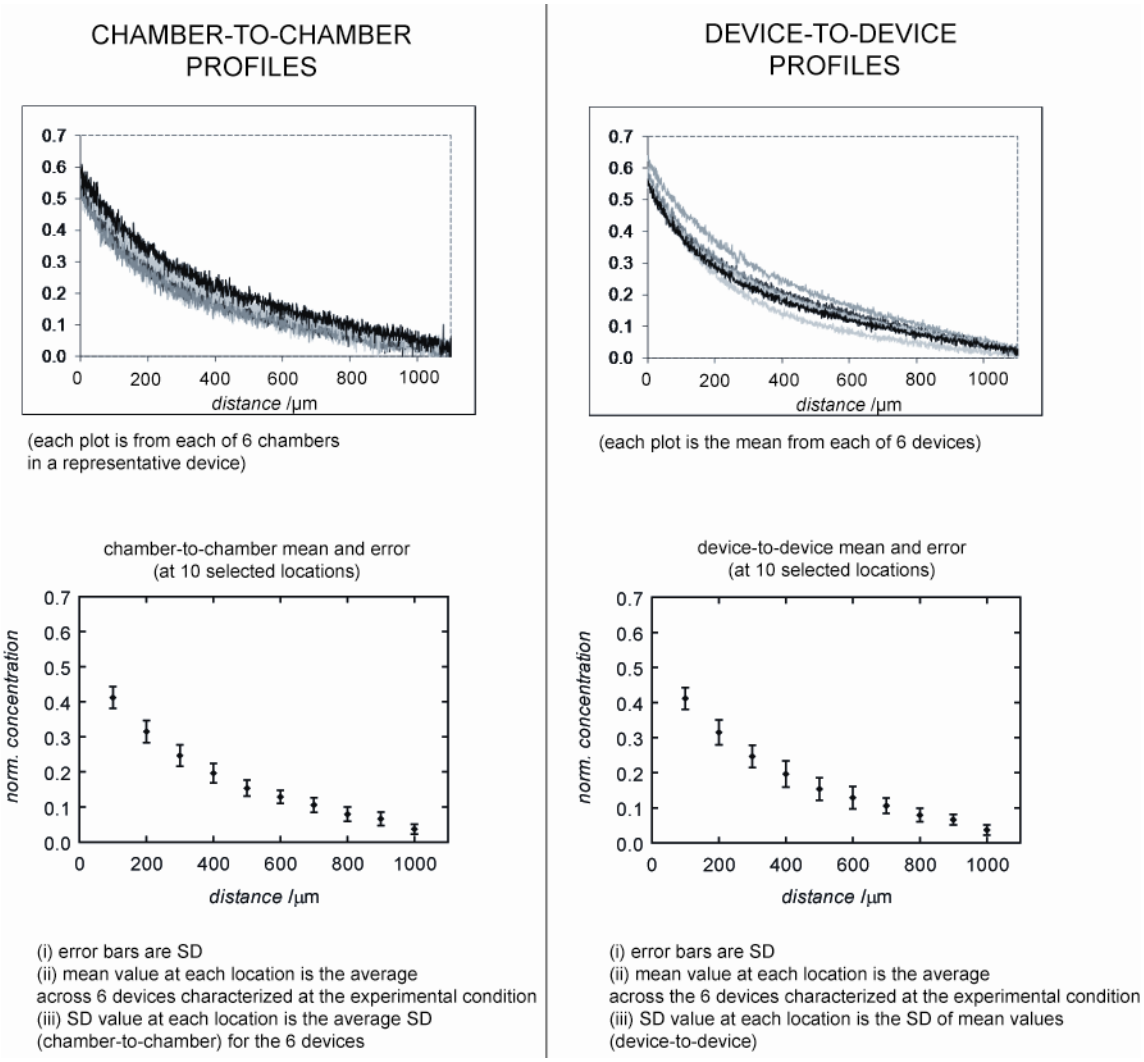

Fig. 5-7 Variation in concentration profiles, chamber-to-chamber and device-to-device. Full plots are shown in the top row. Bottom row shows mean and SD at selected locations. Profiles are measured at steady-state using experimental conditions: flow rate of 2.5 μL min^{-1} and unequal pulsing schedule (see Fig. 5-5(b), lower row). Normalized concentration does not reach 1 because the plots (and experimental region of interest) do not span the full length the chamber in the x-direction.

Testing of Device via Cell Migration Experiments

To test whether the device can be used as a chemotaxis platform, cells are loaded into the device and their response to FBS gradients is measured. Specifically, human

breast cancer cells (MDA-MB-231, epithelial origin) are plated in the array of 6 chambers, and the migrational and morphological responses of single cells in each chamber are quantified before and after a FBS gradient is applied. To quantify the responses, time-lapse phase contrast photos are acquired, and the cells in each frame are segmented. The segment locations and morphological information are used to calculate responses. The particular responses include chemotactic index (CI), speed, area, and circularity.

Cellular response is first considered with respect to CI across the entire region of interest (ROI). The CI of each cell is calculated based upon its first and last x-locations, as well as its accumulated distance, for controls and experimental trials. Additionally, spatially specific information is obtained by dividing the chamber into 4 sections along the x-dimension, and responses are binned based upon the location in the chamber they are observed. The reason for binning the chamber into sections is to acknowledge that the concentration profile within the chamber (when the gradient is applied) is not truly a single condition. Instead, the concentration profile is a collection of different conditions based upon the gradient and background concentration at each location within the chamber. In this case of an exponentially-shaped profile, each incremental movement toward the source increases both the background concentration and the gradient. Ideally, an experimentalist would divide the chamber into an infinite number of sections so as to obtain data for cell behavior at every infinitesimally different condition. However, this is not practical, since there will not be enough cells (and corresponding tracks) at each condition to produce results with meaningful statistical information. Therefore, the number of sections is limited by the number of cells (data). Dividing the chamber into sections and binning the data accordingly is a way to effectively increase the number of experiments/conditions in a single trial, which could increase research productivity and shed light on differential responses among sections. Further details are found in the Methods and Materials section of this chapter.

MDA-MB-231 cells are chosen as the model cell line because they are shown to migrate in response to various signals, including growth factors, cytokines, and general sera.[193,194] Being of epithelial origin, a suspected mechanism for metastasis for the cells is to undergo epithelial-to-mesenchymal transition (EMT), migrate through low flow interstitial spaces of the stroma, and ultimately intravasate into blood vessels.[29] Therefore, from the shear perspective, the device of this work is likely more appropriate as an interstitial (low flow) model when compared with flow-based gradient devices that produce significant shear stresses.

The chemoattractant used in these test experiments is fetal bovine serum (FBS). FBS is commonly used as a chemoattractant, either as a control against which to compare the responses to a defined medium or to model a biological context in its own right. Therefore, testing to see if a serum gradient elicits a chemotactic response from cells is critical to validate that the device works as designed.

The test experiments create a curved, exponentially-shaped concentration profile of serum. The profile presents two general contexts: (i) shallower gradients with low basal concentration on the right side of the chamber and (ii) a steeper gradients with high basal concentration on the left side (serum side) (Fig 5-9(a)). In doing so, the ability of the device to produce curved concentration profiles with near zero basal concentrations is utilized.

Observations

Figure 5-8 shows CI considering the entire region of interest (ROI) for controls and experimental trials. Stages 1 and 2 differ depending on the trial. For the positive control, stage 1 is without FBS and stage 2 is with a uniform profile of FBS. For the negative controls, both stages 1 and 2 are without FBS. For the experimental trials, stage 1 is without FBS, while stage 2 is with a FBS gradient (as shown in Fig. 5-9(a)) with peak concentration on the left.

The positive control trial shows a slight increase in CI from stage 1 to 2, although there are no statistics (based on independent trials) to estimate its error. Two independent trials are performed for the negative controls, and three trials are performed as experiments. Further trials could determine whether test comparisons achieve significance compared to in-trial controls, as well as negative and positive stage 2 controls.

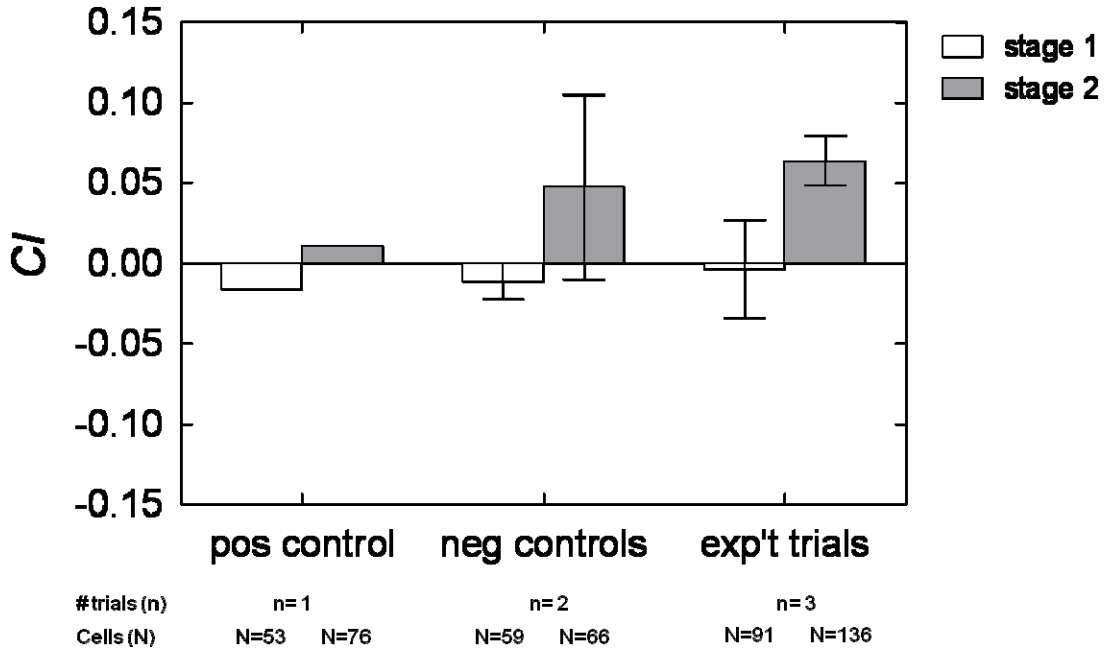

Fig. 5-8 Chemotactic index (CI) for positive controls, negative controls, and experimental trials. Stage 1 for all three categories is with no FBS. Stage 2 for the positive control is a uniform FBS concentration profile (10% v/v). Stage 2 for negative controls is with no FBS. Stage 2 for the experimental trials is a FBS gradient (5% v/v peak concentration on the left side of the ROI), as shown in Fig. 5-9(a).

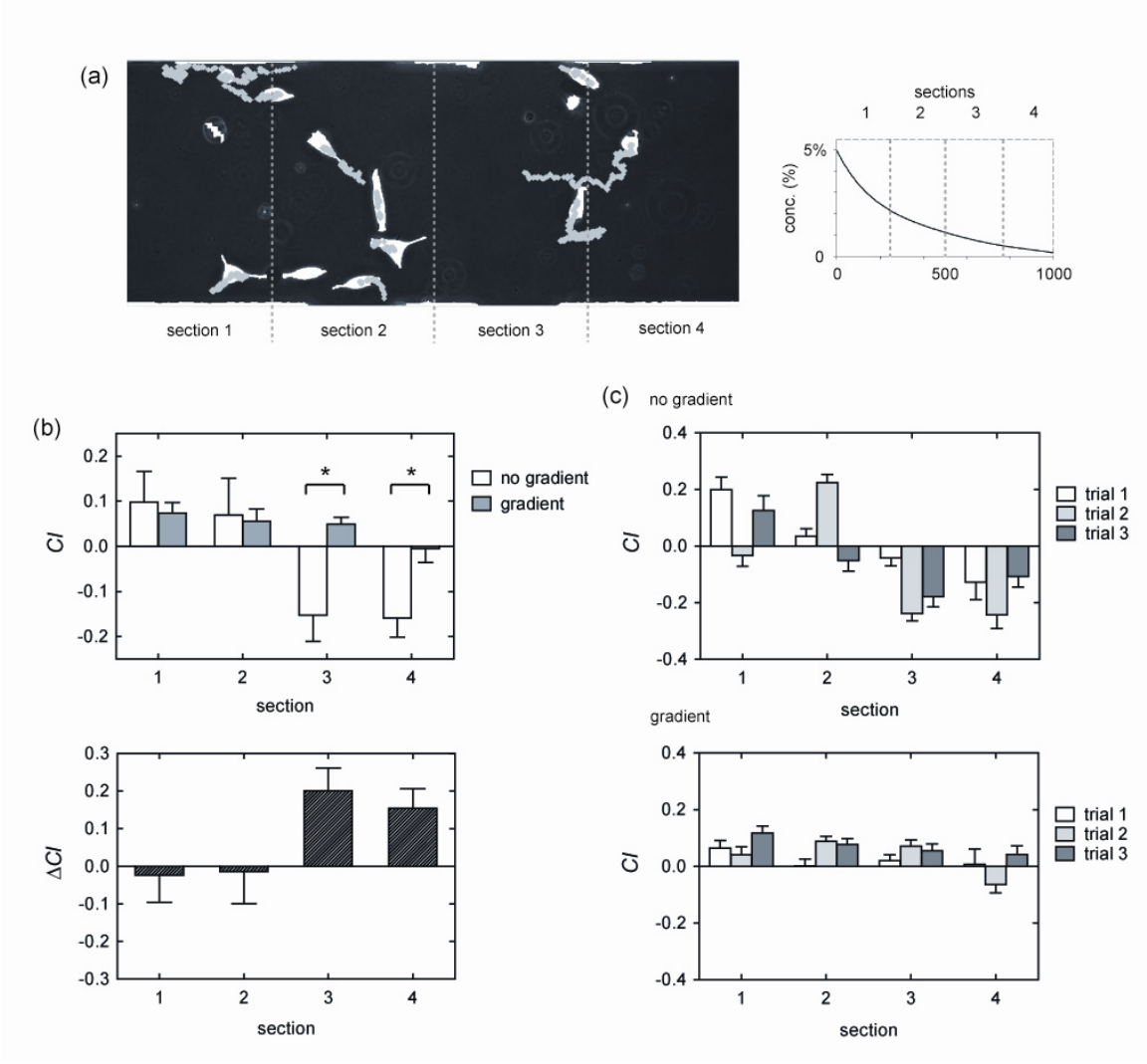

Fig. 5-9 CI from cell migration experiments by section. (a) The chamber region of interest (ROI) is divided into 4 equal sections to spatially bin data. Representative segmented images show cells colored white and migration tracks in gray. Concentration profile of FBS is plotted as a polynomial fit (for clarity) of the steady-state profile generated by 2.5 μL min^{-1} flow rate and unequal flow pulsing schedule (see Fig. 5-5(b), right gradient plot). (b) CI measurements by section at both experimental conditions; change between conditions is plotted below. (c) CI measurements by trial (3 trials performed) to show inter-trial variability. Data gathered from 148 cells across the 3 trials. Error bars are SEM. Stars indicate statistical significance between conditions ($p < 0.05$). Scale: Image in (a) spans 1000 μm in x-direction.

Figure 5-9(a) shows a representative ROI and the 4 spatial sections into which data are binned; cell are segmented in white and migrational tracks are in gray. The concentration profile of serum (shown with sections delineated) reaches a maximum of 5% FBS. CI by spatial section is aggregated and plotted, showing statistically significant changes in CI in sections 3 and 4 after the gradient is applied. To gauge experiment-to-

experiment variability, data are graphed by trial for comparison. Variation among trials is noticeable; however, the results for each trial are consistent in trend.

Data are also plotted in time. These data are contained in Appendix H.

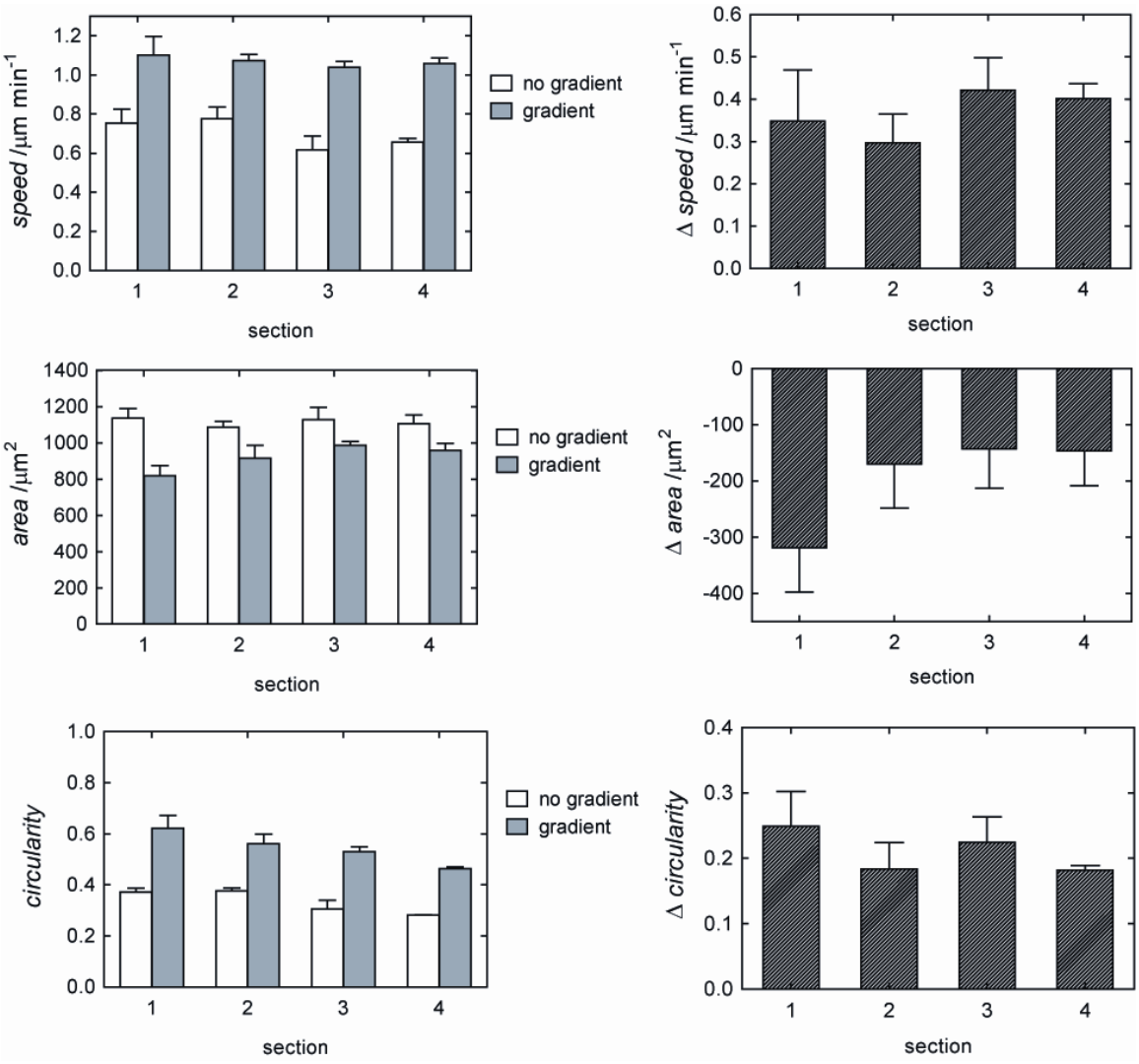

Fig. 5-10 Speed, area, and circularity from cell migration experiments by section. Results are shown by spatial section (1-4) for both experimental conditions. Change of means is shown in percent. Experimental conditions the same as described in Fig. 5-8. Error bars are SEM.

Speed, area, and circularity for both non-gradient and gradient conditions are reported by spatial section in Fig. 5-10. In general, speed and circularity increase upon gradient stimulation, while area decreases. In the gradient condition, both area and

circularity show a slight trend in spatial section, where the area increases from left to right, while circularity decreases in the same direction. As area decreases, circularity appears to increase.

Discussion

A critical response in chemotaxis experiments is the chemotactic index (CI), since it captures both the direction and magnitude of a cells migrational trajectory relative to the gradient. Positive CI indicates net movement toward the chemoattractant source, while a negative CI indicates movement away.

The results of these experiments are very preliminary, as seen in Fig. 5-8 (entire ROI). Only two independent trials were performed for the negative controls, and one of them showed substantially higher CI in stage 2 than any other trial (first and second negative control stage 2 CIs are -0.010 and 0.105), which brings about the wide SEM. The second negative control CI is also greater than all the experimental trial stage 2 CIs (0.040, 0.093, and 0.058). By performing more negative controls, it could be determined if the second control is an outlier and therefore whether the stage 2 CI for negative controls is anomalously high in these results. The experimental trials also require more trials to determine whether there is a statistically significant difference between stage 1 and stage 2 of the experimental trials, as well as between stage 2 of the negative/positive controls and stage 2 of the experimental trials. Overall, Fig. 5-8 indicates that trial numbers should be increased to ascertain any meaningful statistics.

One way to detect possible drivers of the overall results and to detect possible anomalous behavior is to divide the ROI into sections. For instance, after dividing the ROI into four equal sections, results in Fig. 5-9(b) show a statistically significant (in-trial) positive CI change in sections 3 and 4 when the serum gradient is applied. In particular, it appears that cells in section 3 change direction the gradient is applied and migrate, on average, up the gradient toward the FBS source. In addition, cells in section

4 appear to change from a net rightward migration (negative CI) to a CI of zero. One should bear in mind, these are preliminary results and the analysis is shown as an example. For a full analysis, more trials would have to be performed, especially since there are fewer cells to consider (compared to the full ROI), and test comparisons must be performed not only with the in-trial controls, but also with the positive and negative controls.

Regarding the controls, negative control trials (no FBS gradient throughout the whole trial) are performed in order to determine whether stage 1 of gradient trials (first 6 hrs without gradient) are appropriate as intra-trial negative controls, as well as to determine whether measured cell behavior in stage 2 of gradient trials (12 hrs with the gradient applied) could be different from stage 1 simply due to the passage of time (not due to the FBS gradient). Results of negative controls are shown in Fig. G-1 (Appendix G), and both stages of the negative controls are compared to stage 1 of gradient trials and to each other. No statistically significant differences are observed; however, further negative controls should be performed to build statistics, given the low N. A positive control (uniform FBS profile) is also performed. Certain measurements of the positive control appear to be different from those of stage 2 of gradient trials (with gradient), which is what one would expect; however, nothing can be inferred, since there are no statistics associated with the control measurements (N=1 for positive control).

As an aside, there appears to be a directional bias in the migration of cells before the gradient is applied. CI values indicate that cells in sections 1 and 2 tend to migrate to the left (positive CI), while cells in sections 3 and 4 tend to migrate to the right (negative CI) (see Fig. 5-9(b), no gradient conditions). Such behavior may stem from the cells' random-walk-like movement without a directional stimulus (i.e. gradient). Without directional stimulus, cells move and disperse in a manner similar to molecular diffusion, characterized by a random motility coefficient, μ, which is analogous to a molecular diffusion coefficient.[195] Cells are loaded through the middle of the chamber, and

therefore, the cell population is concentrated in sections 2 and 3 (middle two sections) when experiments begin. Tracking data suggest that cells disperse away from the middle of the chamber to the left and right during the non-gradient condition, which is consistent with the hypothesis of random-walk-like dispersion. When the gradient is applied, the responses from sections 3 and 4 suggest that the directional bias away from the serum source may be reduced (and even shifted toward the serum source for cells in section 3).

The CI response from sections 1 and 2 is difficult to interpret; however, possible phenomena can be put forth. When no gradient is applied, the results suggest a positive CI due to random dispersion from the middle of the chamber. When the gradient is applied, cells continue to show positive CI, but the mechanism is not clear. The cells could be continuing in their dispersive movement. Another possibility is that cells sense the gradient, but the level of background concentration causes the cells' morphology (area and circularity) to change, as shown in Fig. 5-10, in a manner that affects chemotaxis. The reduction in area and rise in circularity suggest a contractile morphology indicative of cells that have partially detached from the substratum, which would suggest that cell-substratum adhesion is reduced or intracellular tension is increased. Cell speed is greatest at intermediate levels of cell-substratum adhesiveness;[195] therefore, a reduction of adhesion could interfere with efficient chemotaxis, resulting in the slightly lower CI for sections 1 and 2 during gradient stimulation. One possible way to test for this is to perform the same experiment, but coat the substrate with a much higher concentration of fibronectin than that which is used in the experiments shown (8 $\mu m\ mL^{-1}$). The presumption is that the increased Fn concentration increases the adhesion for cells nearest to the source, enabling them to chemotax more efficiently. Another, more simple experiment is to reduce the source concentration so that the gradient is inherently shallower on the left side of the chamber.

Time course plots demonstrate the utility of monitoring of cellular response during transient conditions. Most notably, area and circularity measurements suggest that

cellular response is most dramatic after 3 hours. The rise time shown in Fig. 5-5 at the experimental condition is roughly 100 min for 70 kDa dextran, which is slightly less than the cellular response time. However, FBS is a complex medium containing smaller and faster diffusing growth factors that could be contributing to cellular response (e.g. EGF 6 kDa). In this case, the rise times could be less than half that of the dextran. Experiments with a defined medium could more precisely shed light on the timing of cellular responses with respect to rise time. If a faster rise time is ultimately required, the characterization shown in Fig. 5-5 suggests that increasing the flow rate could reduce the rise time significantly. Of course, this comes with the trade-off that more reagent/sample would be used at a higher flow rate, and some reagents are very rare and/or expensive, which would limit the number of experiments or prohibit them completely.

Chapter Summary

This chapter details the development of a prototype microfluidic chamber array that generates soluble concentration gradients. The device is designed to generate gradients with a novel combination of features: fully stable, low shear, switchable on-off, capable of low basal concentrations, and adjustable profile curvatures. In addition, the chamber array is scalable, and it is fabricated in a single material (PDMS) and a single alignment step, which increases the potential for future high-throughput screening and manufacturability. This diverse combination of features is made possible by sequentially pulsed delivery and 3-D flow networks.

Device design includes numerical simulations of both the velocity field (to ascertain shear stresses) and diffusion-only mass transport. Gradient characterization via fluorescence measurements yields information regarding gradient formation (concentration profiles at numerous time points after the gradient is turned on), rise times, and steady-state profiles. Characterization data are also used to compare with the diffusion-only model, showing that mass transport is likely driven by both diffusive and

convective components at a high flow rate (2.5 μL min^{-1}), while it is diffusion-dominated at a lower flow rate (0.25 μL min^{-1}). In addition, fluorescence data are used to measure chamber-to-chamber and device-to-device variation among concentration profiles.

Finally, human breast cancer cells are introduced into the array, and certain morphological and migrational responses to a FBS gradient are observed. Cell experiments are performed to test whether the array and the gradients it produces could elicit responses from cells so as to prove the concept of its use as a migration screening tool. Preliminary experiments show high variability chemotactic index (CI) in experimental trials and controls that precludes any conclusion with respect to chemotactic response. A major source of uncertainty stems from the low number of trials. If more trials are performed, statistical significance may emerge. Although statistical significance is not achieved when considering the full chamber, the p-value for in-trial non-gradient controls compared to the gradient condition is somewhat low (~0.1). By partitioning chamber into sections, one can begin to understand what spatial regions may be driving such a result. For example, certain sections of the chamber (3 and 4) show statistically significant differences in CI when comparing non-gradient controls with the gradient condition; however, it must be emphasized that further trials are required to increase the power of statistical measures and to confirm whether the responses are due to the gradient or other phenomena. For instance, cell migration could be affected by competing autocrine and paracrine signal gradients, as well as matrix remodeling in the tracks through which cells translocate. Additionally, if it is hypothesized that the cells respond best to the shallow gradients and low basal concentrations (sections 3 and 4), trials could be performed where the input concentration of FBS is lowered, producing a shallow gradient (and low basal concentration) condition in different sections (1 and 2). Also, other cell types could be tested against gradients of known chemoattractants, as their responses may be more obvious than those from the trials already performed; the breast cancer line (MDA-MB-231) used in this work may only respond with small

changes to its net directional bias, making analysis more difficult than required for proof-of-concept purposes. Moreover, the hypothesis that cells disperse via random-walk due to a concentrated loading distribution (in the middle of the chambers) should be tested by modifying the design of the array so as to load cells uniformly and observing their movement in the absence of a gradient. The above proposed experiments are a few of many that should be performed to further optimize the device and provide clearer explanations of how the array performs as a cell migration screening tool.

It should be noted that all gradient-generating microfluidic devices face similar challenges with respect to their ability to be translated into mainstream biological research. With respect to microenvironment, flow-based devices have become the most commonly-used gradient-generating microfluidic platform.[103,170-174,187] This has happened despite evidence that shear induced responses could confound results, both in terms of migrational bias[184] and metabolism.[196] Also, flow-based gradient devices inherently remove any autocrine or paracrine signals that are secreted by the cells being studied (due to the direct flow over the cells), which could further confound results (although, such a characteristic could also act as an experimental condition[118]). Furthermore, as previously mentioned, the device-to-device variation in gradients is unstudied (or unreported) in microfluidics literature. In all such literature, the concentration profile from only a single device is reported. This work attempts to address the lack of variation information by measuring variation across a batch of 6 devices, and it is shown that notable variation exists. If variation in such a well-controlled system (i.e. computer-timed valve actuation sequences) with a well-accepted and repeatable fabrication process (i.e. photolithographically manufactured molds) exists, then it is reasonable to expect that similar or greater variation could exist in other microfluidic systems. If so, then experimental results based upon such systems could be called into question without the support of proper controls and assisting agents, such as a fluorescent marker to monitor the gradient (so long as the marker does not interfere with

experiment itself). However, these challenges should not deter researchers from further developing microfluidic gradient-generating systems. The potential for stable and highly-controllable gradients, array scalability, and low sample usage offered by microfluidics is likely to exceed the performance of conventional methods, such as transwell, Dunn, and under-agarose assays. Such conventional methods are inherently unable to maintain stable gradients, and perturbations (mechanical or thermal) could disrupt or destroy gradients that are generated. Fertile ground exists for advancement in microfluidic gradient-generators, so long as it is approached with a systematic, engineering viewpoint of thorough characterization and design for reproducibility.

Table 5-2 Chapter summary.

advances / contributions
1. device: a novel and large set of features combined into an chamber array platform, enabled by sequentially pulsed delivery and 3-D flow network *
(a) soluble gradients
(i) fully stable
(ii) low shear
(iii) switchable on-off
(iv) capable of low (near zero) basal concentrations
(v) adjustable in curvature (within linear to concave limits); no device redesign required
(b) array
(i) scalable to larger arrays (due to 3-D flow network)
(ii) single material (PDMS)
(iii) single alignment step during fabrication (due to modified compression-molding)
(c) simultaneously addresses many limitations of both flow-based and free-diffusion-based gradient devices
challenges / limitations
1. device:
(a) gradient rise times are not instantaneous; they are dependent upon signal size and flow rate
(b) concave curvature and faster rise times of gradients requires high flow rates; may limit or prohibit experiments with precious or rare reagents
(c) array is small (6 chambers); larger arrays are required for viability as a screening tool
(d) more gradient characterization required
(i) trials to determine device-to-device variation of other gradient devices for benchmarking comparison
(ii) trials to scan the flow rate vs. pulsing schedule space to determine the effect on profile shapes and rise times
2. data from trials in this work (although showing statistically significant differences in readouts in certain sections) are insufficient to confirm directed migration in response to a signal gradient
(a) more control trials (negative and positive) are required
(b) different cell types and known chemoattractants should be tested (may prove to be better models for proof-of-concept than the current cell line and FBS)
(c) reponses to different gradient conditions (gradients, shapes, and background concentrations) should be tested in the array (only one condition has been tested so far)

* Manuscript of this work in preparation for publication.

CHAPTER 6

CONCLUSIONS

This work is intended to advance the state-of-the-art in microfluidic cell-based assays. An underlying theme of the research is the creation of 3-D flow networks in order to realize chamber arrays that can ultimately be scaled to larger, higher-throughput arrays. The main objectives of this research are to develop a fabrication method for 3-D flows, and also to test two particular microfluidic assay platforms that generate microenvironments with unique characteristics to address complex biological phenomena.

Fabrication of 3-D Flow Networks

A fabrication method is developed to realize 3-D flow networks (vertical connectivity between flow layers) based upon focused compression and alignment with partial curing. It is referred to as a modified compression-molding process. Progress in device technology is often made possible by improvements in fabrication, and in this case, the modified compression-molding process improves final device yield to almost 50%. Such a yield, while low by most industrial standards, enables the design and testing of chamber arrays for specific cell-based assays in an academic setting.

With respect to the microfluidics field in general, the learning in this work underscores the need for more systematic attention to fabrication process development in future publications/literature. It appears that most microfluidics fabrication knowledge is either significantly under-explored or under-reported. A prime example of under-reporting is the treatment of the original compression-molding process upon which this work's fabrication process (modified compression-molding) is based. A diagram of the compression stack is found in the original publication; however, there are no detailed

comments regarding the process flow, yields, and failure modes.[87] It is possible that the idea of using focused pressure during compression, which is described in this work and published,[95] is fabrication knowledge that is already known to the original inventors of the compression process, but simply not made public (either deliberately or by lack of appreciation of its worth). Another example is the protrusion method of fabricating through-holes. Although the possible effect of PDMS surface tension (wetting and profile curvature) is mentioned in a single sentence in the original publication,[84] there are no specific parameters (e.g. feature widths or PDMS thickness ranges) mentioned that could cause device failure, nor is there a description of the frequency or severity of such failures. The lack of fabrication details in microfluidics literature comes with a heavy price to advance the field, where significant time and effort are spent by research groups (like this one) debugging and "re-inventing" processes that could already be well-understood by others.

When it comes to fabrication, much of the focus in microfluidics, particularly for PDMS-based devices, is the simplicity of rapid prototyping granted by soft lithographic methods. Perhaps the idea of simplicity is over-emphasized because microfluidics is still a young field of study, between 10 and 20 years old, and those who work in the field are prone to emphasize its benefits (and minimize its challenges) in order to build interest in the work. This work is no exception. However, this work acknowledges that in order to create more capable devices (including those with 3-D flows and very unique sets of features), fabrication complexity will grow accordingly. Therefore, certain learning is detailed, such as the method to reduce gas bubble nucleation during compression, use of support posts to maintain PDMS surface planarity, yield benefits of thermal bonding, and overall estimates of device yields for the developed fabrication process. In doing so, the fabrication process is elevated to the same level of importance as design, and it is hoped that similar emphasis will be adopted in future works in the field.

A key benefit of 3-D flow networks is the ability to scale to large arrays efficiently (with respect to required device footprint and input/output ports). In addition, 3-D flow networks could facilitate more convenient addressing of individual chambers. The motivation to address individual chambers with different combinations stems from the desire to achieve the same level of versatility as conventional well plates. However, microfluidic chamber array technologies face many hurdles in that goal. Ultimately, the goal of microfluidic chamber arrays should not be to replace well plates, but instead to provide an effective alternative, particularly to prevent evaporation, perform complex fluid handling, reduce sample usage, and provide unique capabilities (e.g. fully stable concentration gradients).

Simple, reliable, and reproducible means of fabricating through-holes and 3-D flow networks will bring about greater efficiency in microfluidic device layout and operation, and perhaps more importantly, it could open the design space so as to bring about creative technological advances and applications yet to be conceived. The key advances, learning, and limitations regarding 3-D flow networks in this work are reviewed in the Chapter Summary in Chapter 3 (Table 3-3).

Microfluidic Chamber Array for Soluble-Matrix Signaling Studies

A microfluidic chamber array is designed, built, and tested that can present cells with different signaling combinations of both soluble and matrix factors. To provide a unique set of capabilities desirable to life scientists, the array operates with continuous perfusion, prevents cross-chamber contamination, protects cells from excessive shear, and offers considerable experimental versatility. These attributes are made possible by implementing a 3-D flow network, which is fabricated using the modified compression-molding technique described in Chapter 3.

The array is tested as a screening tool for studying phenotype transitions and cellular behavior by observing the responses of alveolar epithelial cells under

combinatorial soluble and matrix conditions. Given that cellular response mechanisms are complex, this array technology is ideal to perform studies where cellular response is sensitive to microenvironmental conditions within a parallelized, well-controlled, scalable microfluidic format. Furthermore, the array could be used to perform studies under different perfusion rates (in combination with soluble and matrix signals) or adapted to stimulate cells with time-varying signal patterns.

The array must be further tested with different cell-signal models, scaled-up, and automated to a greater extent. Such a setup will lead to higher control and throughput, making the array capable of larger-scale studies. These studies could lead to insights into the mechanisms for the onset and progression of pathological phenotypes and the identification of novel therapeutic targets to treat diseases. A challenge to successfully deploying such systems is likely to be at the interface between the device and the macro-scale world. While manually inserting pins and tubes into devices is acceptable in academic settings, industrial applications will require automation in this respect. Major advances and limitations of this work are reviewed in Table 4-1 (Chapter 4 summary).

Soluble Gradients via Sequentially-Pulsed Delivery in a Chamber Array

A novel microfluidic chamber array that generates soluble signal gradients is introduced based upon a technology referred to as sequentially pulsed delivery. Similar to the soluble-matrix chamber array, the sequentially pulsed delivery array is enabled by a 3-D flow network. As a result, a rich set of microenvironmental features is integrated into the array, which includes: (i) fully stable signal gradients, (ii) very low shear stresses, (iii) gradient profiles able to approach zero concentration, (iv) gradients that can be switched on-off, and (v) gradient profiles whose curvature are changeable (without changing inlet concentrations or upstream flow architecture). These microenvironmental features offer wide-ranging flexibility in the spatial and temporal control of gradients. In addition, the following system-wide features are exhibited: (i) similar gradients in all

chambers, (ii) a network architecture enabling scale-out of in-line or 2-dimensional chamber arrays, and (iii) a fabrication process requiring only a single alignment step. The system-wide features are intended to facilitate greater throughput and manufacturability.

The system is tested as a chemotaxis assay by measuring the response of human breast cancer cells to gradients of FBS. Migrational and morphological readouts are rapidly quantified on frame-by-frame and single cell bases. Cellular responses are stratified along spatial and temporal dimensions. Some statistically significant responses are measured, but more experimentation is required to confirm that the gradient caused directed migration.

The abovementioned studies serve to highlight numerous features of the system and begin testing it as a versatile, high-throughput, and high-content assay platform, which could bring about significant contributions to our understanding of cellular behaviors and their underlying biomolecular mechanisms in response to spatially and temporally changing gradients. Before such work can be performed, more validation of the array with different cell types and microenvironmental contexts is necessary (using different chemoattractants and matrix substrata). This way, incompatibilities with the design can be identified and addressed. Improved and expanded versions of this array technology could be directly applied to studies in cancer, development, tissue regeneration/repair, and immunology, as well as serve as a tool to screen potential therapeutic compounds to treat related diseases in a massively parallel fashion. Major advances and limitations of this work are reviewed in the Chapter Summary of Chapter 5.

Future Potential for Technology in This Work – Possible Applications in Cancer

The experiments performed in this work for both arrays are intended as initial proof-of-concept trials to test for proper device operation. Once designs and protocols are optimized, future work could focus on adapting and scaling-out the devices for rapid

screening of cancer cell response to various growth factor-matrix stimuli to determine what conditions maintain, exacerbate or reverse their phenotypes, as well as screening potential drugs against the cells to identify and understand differential efficacy based upon the signaling conditions. This could provide clinicians with insights as to when and where an anti-cancer drug will have the greatest effect on cancer cells.

Similar applications exist to rapidly screen potential drugs against cells within gradient microenvironments. There is great need for rapid, high-content screening in the context of cell migration, since few platforms provide stable, reproducible gradients in a high-throughput array format. The great need stems from the knowledge that migrating cancer cells are known to be resistant to apoptosis, and they are also the most lethal (being prone to metastasize). Screening migratory cancer cells against various combinations of drug-chemoattractant-matrix combinations could yield new insights in how to specifically tailor drugs to arrest the migration of metastasizing cells, perhaps making them more vulnerable to standard anti-cancer drugs. Such findings could lead to new and highly effective combination therapy approaches to treat metastatic cancer.

Challenges and Future Directions for Microfluidic Systems

This work focuses on microfluidic chamber arrays that are enhanced by 3-D flow networks. However, much of the learning from this work is applicable to the microfluidics field in general. In the author's opinion, the greatest challenge to the advancement of microfluidics (for life science use) continues to be its degree of acceptance by biologists. It is likely that biologists are afraid to attempt microfluidic experimentation because they fear that (i) the results would not be comparable to those of flasks and well plates, therefore raising more questions than answers, and (ii) it is not simple, easy, or cost-effective enough to try. Such concerns are raised in this research. With respect to lack of comparability, experiments in Chapter 4 showed that new assay protocols may be required to properly stain cells in a microfluidic system (as opposed to

in a standard well plate). In addition, the random-walk dispersion observed in the gradient device (Chapter 5) may indicate a device specific response that makes its results difficult to compare with other literature. That being said, researchers must be careful not to assume that flask/well plate behavior is always the "normal" mode; the results in a microfluidic device could be highlighting behavior that differs from flasks but is closer to true physiological or pathological behavior.

From the standpoint of simplicity and cost, the greatest challenge for a lay biologist, aside from building the devices themselves, is the lack of standardized and easy-to-use world-to-chip interconnect technologies. The vast majority of intangible and experience-based knowledge is contained in the act of setting-up a microfluidic experiment, which is predominantly an exercise in attaching and detaching world-to-chip interconnects (tubes and needles) as the device is primed, incubated, and loaded with cells. The learning process and initial failure rates for new users are daunting. Unfortunately, most research in microfluidic systems is devoted to the internal fluidic circuitry of the device (in the search for a "killer application"), not the world-to-chip connections. The use of 3-D flow networks and concomitant efficiencies in scaling could minimize the number of world-to-chip ports; nevertheless, new world-to-chip interconnecting approaches will be required regardless of device circuitry, ideally where a device is inserted into an interconnect fixture or box and the connections are established without manual manipulation.

Moving forward, there are two directions the author would pursue, building upon the learning from this work. First, there is a great opportunity, as just mentioned, to develop new world-to-chip interconnect technologies. Such technologies could focus on new approaches for interfacing devices to connecting fixtures (sealing and pressurizing/priming devices), innovative entry ports (on the connecting fixture) where fluids could be easily introduced, and standardized equipment and programs to automate the process of preparing a microfluidic device for experiments. A challenge in such

interconnects is minimizing dead volumes so that microfluidic systems best realize their potential for low sample usage. Although such a research topic may not be as "fashionable" as working on internal device circuitry, there are opportunities to make an impact, given that the world-to-chip interconnect field is still nascent. It would be wise to advocate for the establishment of an academic-industrial consortium to host workshops and conferences on the topic, thereby building interest in the field and emphasizing the necessity for interconnect standards. In addition, given the practical nature of the work, opportunities for industrial collaborations should be aggressively cultivated for knowledge sharing and funding.

A second research thrust, based directly upon the 3-D flows research of this work, would be to integrate diverse unit operations onto a single device. This is an ongoing aim in microfluidics research because it would reduce the amount of manual operations a worker is required to do. From the world-to-chip interconnect standpoint, functional integration bypasses the need for cells (or other samples) to be introduced and/or extracted from a device via world-to-chip ports. The advancement of 3-D flow networks is crucial for functional integration, as it enables samples to be shuttled from one functional area on the chip to another in an efficient manner. It is recommended that the research start by integrating commonly performed life science functions, such as cell culture, cell selection, lysis, and separations. Although some of such functions have already been integrated in earlier microfludic devices, none have done so using the efficiency, scalability (many of the same unit operations), and packing-density that 3-D flows could offer.

No matter what research is pursued, it is extremely important for microfluidics projects to be pursued in the context of strong collaborations. These collaborations should be both on the fabrication side and the biology side in order to maintain focus and share ideas. It is the hope of the author that this work will move the field of microfluidics closer to widespread adoption and to the establishment of a new and productive industry.

APPENDIX A

LAYOUTS OF MICROFLUIDIC DEVICES

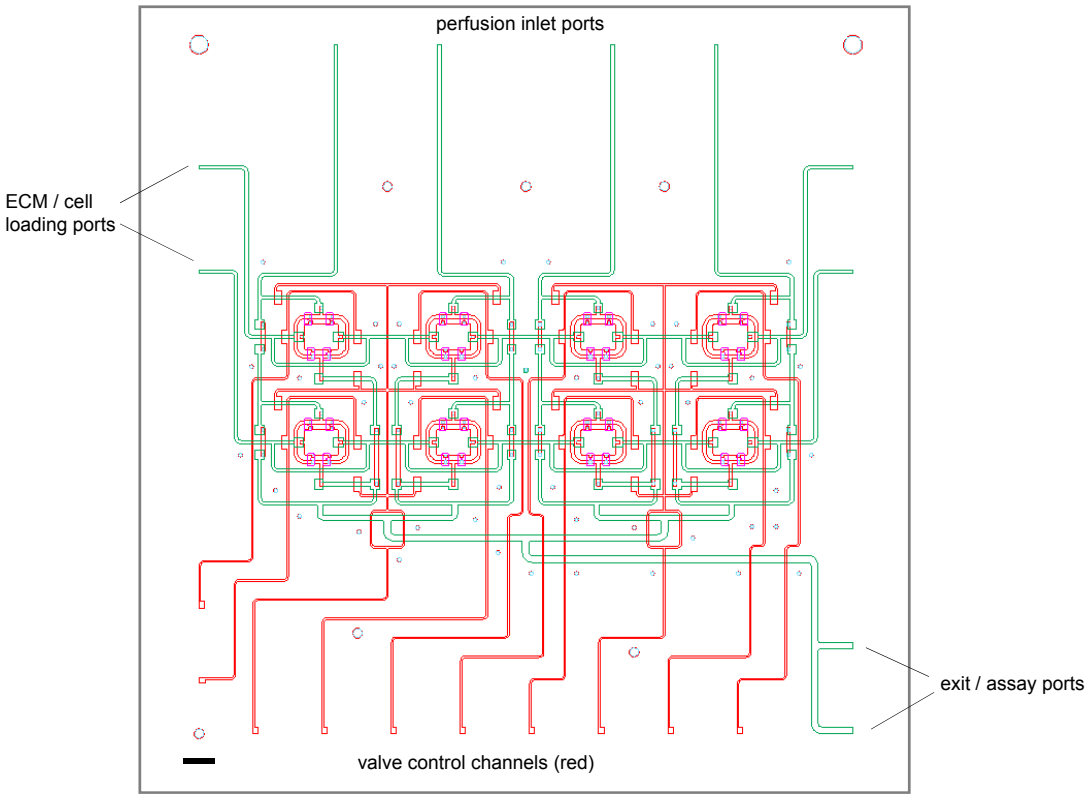

Fig. A-1 CAD layout of chamber array for soluble-matrix signaling. Green (top) layer includes flow channels. Red (lower) layer includes chambers and pressure (control) lines for integrated valves. Purple (top) layer denotes conduits leading into chambers. Light blue features are through-holes (middle layer). Scale bar 1 mm.

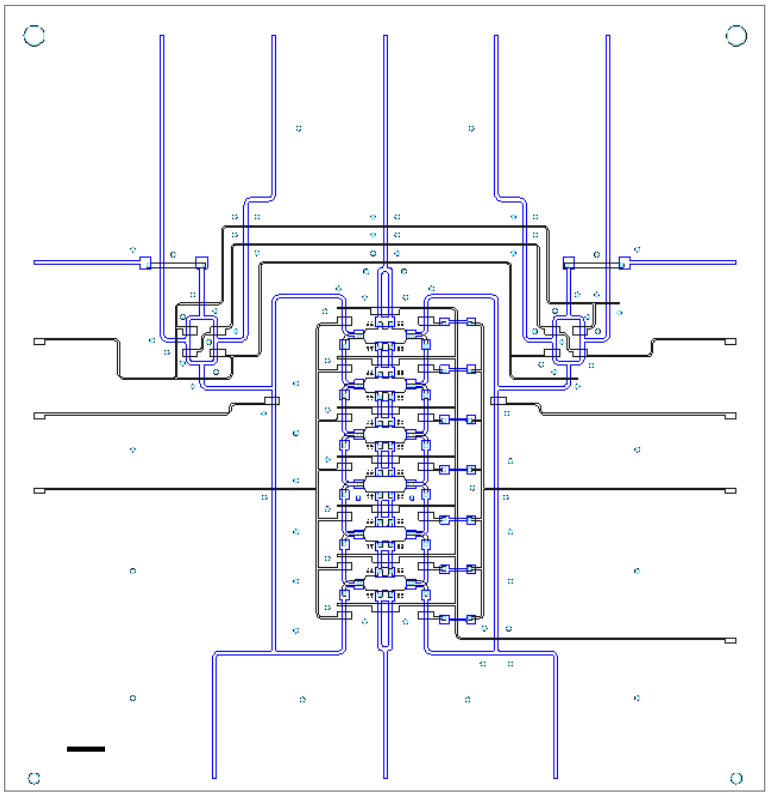

Fig. A-2 CAD layout of chamber array for soluble gradient signaling. Blue (top) layer includes flow channels. Black (lower) layer includes chambers and pressure (control) lines for integrated valves. Light blue features are through-holes (middle layer). Full labeling of features found in Fig. 5-2. Scale bar 1 mm.

APPENDIX B

EXPERIMENTAL SETUP

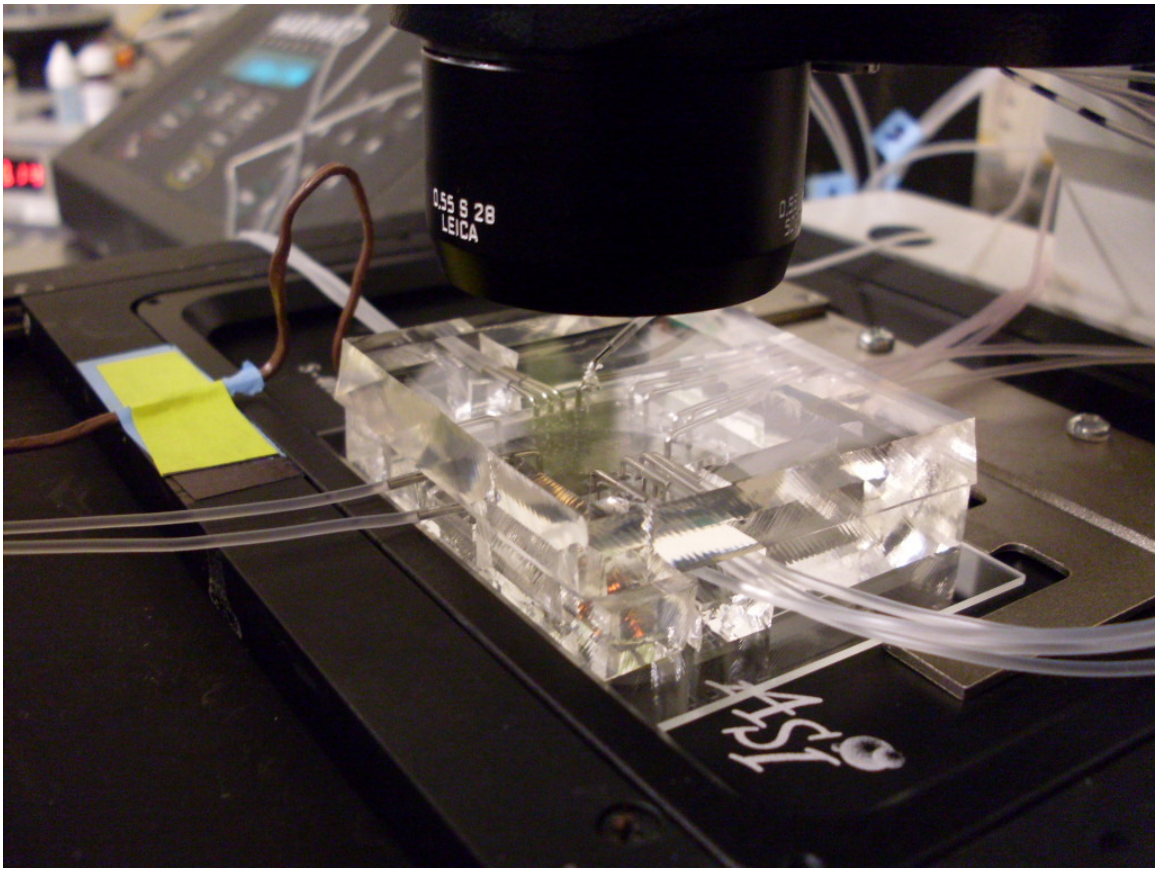

Fig. B-1 Setup for chemotaxis experiments. Device is mounted to motorized x-y stage on inverted microscope. Flow and pressure tubes enter device through stainless steel L-shaped pins. Humidified air is flowed into transparent PDMS enclosure around the device to prevent bubble nucleation in the array. Heating fan (not shown) maintains 37 °C temperature.

APPENDIX C

INTEGRATED, ON-CHIP VALVES

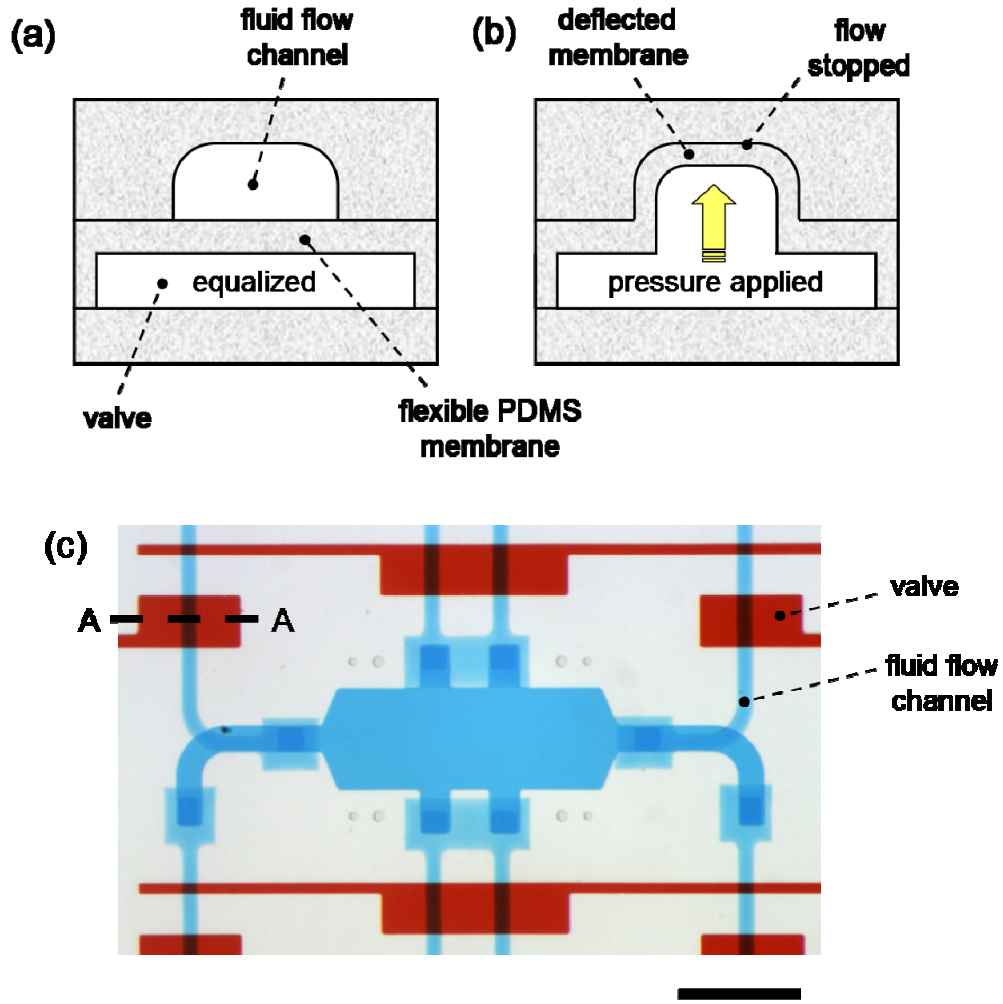

Fig. C-1 Integrated "push-up" PDMS valves. In this work, on-chip valves are actuated by pressurizing valves located in a lower layer. The pressure deflects a flexible PDMS membrane upward so that it stops fluid flow in a channel in the upper layer (subfigure (b)). This type of valve is based on the work of Unger *et al.*[83] Membrane thickness is 30 μm for devices in this work, and pressures required for full closure are 27-30 psig. (c) Valves around a chamber in a soluble gradient-generating device. Cross-section A-A corresponds to the illustrations in (a) and (b). Scale bar is 500 μm.

APPENDIX D

WAFER LEVEL VIEW OF MODIFIED COMPRESSION-MOLDING

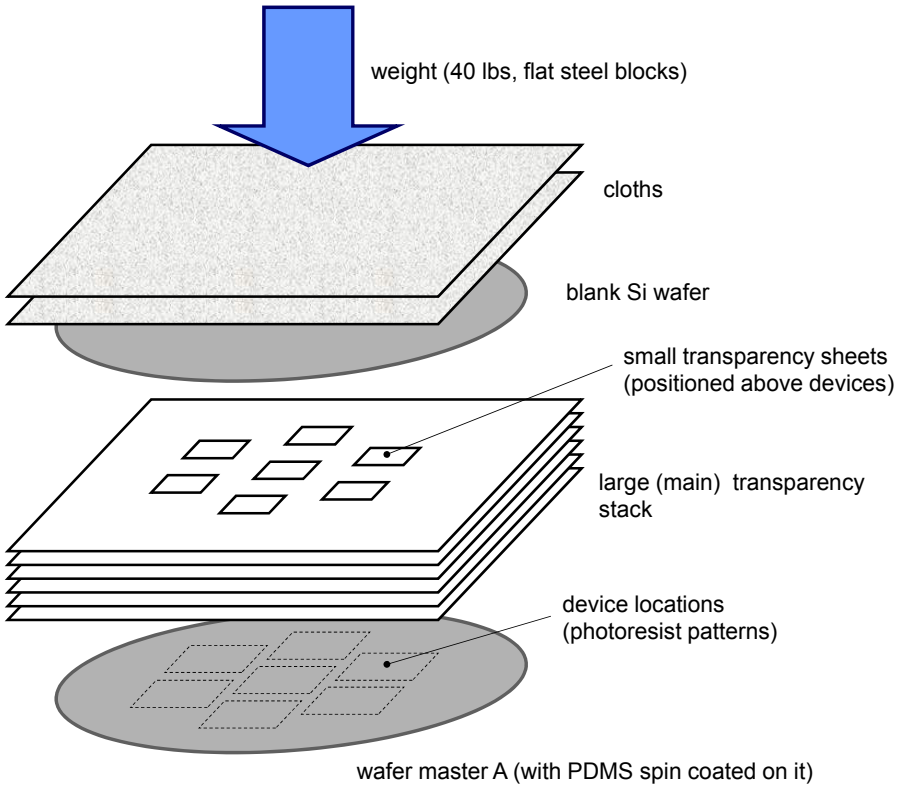

Fig. D-1 Wafer-level view of stack for modified compression-molding fabrication process. Small transparency sheets cut to the size of each device are placed on the main transparency stack. Small sheets are aligned to device locations. The main stack and small sheets are Scotch®-taped together to maintain correct relative positioning. When weight is applied, pressure is focused above each device, and PDMS is laterally displaced from the tops of photoresist features.

APPENDIX E

DETAILED FABRICATION PROCESS

Table E-1 Details for the modified compression-molding process described in Chapter 3.

FRONT-END PROCESSING		
Step #	**Step Name**	**Description**
1	Master A prep.	Master A is a 100 mm polished Si wafer (0.5 mm thick) patterned with 2 layers of SU-8 photoresist. First and second layers correspond to lower and middle layers, respectively, in CAD layouts shown in Appendix A. 1. SU-8 features are 50 μm and 30 μm tall in first and second layers, respectively. Second layer is patterned on first layer, making total thickness 80 μm. Fabrication is performed using standard photolithography processes[90] and recipes from MicroChem Corp. 2. Partially silanize by vapor deposition. a. Place 0.2 mL silane (T2492, United Chemical Technologies, Bristol, PA, USA) in a glass vial. b. Vial and master are placed in a vacuum desiccator, evacuated to ~30 torr. c. Silane deposits (by vapor) on master A for 15 min in desiccator. Do not silanize longer (a master with a full silane layer causes the PDMS to detach from the master (stick to the transparency) during compression-molding process). d. Excess adsorbed silane removed by casting PDMS (10:1 prepolymer:crosslinker ratio) on wafer, curing at 70 °C for 1 hr, and peeling off the master. Note: Silanization performed in fume hood. This process is performed on the master once.
2	Master B prep.	Master B is a 100 mm polished Si wafer patterned with AZ P4620 photoresist. AZ features correspond to top layer in CAD layouts in Appendix A. 1. AZ features are 35 or 25 μm tall (for soluble-matrix or gradient device, resp.) and fabricated using standard photolithography processes[90] and recipes from AZ Electronic Materials. a. Note: Prior to AZ patterning, to improve adhesion of AZ photoresist, hexamethyldisilazane (MicroPrime HP Primer, Shin-Etsu Chemical Co., Tokyo, Japan) is spin coated onto the wafer at 3000 rpm for 30 s, then placed on a hotplate at 110 °C for 45 s to evaporate residuals. 2. Reflow AZ features so that cross-sections change from rectangular to semi-circular cross-sections (assists with complete closing of on-chip valves (Appendix C)). a. Place master on hot plate at room temperature. b. Ramp temperature to 125 °C, then turn off (let ramp down to room temperature) c. Remove master from hot plate when temperature reaches 40 °C. 3. Fully silanize by vapor deposition a. Place 0.2 mL silane in a glass vial. b. Vial and master are placed in a vacuum desiccator; evacuated to ~30 torr. d. Silane deposits (by vapor) on master B for 6+ hr in desiccator. e. Excess adsorbed silane removed by casting PDMS (10:1 prepolymer:crosslinker ratio) on wafer, curing at 70 °C for 1 hr, and peeling off the master within 5 min after removing from

		oven (waiting longer will result in AZ features detaching from master). Note: Silanization performed in fume hood. This process is performed on the master once.
3	Transparency prep.	A silane layer is vapor-deposited on the transparency that is laminated to uncured PDMS on master A. This prevents the PDMS from peeling off the wafer (adhering to the transparency) when the transparency is de-laminated after compression/partial curing. 1. Place 0.2 mL silane in a glass vial. 2. Vial and transparency are placed in a vacuum desiccator, which is evacuated to ~30 torr. 3. Silane deposits (by vapor) on transparency for 30 min. 4. Excess adsorbed silane removed by wiping transparency gently with IPA-soaked cleanroom cloth (Texwipe). Transparency ready for lamination. Notes: These procedures are performed in a fume hood. Transparency can be re-used by wiping away residual PDMS with an IPA-soaked Texwipe (the silanization should then be repeated).
4	PDMS prep.	1. PDMS mix 1: 30 g PDMS prepolymer and 1.5 g crosslinking agent are mixed in a cup. 2. PDMS mix 2: 55 g PDMS prepolymer and 11 g crosslinking agent are mixed in a cup. 3. Both mixtures are degassed under vacuum in a desiccator (~30 torr) for 2 hr.
5	Spin coat PDMS on Master A	1. Master A is placed on a spin coater chuck, and PDMS mix 1 is poured onto the master until it is ¾ the radius of the wafer. PDMS should be poured slowly to avoid bubble trapping. 2. Spread: Spin at 500 rpm (100 rpm/s acceleration) for 15 s. 3. Spin: Spin at 1000 rpm (500 rpm/s accel.) for 31 s. 4. Relax: Let PDMS relax on the master for at least 15 min 5. Remove master A from spin coater and place on a large transparency (acts as a backing for the master and the subsequent stack) on a flat lab table; cover the master with a 150 mm Petri dish cover to prevent dust from settling on the uncured PDMS.
6	Partial cure PDMS slab on Master B	1. Place master B in a 150 mm Petri dish. 2. Pour all PDMS mix 2 onto master B. PDMS should be poured slowly to avoid bubble trapping. PDMS should be ~4 mm thick. 3. Gently press on the master using a razor blade to force any air bubbles out from underneath the master (avoid device features). 4. Place Petri dish with master into an oven at 70 °C; make sure that the dish is level by using a leveler. Petri dish should not be covered. Start timer. 5. Check progress of cure occasionally by touching the PDMS with a plastic pipette. If oven temperature is not uniform, rotate dish to make sure PDMS cures evenly. 6. Once PDMS cures into a solid slab, remove from oven. Should take roughly 15-20 min. PDMS is partially cured. 7. Within 2-5 min of removing from oven, cut around the master and slowly peel PDMS slab off of master. (Delaying over 5 min may cause AZ photoresist to detach from master when peeling the PDMS off.) 8. Store PDMS slab in a Petri dish. PDMS slab contains top layer channels for all 7 die.
7	Laminate transparency on Master A	Laminate the transparency from step 1 onto master A. 1. Fix one side of the transparency with tape. (Tape should contact the larger transparency that acts as a backing for the master.) 2. Carefully (and slowly) laminate transparency from one side to the other side of the master. Do not trap bubbles underneath. Bubbles can be released by pulling-up transparency and re-laminating. A glass or plastic rod with a rounded end can be used to assist in lamination. 3. Tape-down the other end of the transparency.
8	Stack onto Master A	1. Place a 2nd transparency onto the first one. 2. Use a 50 mL serological pipette (or similar cylindrical object) to roll over

		the two transparencies to displace excess PDMS (use gentle hand pressure). Wipe the top of the 2nd transparency with an IPA soaked Texwipe to remove any particles. 3. Stack 5 more transparencies on top of the first 2. The top (7th) transparency is the small sheet cut to the size of the device footprint (see Appendix D for stack illustration). 4. Place a blank Si wafer (polished side down) on the stack. 5. Place 2 Texwipes on the stack. The cloths assist in providing uniform pressure distribution across the devices and soft contact with the steel plates. 6. Place steel plates on the stack amounting 40 lbs force. 7. Stack must sit on the lab table for 10 min (at room temperature) to allow initial displacement of PDMS. Note: Transparencies must be kept clean throughout stacking process to prevent particles from lodging between sheets. Tape should be used to secure transparencies to the large backing transparency.
9	Partial cure master A	1. Remove steel weights from stack. 2. Carry master A (with stack of transparencies, blank wafer, and Texwipes) to a hot plate and place on center of hot plate. Hot plate must be flat with uniform heat (for semiconductor processing; this work used the CEE 100CB plate, Brewer Science Inc., Rolla, MO, USA. Hot plate must be 80 °C. 3. Quickly re-stack steel plates on hot plate and allow stack to heat for 10.5 min. 4. Remove steel weights, carry master/transparencies/wafer stack to a lab table, and allow to cool for 5 min. 5. Remove the blank wafer and transparencies. 6. Carefully (and slowly) peel the first transparency off of the partially cured PDMS on master A. The partially cured PDMS should be tacky.
10	Cut slabs, punch, align, and bond	1. Cut devices out of the PDMS slab from master B. 2. Punch input/output ports into slab devices using 20G luer stubs. 3. Blow compressed gas through each port to remove residual particles of PDMS and use Scotch tape to clean off both sides of the slab devices. 4. Use stereo-zoom microscope to align each slab device to a device location on master A. Rework if alignment is out of tolerance. 5. Place master A (with aligned slab devices) into an oven at 70 °C for 12+ hrs to fully cure and thermally bond both layers.

BACK-END PROCESSING		
Step #	**Step Name**	**Description**
1	Cut and punch devices	1. Remove master A (with device slabs) from oven. 2. Use blade to cut the thin layer of PDMS (from master A) along the edges of each device slab. 3. Gently peel each device (2 bonded layers of PDMS) off of master A and store in a dust-free container (like a new Petri dish). 4. Punch input/output ports for valve control channels into devices using 21G luer stubs. 5. Blow compressed gas through each port to remove residual particles of PDMS and use Scotch tape to clean off both sides of the slab devices.
2	Plasma bond to glass	1. Place a device and a glass slide (or cover slip) into air plasma bonding chamber (Plasma Cleaner PDC-32G, Harrick Plasma, Ithaca, NY, USA). Make sure the device and glass are clean and free of particles. 2. Expose device and glass to air plasma for 30 s at 18 W power. Remove both from chamber. 3. Place device on the glass within 1 min. Gently tap the device (using tweezers or similar object) to make contact between the device and glass. Do not press firmly, as PDMS features may collapse.

APPENDIX F

TRANSWELL ASSAYS

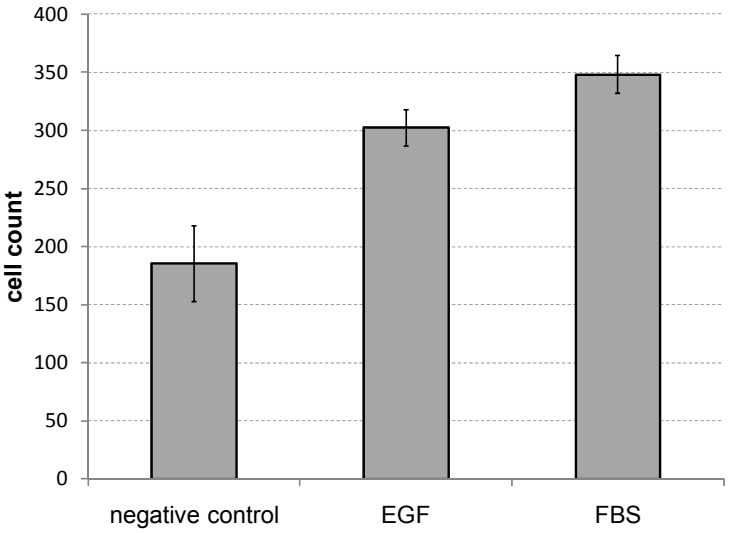

Fig. F-1 Transwell assays, testing responses of cells (MDA-MB-231) to signals (FBS and EGF). Membranes were pre-coated with fibronectin (8 μg/ml) for adhesion. Cells were seeded at equal densities per well (80,000 cells/well) and were incubated for 6 hours. After incubation, cells on the lower surface of the membrane were stained with hematoxylin and counted in the field of view under a light microscope in 3 different locations per well. Each assay condition is performed in triplicate. FBS concentration is 10% v/v in L-15 medium. EGF concentration is 50 ng/mL in L-15 medium. Error bars are SEM.

APPENDIX G

CONTROLS TRIALS FOR FBS GRADIENT EXPERIMENTS

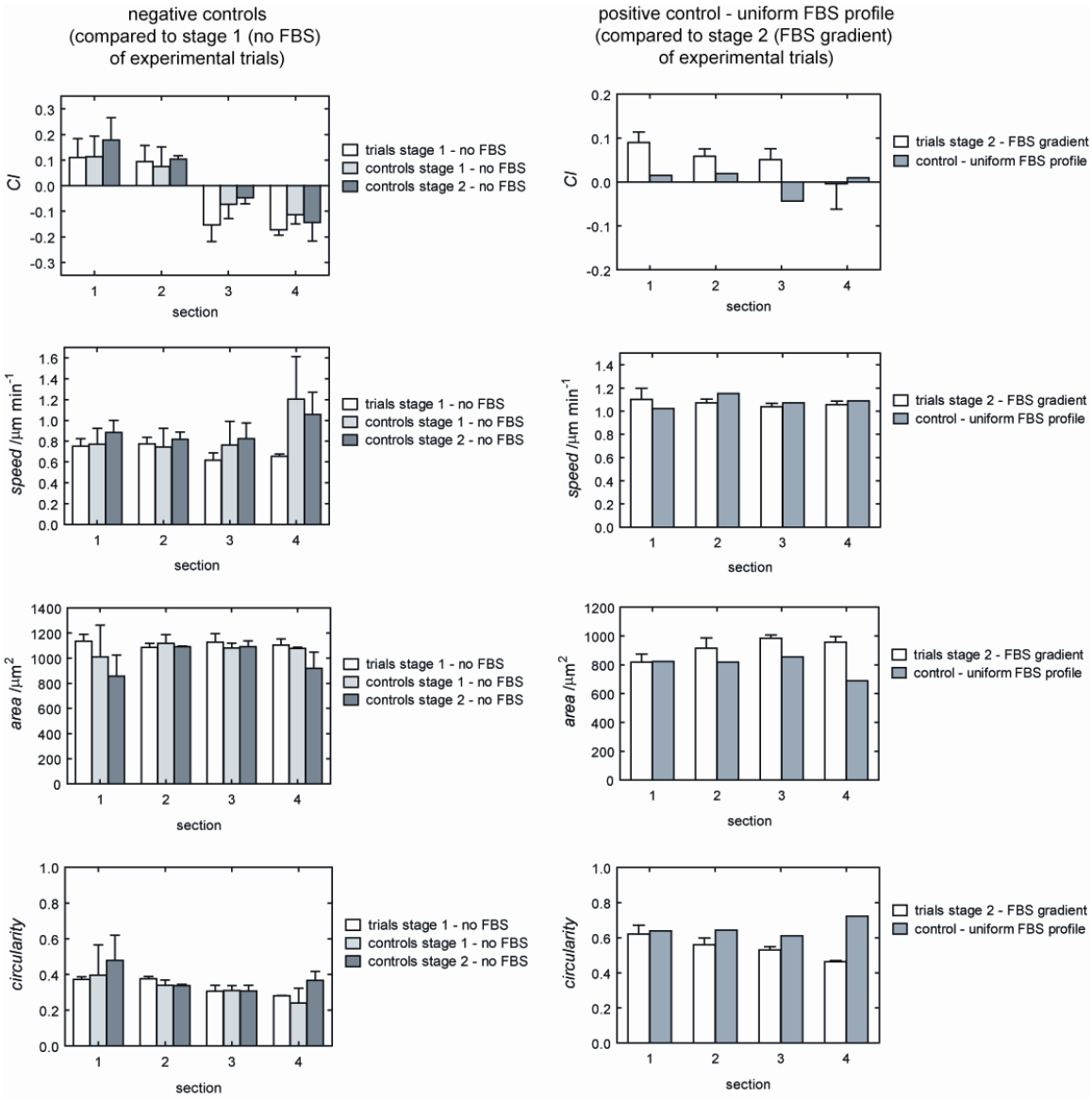

Fig. G-1 Negative (left) and positive (right) controls compared to gradient trials. Negative controls (N=2 trials) are compared to stage 1 (the non-gradient stage) of gradient trials (N=3); no significant differences are measured between conditions in any of the 4 sections (all pairwise tests yield $p>0.05$). Positive control (N=1) is compared to stage 2 (gradient stage) of gradient trials.

APPENDIX H

TIME-DEPENDENT RESULTS FROM FBS GRADIENT EXPERIMENTS

The CI for each section is shown over the 18 hour trial course (Fig. H-1). The first 6 hours are without a gradient, while the 12 following hours are with the gradient switched on. Sections 1 and 2 show no significant changes in CI between conditions, while sections 3 and 4 suggest an upward shift in CI upon gradient stimulation. These trends are consistent with the spatial plots in Fig. 5-9.

The first 3 hours with gradient is followed by possible adaptation over the following hours (Fig. H-2, especially area and circularity columns). Such trends suggest that cells may be returning to non-gradient behavior, which could be caused by cellular adaptation (as previously stated), desensitization, and/or receptor saturation or endocytosis in response to the new microenvironment. The trend is detectable to varying degrees in sections 1, 2 and 3; in contrast, section 4 (furthest from the gradient source) shows a less severe response.

Time dependent results could be helpful too further understand the transient progression of cellular response; however, further trials are required to make conclusions.

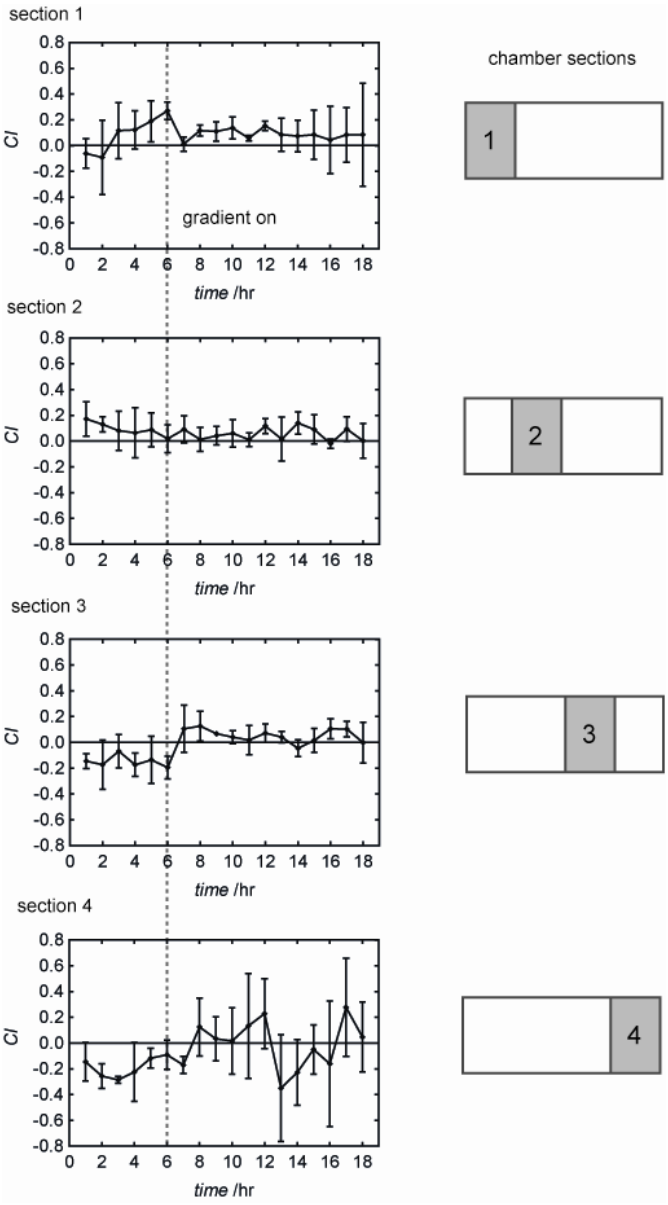

Fig. H-1 Chemotactic index (CI) by time, stratified by spatial section of chamber. Cells are monitored for 6 hrs with no FBS stimuli. At 6 hrs, a FBS gradient is applied and cells are monitored for 12 hrs following. Experimental conditions the same as described in Fig. 5-9. Error bars are SEM.

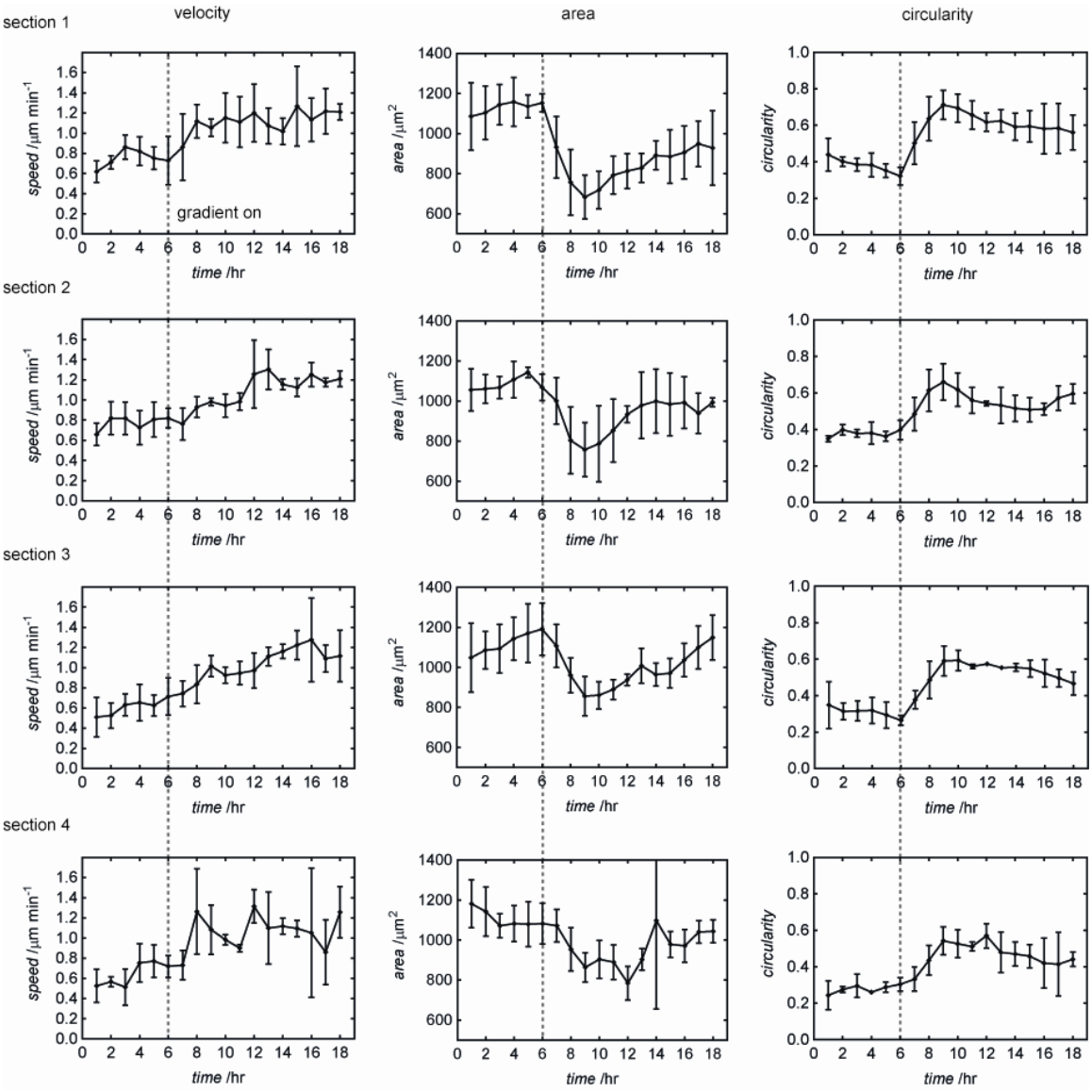

Fig. H-2 Speed, area, and circularity by time, stratified by spatial section of chamber. Cells are monitored for 6 hrs with no FBS stimuli. At 6 hrs, a FBS gradient is applied and cells are monitored for 12 hrs following. Experimental conditions the same as described in Fig. 5-9. Error bars are SEM.

APPENDIX I

CELL SEGMENTATION CODE

Cell segmentation code was written in MATLAB script, and is shown below. The code executes the segmentation heuristic described in Chapter 5 (Methods).

```
function image_segmentation(Trial, Well, Part, Thresh)
%IMAGE_SEGMENTATION Perform cell segmentation on a single sequence.
%   Please make sure that the flattened sequence file is in the folder
of
%   the current trial.  Then, enter the Trial#, Well#, Part#, and
%   thresholding factor (separated by commas) when calling this
function.
%
%   Remarks
%   -------
%   Use the run_segmentation function to perform a cell segmentation on
six
%   (6) different wells each in two (2) parts at a constant
thresholding
%   factor.
%
%   Example
%   -------
%   If the current sequence you want to segment is from Trial
%   5, Well 2, Part 1, with a thresholding factor of 0.7:
%
%   The T05_Well2_Part1 folder should include the file: -
%   T05_Well2_Part1_Flat.tif
%
%   And to perform the segmentation on this sequence you would type:
%
%   image_segmentation(05,2,1,0.7)
%
%   See also RUN_SEGMENTATION, IMAGE_DIVISION, RUN_DIVISION

% Begin the timer to determine the time required for this function
tic

% Convert numerical inputs to strings for creating filenames
Trial = num2str(Trial);
Well = num2str(Well);
Part = num2str(Part);

% Determine folder names and locations based on the current location of
the
% Cell Segmentation folder (using the pwd function) or the locations of
% folders created using the im_division function
trial_folder = strcat(pwd, '\', 'T', Trial, '_', 'Well', Well, '_',...
    'Part', Part, '\');
```

```
other_folder = strcat(trial_folder, '\', 'Other Sequences', '\');
final_folder = strcat(trial_folder, '\', 'Final Sequences', '\');

% Create the Final Sequences folder (the other folders should have
already
% been created in the im_division function).  Since we will be writing
to
% this folder only (no reading), it does not need to be added to the
% current directory.
% mkdir(final_folder);

% Make the folders accessible when running this function
addpath(trial_folder);
addpath(other_folder);
addpath(final_folder);

% Determine the names and locations of the divided images sequence, the
% flattened images sequence, the ROI images sequence, and the yet to be
% created segmented and overlay image sequences from the user inputs of
% trial #, well #, and part #
im_divided_name = strcat(pwd, '\', 'T', Trial, '_', 'Well', Well,...
    '_', 'Part', Part, '_', 'Divided', '.', 'tif');
im_ROI_name = strcat(other_folder, 'T', Trial, '_', 'Well', Well,
'_',...
    'Part', Part, '_', 'ROI', '.', 'tif');
im_flat_name = strcat(pwd, '\', 'T', Trial, '_', 'Well', Well, '_',...
    'Part', Part, '_', 'Flat', '.', 'tif');
im_segmented_name = strcat(pwd, '\', 'T', Trial, '_', 'Well', Well,...
    '_', 'Part', Part, '_', 'Segmented', '.', 'tif');
im_overlay_name = strcat(pwd, '\', 'T', Trial, '_', 'Well', Well,...
    '_', 'Part', Part, '_', 'Overlay', '.', 'tif');

% Determine number of images in the sequence using the imfinfo
function,
% and then store this number into sequence size
file_info = imfinfo(im_flat_name);
sequence_size = max(size(file_info));

% Begin iterating through the entire sequence to produce black and
white
% photos of cells only
for i = 1:sequence_size

    i % Display the current iteration

    % Read in the flattened image of the current iteration to begin
    % performing segmentation
    im_flat = imread(im_flat_name,i);


%%%%%%%%%%%%%%%%%%%%%%%%%%%%%%%%%%%%%%%%%%%%%%%%%%%%%%%%%%%%%%%%%%%%%%%
    %%%%%%%%%%%%%%%%%%%%%%% CELL PROCESS DETECTION
%%%%%%%%%%%%%%%%%%%%%%%%

%%%%%%%%%%%%%%%%%%%%%%%%%%%%%%%%%%%%%%%%%%%%%%%%%%%%%%%%%%%%%%%%%%%%%%%
```

```
    % Create a new image for manipulation to isolate the processes of
the
    % cells (while maintaining the quality of the original)
    im_processes = im_flat;

    % Define the threshold based on the median and standard
    % deviation of all pixel intensities within the ROI.  The user-
input
    % thresholding factor determines what fraction of the standard
    % deviation to subtract from the median pixel intensity.  Thus, the
    % threshold pixel intensity becomes the median pixel intensity
value of
    % the image less the standard deviation of all pixel intensities
    % multiplied by the user-input value.  Only the standard deviation
is
    % multiplied by the user-input value.
    stdev = std2(im_flat);
    range_factor_processes = median(im_flat(:))-Thresh*stdev;

    % Set all pixel intensities above the range factor for processes
    % (multiplied by the median pixel intensity spanning a 16-bit
image)
    % equal to zero (black).  This should eliminate most of the
background
    % and halos in the image since the processes are darker than both
of
    % these features.  This creates a logical, black and white image
where
    % processes should appear white on a black background.
    im_processes(im_processes > range_factor_processes) = 0;

    % Determine the areas of the resulting white pixel regions (i.e.,
the
    % area of the processes and small particles that may have been
picked
    % up during the process segmentation).  Label each of these areas
with
    % a region number using the bwlabel function.
    props_processes = regionprops(logical(im_processes), 'Area');
    im_label_processes = bwlabel(im_processes);

    % Find the regions of the black and white image that have a pixel
area
    % less than 30.
    index_processes = find([props_processes.Area] < 30);

    % Iterate through the regions with pixel areas less than 30 and set
the
    % pixel intensity values to zero.  This should eliminate small
debris
    % picked up during the process segmentation.
    for j = 1:length(index_processes)
        im_processes(im_label_processes == index_processes(j)) = 0;
    end
```

```
    % Create a structuring element to dilate (fatten) the processes,
and
    % then perform the dilation
    strel_processes = ones(5,5);
    im_processes = imdilate(im_processes, strel_processes);


%%%%%%%%%%%%%%%%%%%%%%%%%%%%%%%%%%%%%%%%%%%%%%%%%%%%%%%%%%%%%%%%%%%%%%%%%%%%
    %%%%%%%%%%%%%%%%%%%%%% CELL HALO (BODY) DETECTION
%%%%%%%%%%%%%%%%%%%%%%

%%%%%%%%%%%%%%%%%%%%%%%%%%%%%%%%%%%%%%%%%%%%%%%%%%%%%%%%%%%%%%%%%%%%%%%%%%%%

    % Create a new image for manipulation to isolate the halos (bodies)
of
    % the cells (while maintaining the quality of the original)
    im_halos = im_flat;

    % Define the thresholding fudge factor to capture the greatest
number
    % of halos during segmentation.  This value was found to be
relatively
    % constant for our images at 1.02, and it did not appear to require
any
    % incremental increase or decrease throughout the trials.
    range_factor_halos = 1.02;

    % Set all pixel intensities below the range factor for halos
    % (multiplied by the median pixel intensity spanning a 16-bit
image)
    % equal to zero (black).  This should eliminate most of the
background
    % and processes in the image since the halos are brighter than both
of
    % these features.  This creates a logical, black and white image
where
    % the halos should appear white on a black background.
    im_halos(im_halos < range_factor_halos*32768) = 0;

    % Determine the areas of the resulting white pixel regions (i.e.,
the
    % area of the halos and small particles that may have been picked
up
    % during the halo segmentation).  Then, label each of these areas
with
    % a region number using the bwlabel function.
    props_halos = regionprops(logical(im_halos), 'Area');
    im_label_halos = bwlabel(im_halos);


    % Find the regions of the black and white image that have a pixel
area
    % less than 30.
    index_halos = find([props_halos.Area] < 30);
```

```
    % Iterate through the regions with pixel areas less than 30 and set
the
    % pixel intensity values to zero.  This should eliminate small
bright
    % spots (debris or other fluctuations) picked up during the halo
    % segmentation.
    for j = 1:length(index_halos)
        im_halos(im_label_halos == index_halos(j)) = 0;
    end

    % Create a structuring element to dilate (fatten) the halos, and
then
    % perform the dilation.  This structuring element is smaller than
that
    % for processes because the halos represent a slightly fatter
region
    % than the actual cell bodies; however, it improves the likelihood
that
    % process and halo regions will meet in the combination step.
    strel_halos = ones(3,3);
    im_halos = imdilate(im_halos, strel_halos);


%%%%%%%%%%%%%%%%%%%%%%%%%%%%%%%%%%%%%%%%%%%%%%%%%%%%%%%%%%%%%%%%%%%%%%%
    %%%%%%%%%%%%%%%%%%% CELL PROCESS & HALO COMBINATION
%%%%%%%%%%%%%%%%%%%

%%%%%%%%%%%%%%%%%%%%%%%%%%%%%%%%%%%%%%%%%%%%%%%%%%%%%%%%%%%%%%%%%%%%%%%

    % Create an image that includes "positive" (white) pixels from the
    % logical process and halo images
    im_combined = im_halos | im_processes;

    % Create a structuring element to dilate the image of the combined
    % features (halos and processes) to increase the likelihood that
these
    % features will touch
    strel_dilate_combined = ones(4,4);

    % Perform the dilation and fill and holes between features with
    % positive (white) pixel values
    im_combined = imdilate(im_combined, strel_dilate_combined);
    im_combined = imfill(im_combined,'holes');

    % Now that the two features have been combined, create a
structuring
    % element to erode the resulting cells to improve their fit to the
    % actual size of the cells in the image
    strel_erode_combined = ones(7,7);

    % Perform the erosion
    im_combined = imerode(im_combined, strel_erode_combined);
```

```
    % Determine the areas of the resulting white pixel regions (i.e.,
the
    % area of the combined cell features and potential regions that do
not
    % correspond to a cell).  Then, label each of these areas with a
region
    % number using the bwlabel function.
    props_combined = regionprops(logical(im_combined), 'Area');
    im_label_combined = bwlabel(im_combined);

    % Find the regions of the black and white image that have a pixel
area
    % less than 300.  These regions should correspond to large non-cell
    % particles that were picked up during segmentation.
    index = find([props_combined.Area] < 300);

    % Iterate through the regions with pixel areas less than 300 and
set
    % the pixel intensity values to zero.
    for j = 1:length(index)
        im_combined(im_label_combined == index(j)) = 0;
    end

    % Convert the combined image from a logical to an 8-bit image
    im_combined = mat2gray(im_combined);

    % Write the final image of combined processes and halos as a black
and
    % white image
    imwrite(im_combined, im_segmented_name, 'tif', 'WriteMode',
'append');

end


% Begin iterating through the segmented image sequence to produce a
% sequence of photos in which the segmentation is "overlayed" on the
% original photos.  This provides a good way to determine how much of
the
% cell was segmented in the previous step, and it also allows for hand
% corrections if necessary.
for i = 1:sequence_size

    % Read in the black and white segmented image corresponding to the
    % current iteration
    im_segmented = imread(im_segmented_name, i);

    % Read in the corresponding ROI image (original phase photo) for
the
    % current iteration.  Convert to a grayscale image with pixel
    % intensities between 0 and 1 (this simplifies the overlay).  Since
we
    % later want to threshold these images so that cell regions are the
    % only pixels with maximum intensity, multiply the image by 0.98.
    im_overlay = mat2gray(imread(im_ROI_name, i));
```

```
    im_overlay = 0.98*im_overlay;

    % Find any non-black pixels from the segmented image and set the
    % corresponding pixels of the ROI image to the maximum pixel
intensity.
    im_overlay(im_segmented > 0) = 1;

    % Write the final overlay image to a file in the "Final Sequences"
    % folder.  Note that the image is saved as an 8-bit image.
    imwrite(im_overlay, im_overlay_name, 'tif', 'WriteMode', 'append');
end

% Move the divided image to the "Other Sequences" folder (to reduce
clutter
% within the current trial's folder).
%movefile(im_divided_name, other_folder);

toc % End the timer
```

REFERENCES

1. Bhadriraju, K. & Chen, C.S. Engineering cellular microenvironments to improve cell-based drug testing. *Drug Discovery Today* **7**, 612-620 (2002).
2. Butcher, E.C. Can cell systems biology rescue drug discovery? *Nature Reviews Drug Discovery* **4**, 461-467 (2005).
3. DiMasi, J.A., Hansen, R.W. & Grabowski, H.G. The price of innovation: new estimates of drug development costs. *Journal of Health Economics* **22**, 151-185 (2003).
4. Haney, S.A., LaPan, P., Pan, J. & Zhang, J. High-content screening moves to the front of the line. *Drug Discovery Today* **11**, 889-894 (2006).
5. Csete, M.E. & Doyle, J.C. Reverse Engineering of Biological Complexity. *Science* **295**, 1664-1669 (2002).
6. Kitano, H. Systems biology: a brief overview. *Science* **295**, 1662-1664 (2002).
7. Wikswo, J.P.*, et al.* Engineering challenges of BioNEMS: the integration of microfluidics, micro- and nanodevices, models, and external control for systems biology. *IEE Proceedings - Nanobiotechnology* **153**, 81-101 (2006).
8. Lang, P., Yeow, K., Nichols, A. & Scheer, A. Cellular imaging in drug discovery. *Nature Reviews. Drug Discovery* **5**, 343-356 (2006).
9. Sundberg, S.A. High-throughput and ultra-high-throughput screening: solution- and cell-based approaches. *Curr. Opin. Biotechnol.* **11**, 47-53 (2000).
10. El-Ali, J., Sorger, P.K. & Jensen, K.F. Cells on chips. *Nature* **442**, 403-411 (2006).
11. Alberts, B.*, et al. The Molecular Biology of the Cell*, (Garland Science, New York, NY, 2002).
12. The Development of *Drosophila melanogaster*. (eds. Bate, M. & Martinez, A.A.) (Cold Spring Harbor Laboratory Press, Cold Spring Harbor, NY, 1993).
13. Capdevila, J. & Belmonte, J.C.I. Patterning mechanisms controlling vertebrate limb development. *Annual Review of Cell and Developmental Biology* **17**, 87-132 (2001).
14. Schwartz, M.A. & Baron, V. Interactions between mitogenic stimuli, or, a thousand and one connections. *Current Opinion in Cell Biology* **11**, 197-202 (1999).
15. Scully, K.M. & Rosenfeld, M.G. Pituitary development: regulatory codes in mammalian organogenesis. *Science* **295**, 2231-2235 (2002).
16. Giancotti, F.G. Integrin signaling: specificity and control of cell survival and cell cycle progression. *Current Opinion in Cell Biology* **9**, 691-700 (1997).
17. Miyamoto, S., Teramoto, H., Gutkind, J.S. & Yamada, K.M. Integrins can collaborate with growth factors for phosphorylation of receptor tyrosine kinases and MAP kinase activation: roles of integrin aggregation and occupancy of receptors. *The Journal of Cell Biology* **135**, 1633-1642 (1996).
18. Roovers, K. & Assoian, R.K. Integrating the MAP kinase signal into the G1 phase cell cycle machinery. *BioEssays* **22**, 818-826 (2000).

19. Bond, M., Fabunmi, R.P., Baker, A.H. & Newby, A.C. Synergistic upregulation of metalloproteinase-9 by growth factors and inflammatory cytokines: an absolute requirement for transcription factor NF-κB. *FEBS Letters* **435**, 29-34 (1998).
20. Zhang, Y., McCluskey, K., Fujii, K. & Wahl, L.M. Differential regulation of monocyte matrix metalloproteinase and TIMP-1 production by TNF-α, granulocyte-macrophage CSF, and IL-1β through prostaglandin-dependent and -independent mechanisms. *The Journal of Immunology* **161**, 3071-3076 (1998).
21. Sweatt, D.J. The neuronal MAP kinase cascade: a biochemical signal integration system subserving synaptic plasticity and memory. *Journal of Neurochemistry* **76**, 1-10 (2001).
22. Watabe, A.M., Zaki, P.A. & O'Dell, T.J. Coactivation of β-adrenergic and cholinergic receptors enhances the induction of long-term potentiation and synergistically activates mitogen-activated protein kinase in the hippocampal CA1 region. *The Journal of Neuroscience* **20**, 5924-5931 (2000).
23. Parent, C.A. & Devreotes, P.N. A cell's sense of direction. *Science* **284**, 765-770 (1999).
24. Treier, M.*, et al.* Multistep signaling requirements for pituitary organogenesis in vivo. *Genes & Development* **12**, 1691-1704 (1998).
25. Flanagan, J.G. Neural map specification by gradients. *Current Opinion in Neurobiology* **16**, 59-66 (2006).
26. Hansen, M.J., Dallal, G.E. & Flanagan, J.G. Retinal Axon Response to Ephrin-As Shows a Graded, Concentration-Dependent Transition from Growth Promotion to Inhibition. *Neuron* **42**, 717-730 (2004).
27. Foxman, E.F., Campbell, J.J. & Butcher, E.C. Multistep navigation and the combinatorial control of leukocyte chemotaxis. *The Journal of Cell Biology* **139**, 1349-1360 (1997).
28. Foxman, E.F., Kunkel, E.J. & Butcher, E.C. Integrating conflicting chemotactic signals: the role of memory in leukocyte navigation. *The Journal of Cell Biology* **147**, 577-587 (1999).
29. Weinberg, R.A. *The Biology of Cancer*, (Garland Science, Taylor & Francis Group, LLC, New York, NY, 2007).
30. Gilles, C.*, et al.* Vimentin contributes to human mammary epithelial cell migration. *J Cell Sci* **112**, 4615-4625 (1999).
31. Hay, E.D. The mesenchymal cell, its role in the embryo, and the remarkable signaling mechanisms that create it. *Developmental Dynamics* **233**, 706-720 (2005).
32. Thiery, J.P. Epithelial-mesenchymal transitions in tumour progression. *Nat. Rev. Cancer* **2**, 442-454 (2002).
33. Haass, N., Smalley, K. & Herlyn, M. The Role of Altered Cell–Cell Communication in Melanoma Progression. *Journal of Molecular Histology* **35**, 309-318 (2004).
34. Grünert, S., Jechlinger, M. & Beug, H. Diverse cellular and molecular mechanisms contribute to epithelial plasticity and metastasis. *Nature Reviews. Molecular Cell Biology* **4**, 657-665 (2003).
35. Zavadil, J. & Bottinger, E.P. TGF-beta and epithelial-to-mesenchymal transitions. *Oncogene* **24**, 5764-5774 (2005).

36. Keller, R. Cell migration during gastrulation. *Current Opinion in Cell Biology* **17**, 533-541 (2005).
37. Schneider, V.A. & Granato, M. Motor axon migration: a long way to go. *Developmental Biology* **263**, 1-11 (2003).
38. Manes, S.*, et al.* Mastering time and space: immune cell polarization and chemotaxis. *Seminars in Immunology* **17**, 77-86 (2005).
39. Bruzzaniti, A. & Baron, R. Molecular recognition of osteoclast activity. *Reviews in Endocrine & Metabolic Disorders* **7**, 123-139 (2006).
40. Li, W., Fan, J., Chen, M. & Woodley, D.T. Mechanisms of human skin cell motility. *Histology and Histopathology* **19**, 1311-1324 (2004).
41. Yen, T.H. & Wright, N.A. The gastrointestinal tract stem cell niche. *Stem Cell Reviews* **2**, 203-212 (2006).
42. Friedl, P. & Wolf, K. Tumour-cell invasion and migration: diversity and escape mechanisms. *Nature Reviews Cancer* **3**, 362-374 (2003).
43. Lauffenburger, D.A. & Horwitz, A.F. Cell migration: A physically integrated molecular process. *Cell* **84**, 359-369 (1996).
44. Li, S., Guan, J.-L. & Chien, S. Biochemistry and biomechanics of cell motility. *Annual Review of Biomedical Engineering* **7**, 105-150 (2005).
45. Pollard, T.D., Borisy, G.G. & 112:453–65, C.m.d.b.a.a.d.o.a.f.C. Cellular motility driven by assembly and disassembly of actin filaments. *Cell* **112**, 453-465 (2003).
46. Huttenlocher, A.*, et al.* Regulation of cell migration by the calcium-dependent protease calpain. *Journal of Biological Chemistry* **272**, 32719-32722 (1997).
47. Palecek, S.P., Loftus, J.C., Ginsberg, M.H., Lauffenburger, D.A. & Horwitz, A.F. Integrin-ligand binding properties govern cell migration speed through cell-substratum adhesiveness. *Nature* **385**, 537-540 (1997).
48. Entschladen, F.*, et al.* Analysis methods of human cell migration. *Experimental Cell Research* **307**, 418-426 (2005).
49. Chan, A.Y., Bailly, M., Zebda, N., Segall, J.E. & Condeelis, J.S. Role of cofilin in epidermal growth factor-stimulated actin polymerization and lamellipod protrusion. *Journal of Cell Biology* **148**, 531-542 (2000).
50. Ichetovkin, I., Grant, W. & Condeelis, J.S. Cofilin produces newly polymerized actin filaments that are preferred for dendritic nucleation by the Arp2/3 complex. *Current Biology* **12**, 79-84 (2002).
51. Ilic, D.*, et al.* Reduced cell motility and enhanced focal adhesion contact formation in cells from FAK-deficient mice. *Nature* **377**, 539-544 (1995).
52. Ridley, A.J.*, et al.* Cell migration: integrating signals from front to back. *Science* **302**, 1704-1709 (2003).
53. Van Haastert, P.J.M. & Devreotes, P.N. Chemotaxis: signalling the way forward. *Nature Reviews Molecular Cell Biology* **5**, 626-634 (2004).
54. Sims, C.E. & Allbritton, N.L. Analysis of single mammalian cells on-chip. *Lab on a Chip* **7**, 423-440 (2007).
55. Whitesides, G.M. The origins and the future of microfluidics. *Nature* **442**, 368-373 (2006).
56. Squires, T.M. & Quake, S.R. Microfluidics: fluid physics at the nanoliter scale. *Reviews of Modern Physics* **77**, 977-1026 (2005).

57. Sawano, A., Takayama, S., Matsuda, M. & Miyawaki, A. Lateral propagation of EGF signaling after local stimulation is dependent on receptor density. *Developmental Cell* **3**, 245-257 (2002).
58. Takayama, S.*, et al.* Laminar flows - Subcellular positioning of small molecules. *Nature* **411**, 1016 (2001).
59. Takayama, S.*, et al.* Selective chemical treatment of cellular microdomains using multiple laminar streams. *Chemistry & Biology* **10**, 123-130 (2003).
60. Thorsen, T., Maerkl, S.J. & Quake, S.R. Microfluidic large-scale integration. *Science* **298**, 580-584 (2002).
61. Dittrich, P.S. & Manz, A. Lab-on-a-chip: microfluidics in drug discovery. *Nature Reviews Drug Discovery* **5**, 210-218 (2006).
62. Li, N., Tourovskaia, A. & Folch, A. Biology on a chip: microfabrication for studying the behavior of cultured cells. *Critical Reviews in Biomedical Engineering* **31**, 423-488 (2003).
63. Flaim, C.J., Chien, S. & Bhatia, S.N. An extracellular matrix microarray for probing cellular differentiation. *Nature Methods* **2**, 119-125 (2005).
64. Soen, Y., Mori, A., Palmer, T.D. & Brown, P.O. Exploring the regulation of human neural precursor cell differentiation using arrays of signaling microenvironments. *Molecular Systems Biology* **2**, 1-14 (article #37) (2006).
65. Boyden, S. The chemotactic effect of mixtures of antibody and antigen on polymorphonuclear leucocytes. *Journal of Experimental Medicine* **115**, 453-466 (1962).
66. Zicha, D., Dunn, G.A. & Brown, A.F. A new direct-viewing chemotaxis chamber. *Journal of Cell Science* **99**, 769-775 (1991).
67. Laevsky, G. & Knecht, D.A. Under-agarose folate chemotaxis of Dictyostelium discoideum amoebae in permissive and mechanically inhibited conditions. *Biotechniques* **31**, 1140-1142, 1144, 1146-1149 (2001).
68. Dertinger, S.K., Chiu, D.T., Jeon, N.L. & Whitesides, G.M. Generation of gradients having complex shapes using microfluidic networks. *Analytical Chemistry* **73**, 1240-1246 (2001).
69. Jeon, N.L.*, et al.* Neutrophil chemotaxis in linear and complex gradients of interleukin-8 formed in a microfabricated device. *Nature Biotechnology* **20**, 826-830 (2002).
70. Lin, F.*, et al.* Effective neutrophil chemotaxis is strongly influenced by mean IL-8 concentration. *Biochemical and Biophysical Research Communications* **319**, 576-581 (2004).
71. Saadi, W., Wang, S.-J., Lin, F. & Jeon, N.L. A parallel-gradient microfluidic chamber for quantitative analysis of breast cancer cell chemotaxis. *Biomedical Microdevices* **8**, 109-118 (2006).
72. Wang, S.J., Saadi, W., Lin, F., Nguyen, C.M.C. & Jeon, N.L. Differential effects of EGF gradient profiles on MDA-MB-231 breast cancer cell chemotaxis. *Experimental Cell Research* **300**, 180-189 (2004).
73. Chung, B.G.*, et al.* Human neural stem cell growth and differentiation in a gradient-generating microfluidic device. *Lab on a Chip* **5**, 401-406 (2005).

74. Hung, P.J., Lee, P.J., Sabounchi, P., Lin, R. & Lee, L.P. Continuous perfusion microfluidic cell culture array for high-throughput cell-based assays. *Biotechnology and Bioengineering* **89**, 1-8 (2004).
75. Lee, P.J., Hung, P.J., Rao, V.M. & Lee, L.P. Nanoliter scale microbioreactor array for quantitative cell biology. *Biotechnology and Bioengineering* **94**, 5-14 (2006).
76. Walker, G.M.*, et al.* Effects of flow and diffusion on chemotaxis studies in a microfabricated gradient generator. *Lab on a Chip* **5**, 611-618 (2005).
77. Yin, H.*, et al.* Influence of hydrodynamic conditions on quantitative cellular assays in microfluidic systems. *Analytical Chemistry*, (online advance article) (2007).
78. Chung, B.G., Lin, F. & Jeon, N.L. A microfluidic multi-injector for gradient generation. *Lab on a Chip* **6**, 764-768 (2006).
79. Lin, F.*, et al.* Neutrophil migration in opposing chemoattractant gradients using microfluidic chemotaxis devices. *Annals of Biomedical Engineering* **33**, 475-482 (2005).
80. Irimia, D.*, et al.* Microfluidic system for measuring neutrophil migratory response to fast switches of chemical gradients. *Lab on a Chip* **6**, 191-198 (2006).
81. Lin, F.*, et al.* Generation of dynamic temporal and spatial concentration gradients using microfluidic devices. *Lab on a Chip* **4**, 164-167 (2004).
82. Chen, L., Azizi, F. & Mastrangelo, C.H. Generation of dynamic chemical signals with microfluidic C-DACs. *Lab on a Chip* **7**, 850-855 (2007).
83. Unger, M.A., Chou, H.P., Thorsen, T., Scherer, A. & Quake, S.R. Monolithic microfabricated valves and pumps by multilayer soft lithography. *Science* **288**, 113-116 (2000).
84. Kartalov, E.P., Walker, C., Taylor, C.R., Anderson, W.F. & Scherer, A. Microfluidic vias enable nested bioarrays and autoregulatory devices in Newtonian fluids. *Proc. Natl. Acad. Sci. U. S. A.* **103**, 12280-12284 (2006).
85. Luo, Y.Q. & Zare, R.N. Perforated membrane method for fabricating three-dimensional polydimethylsiloxane microfluidic devices. *Lab Chip* **8**, 1688-1694 (2008).
86. McDonald, J.C. & Whitesides, G.M. Poly(dimethylsiloxane) as a Material for Fabricating Microfluidic Devices. *Accounts of Chemical Research* **35**, 491-499 (2002).
87. Kim, L., Vahey, M.D., Lee, H.Y. & Voldman, J. Microfluidic arrays for logarithmically perfused embryonic stem cell culture. *Lab Chip* **6**, 394-406 (2006).
88. Folch, A., Jo, B.H., Hurtado, O., Beebe, D.J. & Toner, M. Microfabricated elastomeric stencils for micropatterning cell cultures. *J. Biomed. Mater. Res.* **52**, 346-353 (2000).
89. McDonald, J.C.*, et al.* Fabrication of microfluidic systems in poly(dimethylsiloxane). *Electrophoresis* **21**, 27-40 (2000).
90. Madou, M.J. *Fundamentals of microfabrication : the science of miniaturization*, (CRC Press, Boca Raton :, 2002).
91. Lorenz, M.G.O. Liquid-handling robotic workstations for functional genomics. *Journal of the Association for Laboratory Automation* **9**, 262-267 (2004).

92. Gomez-Sjoberg, R., Leyrat, A.A., Pirone, D.M., Chen, C.S. & Quake, S.R. Versatile, fully automated, microfluidic cell culture system. *Anal. Chem.* **79**, 8557-8563 (2007).
93. http://www.fluidigm.com/.
94. Wang, H.Y., Bao, N. & Lu, C. A microfluidic cell array with individually addressable culture chambers. *Biosens. Bioelectron.* **24**, 613-617 (2008).
95. Park, E.S., Brown, A.C., DiFeo, M.A., Barker, T.H. & Lu, H. Continuously perfused, non-cross-contaminating microfluidic chamber array for studying cellular responses to orthogonal combinations of matrix and soluble signals. *Lab Chip* **10**, 571-580 (2010).
96. Yarmush, M.L. & King, K.R. Living-Cell Microarrays. *Annual Review of Biomedical Engineering* **11**, 235-257 (2009).
97. Soen, Y., Mori, A., Palmer, T.D. & Brown, P.O. Exploring the regulation of human neural precursor cell differentiation using arrays of signaling microenvironments. *Mol. Syst. Biol.* **2**, 14 (2006).
98. Jang, J.H. & Schaffer, D.V. Microarraying the cellular microenvironment. *Mol. Syst. Biol.* **2**, 2 (2006).
99. Flaim, C.J., Chien, S. & Bhatia, S.N. An extracellular matrix microarray for probing cellular differentiation. *Nat. Methods* **2**, 119-125 (2005).
100. Fernandes, T.G., Diogo, M.M., Clark, D.S., Dordick, J.S. & Cabral, J.M.S. High-throughput cellular microarray platforms: applications in drug discovery, toxicology and stem cell research. *Trends Biotechnol.* **27**, 342-349 (2009).
101. El-Ali, J., Sorger, P.K. & Jensen, K.F. Cells on chips. *Nature* **442**, 403-411 (2006).
102. Angres, B. Cell microarrays. *Expert Review of Molecular Diagnostics* **5**, 769-779 (2005).
103. Wang, C.J.*, et al.* A microfluidics-based turning assay reveals complex growth cone responses to integrated gradients of substrate-bound ECM molecules and diffusible guidance cues. *Lab Chip* **8**, 227-237 (2008).
104. Lee, P.J., Hung, P.J., Rao, V.M. & Lee, L.P. Nanoliter scale microbioreactor array for quantitative cell biology. *Biotechnol. Bioeng.* **94**, 5-14 (2006).
105. Hung, P.J., Lee, P.J., Sabounchi, P., Lin, R. & Lee, L.P. Continuous perfusion microfluidic cell culture array for high-throughput cell-based assays. *Biotechnol. Bioeng.* **89**, 1-8 (2005).
106. Hung, P.J.*, et al.* A novel high aspect ratio microfluidic design to provide a stable and uniform microenvironment for cell growth in a high throughput mammalian cell culture array. *Lab Chip* **5**, 44-48 (2005).
107. Di Carlo, D., Wu, L.Y. & Lee, L.P. Dynamic single cell culture array. *Lab Chip* **6**, 1445-1449 (2006).
108. Wang, Z.H., Kim, M.C., Marquez, M. & Thorsen, T. High-density microfluidic arrays for cell cytotoxicity analysis. *Lab Chip* **7**, 740-745 (2007).
109. Thompson, D.M.*, et al.* Dynamic gene expression profiling using a microfabricated living cell array. *Anal. Chem.* **76**, 4098-4103 (2004).
110. Sugiura, S., Edahiro, J., Kikuchi, K., Sumaru, K. & Kanamori, T. Pressure-driven perfusion culture microchamber array for a parallel drug cytotoxicity assay. *Biotechnol. Bioeng.* **100**, 1156-1165 (2008).

111. King, K.R.*, et al.* A high-throughput microfluidic real-time gene expression living cell array. *Lab Chip* **7**, 77-85 (2007).
112. Khademhosseini, A.*, et al.* Cell docking inside microwells within reversibly sealed microfluidic channels for fabricating multiphenotype cell arrays. *Lab Chip* **5**, 1380-1386 (2005).
113. Kim, L., Toh, Y.C., Voldman, J. & Yu, H. A practical guide to microfluidic perfusion culture of adherent mammalian cells. *Lab Chip* **7**, 681-694 (2007).
114. Schwartz, R.M., Palsson, B.O. & Emerson, S.G. RAPID MEDIUM PERFUSION RATE SIGNIFICANTLY INCREASES THE PRODUCTIVITY AND LONGEVITY OF HUMAN BONE-MARROW CULTURES. *Proceedings of the National Academy of Sciences of the United States of America* **88**, 6760-6764 (1991).
115. Minuth, W.W.*, et al.* Modulation of cell differentiation in perfusion culture. *Experimental Nephrology* **7**, 394-406 (1999).
116. Minuth, W.W.*, et al.* Culture of embryonic renal collecting duct epithelia in a gradient container. *Pediatric Nephrology* **11**, 140-147 (1997).
117. Leclerc, E.*, et al.* Study of osteoblastic cells in a microfluidic environment. *Biomaterials* **27**, 586-595 (2006).
118. Blagovic, K., Kim, L., Skelley, A.M. & Voldman, J. Microfluidic control of stem cell diffusible signaling. in *Twelfth International Conference on Miniaturized Systems for Chemistry and Life Sciences* 677-679 (San Diego, California, USA, 2008).
119. Aubry, L.*, et al.* Improvement of Culture Conditions of Human Embryoid Bodies Using a Controlled Perfused and Dialyzed Bioreactor System. *Tissue Engineering Part C-Methods* **14**, 289-298 (2008).
120. Frégeau, C.J., Yensen, C., Elliott, J. & Fourney, R.M. Optimized Configuration of Fixed-Tip Robotic Liquid-Handling Stations for the Elimination of Biological Sample Cross-Contamination. *Journal of the Association for Laboratory Automation* **12**, 339-354 (2007).
121. Derynck, R., Akhurst, R.J. & Balmain, A. TGF-beta signaling in tumor suppression and cancer progression. *Nature Genet.* **29**, 117-129 (2001).
122. Pedersen, J.A., Boschetti, F. & Swartz, M.A. Effects of extracellular fiber architecture on cell membrane shear stress in a 3D fibrous matrix. *J. Biomech.* **40**, 1484-1492 (2007).
123. Chary, S.R. & Jain, R.K. DIRECT MEASUREMENT OF INTERSTITIAL CONVECTION AND DIFFUSION OF ALBUMIN IN NORMAL AND NEOPLASTIC TISSUES BY FLUORESCENCE PHOTOBLEACHING. *Proc. Natl. Acad. Sci. U. S. A.* **86**, 5385-5389 (1989).
124. Nawshad, A., LaGamba, D., Polad, A. & Hay, E.D. Transforming growth factor-beta signaling during epithelial-mesenchymal transformation: Implications for embryogenesis and tumor metastasis. 11-23 (Karger, 2005).
125. Greenburg, G. & Hay, E.D. EPITHELIA SUSPENDED IN COLLAGEN GELS CAN LOSE POLARITY AND EXPRESS CHARACTERISTICS OF MIGRATING MESENCHYMAL CELLS. *J. Cell Biol.* **95**, 333-339 (1982).
126. Kalluri, R. & Neilson, E.G. Epithelial-mesenchymal transition and its implications for fibrosis. *J. Clin. Invest.* **112**, 1776-1784 (2003).

127. Saika, S.*, et al.* Smad3 signaling is required for epithelial-mesenchymal transition of lens epithelium after injury. *Am. J. Pathol.* **164**, 651-663 (2004).
128. Kim, K.K.*, et al.* Alveolar epithelial cell mesenchymal transition develops in vivo during pulmonary fibrosis and is regulated by the extracellular matrix. *Proceedings of the National Academy of Sciences of the United States of America* **103**, 13180-13185 (2006).
129. Sheppard, D. Epithelial integrins. *Bioessays* **18**, 655-660 (1996).
130. Serini, G. & Gabbiani, G. Mechanisms of myofibroblast activity and phenotypic modulation. *Exp. Cell Res.* **250**, 273-283 (1999).
131. Jones, J.L. & Walker, R.A. Integrins: a role as cell signalling molecules. *J. Clin. Pathol.-Mol. Pathol.* **52**, 208-213 (1999).
132. Handschuh, G.*, et al.* Tumour-associated E-cadherin mutations alter cellular morphology, decrease cellular adhesion and increase cellular motility. *Oncogene* **18**, 4301-4312 (1999).
133. Balzac, F.*, et al.* E-cadherin endocytosis regulates the activity of Rap1: a traffic light GTPase at the crossroads between cadherin and integrin function. *J. Cell Sci.* **118**, 4765-4783 (2005).
134. Aman, A. & Piotrowski, T. Cell migration during morphogenesis. *Dev. Biol.* **341**, 20-33 (2010).
135. Dormann, D. & Weijer, C.J. Chemotactic cell movement during development. *Curr. Opin. Genet. Dev.* **13**, 358-364 (2003).
136. Hatten, M.E. Central nervous system neuronal migration. *Annu. Rev. Neurosci.* **22**, 511-539 (1999).
137. Warburton, D.*, et al.* The molecular basis of lung morphogenesis. *Mech. Dev.* **92**, 55-81 (2000).
138. Gurtner, G.C., Werner, S., Barrandon, Y. & Longaker, M.T. Wound repair and regeneration. *Nature* **453**, 314-321 (2008).
139. Martin, P. Wound healing - Aiming for perfect skin regeneration. *Science* **276**, 75-81 (1997).
140. Mutsaers, S.E., Bishop, J.E., McGrouther, G. & Laurent, G.J. Mechanisms of tissue repair: From wound healing to fibrosis. *Int. J. Biochem. Cell Biol.* **29**, 5-17 (1997).
141. Luster, A.D., Alon, R. & von Andrian, U.H. Immune cell migration in inflammation: present and future therapeutic targets. *Nat. Immunol.* **6**, 1182-1190 (2005).
142. Robertson, M.J. Role of chemokines in the biology of natural killer cells. *J. Leukoc. Biol.* **71**, 173-183 (2002).
143. Zhelev, D.V. & Alteraifi, A. Signaling in the motility responses of the human neutrophil. *Ann. Biomed. Eng.* **30**, 356-370 (2002).
144. Friedl, P. & Wolf, K. Tumour-cell invasion and migration: Diversity and escape mechanisms. *Nat. Rev. Cancer* **3**, 362-374 (2003).
145. Yamaguchi, H., Wyckoff, J. & Condeelis, J. Cell migration in tumors. *Curr. Opin. Cell Biol.* **17**, 559-564 (2005).
146. Yilmaz, M. & Christofori, G. Mechanisms of Motility in Metastasizing Cells. *Mol. Cancer Res.* **8**, 629-642 (2010).

147. Van Haastert, P.J.M. & Devreotes, P.N. Chemotaxis: Signalling the way forward. *Nat. Rev. Mol. Cell Biol.* **5**, 626-634 (2004).
148. Lauffenburger, D.A. & Horwitz, A.F. Cell migration: A physically integrated molecular process. *Cell* **84**, 359-369 (1996).
149. Weiner, O.D. Regulation of cell polarity during eukaryotic chemotaxis: the chemotactic compass. *Curr. Opin. Cell Biol.* **14**, 196-202 (2002).
150. Swaney, K.F., Huang, C.H. & Devreotes, P.N. Eukaryotic Chemotaxis: A Network of Signaling Pathways Controls Motility, Directional Sensing, and Polarity. in *Annual Review of Biophysics, Vol 39*, Vol. 39 265-289 (Annual Reviews, Palo Alto, 2010).
151. Etienne-Manneville, S. Polarity proteins in migration and invasion. *Oncogene* **27**, 6970-6980 (2008).
152. Ridley, A.J.*, et al.* Cell migration: Integrating signals from front to back. *Science* **302**, 1704-1709 (2003).
153. Boyden, S. CHEMOTACTIC EFFECT OF MIXTURES OF ANTIBODY AND ANTIGEN ON POLYMORPHONUCLEAR LEUCOCYTES. *J. Exp. Med.* **115**, 453-& (1962).
154. Zigmond, S.H. ABILITY OF POLYMORPHONUCLEAR LEUKOCYTES TO ORIENT IN GRADIENTS OF CHEMOTACTIC FACTORS. *J. Cell Biol.* **75**, 606-616 (1977).
155. Foxman, E.F., Campbell, J.J. & Butcher, E.C. Multistep navigation and the combinatorial control of leukocyte chemotaxis. *J. Cell Biol.* **139**, 1349-1360 (1997).
156. Nelson, R.D., Quie, P.G. & Simmons, R.L. CHEMOTAXIS UNDER AGAROSE - NEW AND SIMPLE METHOD FOR MEASURING CHEMOTAXIS AND SPONTANEOUS MIGRATION OF HUMAN POLYMORPHONUCLEAR LEUKOCYTES AND MONOCYTES. *J. Immunol.* **115**, 1650-1656 (1975).
157. Song, H.J., Ming, G.L. & Poo, M.M. CAMP-induced switching in turning direction of nerve growth cones. *Nature* **388**, 275-279 (1997).
158. Ming, G.L.*, et al.* Adaptation in the chemotactic guidance of nerve growth cones. *Nature* **417**, 411-418 (2002).
159. Gundersen, R.W. & Barrett, J.N. NEURONAL CHEMOTAXIS - CHICK DORSAL-ROOT AXONS TURN TOWARD HIGH-CONCENTRATIONS OF NERVE GROWTH-FACTOR. *Science* **206**, 1079-1080 (1979).
160. Entschladen, F.*, et al.* Analysis methods of human cell migration. *Exp. Cell Res.* **307**, 418-426 (2005).
161. Keenan, T.M. & Folch, A. Biomolecular gradients in cell culture systems. *Lab Chip* **8**, 34-57 (2008).
162. Pujic, Z., Mortimer, D., Feldner, J. & Goodhill, G.J. Assays for Eukaryotic Cell Chemotaxis. *Comb. Chem. High Throughput Screen* **12**, 580-588 (2009).
163. Toetsch, S., Olwell, P., Prina-Mello, A. & Volkov, Y. The evolution of chemotaxis assays from static models to physiologically relevant platforms. *Integr. Biol.* **1**, 170-181 (2009).
164. Takayama, S.*, et al.* Laminar flows - Subcellular positioning of small molecules. *Nature* **411**, 1016-1016 (2001).

165. Breslauer, D.N., Lee, P.J. & Lee, L.P. Microfluidics-based systems biology. *Mol. Biosyst.* **2**, 97-112 (2006).
166. Dittrich, P.S. & Manz, A. Lab-on-a-chip: microfluidics in drug discovery. *Nature Reviews Drug Discovery* **5**, 210-218 (2006).
167. Weibel, D.B. & Whitesides, G.M. Applications of microfluidics in chemical biology. *Curr. Opin. Chem. Biol.* **10**, 584-591 (2006).
168. Kim, S., Kim, H.J. & Jeon, N.L. Biological applications of microfluidic gradient devices. *Integr. Biol.* **2**, 584-603 (2010).
169. Irimia, D. Microfluidic Technologies for Temporal Perturbations of Chemotaxis. in *Annual Review of Biomedical Engineering, Vol 12*, Vol. 12 259-284 (Annual Reviews, Palo Alto, 2010).
170. Jeon, N.L.*, et al.* Neutrophil chemotaxis in linear and complex gradients of interleukin-8 formed in a microfabricated device. *Nat. Biotechnol.* **20**, 826-830 (2002).
171. Barkefors, I.*, et al.* Endothelial cell migration in stable gradients of vascular endothelial growth factor a and fibroblast growth factor 2 - Effects on chemotaxis and chemokinesis. *J. Biol. Chem.* **283**, 13905-13912 (2008).
172. Chung, B.G.*, et al.* Human neural stem cell growth and differentiation in a gradient-generating microfluidic device. *Lab Chip* **5**, 401-406 (2005).
173. Lin, F.*, et al.* Effective neutrophil chemotaxis is strongly influenced by mean IL-8 concentration. *Biochem. Biophys. Res. Commun.* **319**, 576-581 (2004).
174. Wang, S.J., Saadi, W., Lin, F., Nguyen, C.M.C. & Jeon, N.L. Differential effects of EGF gradient profiles on MDA-MB-231 breast cancer cell chemotaxis. *Exp. Cell Res.* **300**, 180-189 (2004).
175. Bhattacharjee, N., Li, N.Z., Keenan, T.M. & Folch, A. A neuron-benign microfluidic gradient generator for studying the response of mammalian neurons towards axon guidance factors. *Integr. Biol.* **2**, 669-679 (2010).
176. Keenan, T.M., Hsu, C.H. & Folch, A. Microfluidic "jets" for generating steady-state gradients of soluble molecules on open surfaces. *Appl. Phys. Lett.* **89**(2006).
177. Shamloo, A., Ma, N., Poo, M.M., Sohn, L.L. & Heilshorn, S.C. Endothelial cell polarization and chemotaxis in a microfluidic device. *Lab Chip* **8**, 1292-1299 (2008).
178. Abhyankar, V.V., Lokuta, M.A., Huttenlocher, A. & Beebe, D.J. Characterization of a membrane-based gradient generator for use in cell-signaling studies. *Lab Chip* **6**, 389-393 (2006).
179. Cate, D.M., Sip, C.G. & Folch, A. A microfluidic platform for generation of sharp gradients in open-access culture. *Biomicrofluidics* **4**, 044105 (2010).
180. Kim, D., Lokuta, M.A., Huttenlocher, A. & Beebe, D.J. Selective and tunable gradient device for cell culture and chemotaxis study. *Lab Chip* **9**, 1797-1800 (2009).
181. Mosadegh, B.*, et al.* Uniform cell seeding and generation of overlapping gradient profiles in a multiplexed microchamber device with normally-closed valves. *Lab Chip* **10**, 2959-2964 (2010).
182. Torisawa, Y.-s.*, et al.* Microfluidic platform for chemotaxis in gradients formed by CXCL12 source-sink cells. *Integr. Biol.* **2**, 680-686 (2010).

183. Cheng, S.Y.*, et al.* A hydrogel-based microfluidic device for the studies of directed cell migration. *Lab Chip* **7**, 763-769 (2007).
184. Walker, G.M.*, et al.* Effects of flow and diffusion on chemotaxis studies in a microfabricated gradient generator. *Lab Chip* **5**, 611-618 (2005).
185. Iijima, M., Huang, Y.E. & Devreotes, P. Temporal and spatial regulation of chemotaxis. *Dev. Cell* **3**, 469-478 (2002).
186. Gurdon, J.B. & Bourillot, P.Y. Morphogen gradient interpretation. *Nature* **413**, 797-803 (2001).
187. Herzmark, P.*, et al.* Bound attractant at the leading vs. the trailing edge determines chemotactic prowess. *Proc. Natl. Acad. Sci. U. S. A.* **104**, 13349-13354 (2007).
188. Diao, J.P.*, et al.* A three-channel microfluidic device for generating static linear gradients and its application to the quantitative analysis of bacterial chemotaxis. *Lab Chip* **6**, 381-388 (2006).
189. Periasamy, N. & Verkman, A.S. Analysis of Fluorophore Diffusion by Continuous Distributions of Diffusion Coefficients: Application to Photobleaching Measurements of Multicomponent and Anomalous Diffusion. *Biophys. J.* **75**, 557-567 (1998).
190. Wittmer, C.R., Phelps, J.A., Saltzman, W.M. & Van Tassel, P.R. Fibronectin terminated multilayer films: Protein adsorption and cell attachment studies. *Biomaterials* **28**, 851-860 (2007).
191. Jabbarzadeh, E. & Abrams, C.F. Chemotaxis and random motility in unsteady chemoattractant fields: a computational study. *J. Theor. Biol.* **235**, 221-232 (2005).
192. Insall, R.H. Understanding eukaryotic chemotaxis: a pseudopod-centred view. *Nat. Rev. Mol. Cell Biol.* **11**, 453-458 (2010).
193. Muller, A.*, et al.* Involvement of chemokine receptors in breast cancer metastasis. *Nature* **410**, 50-56 (2001).
194. Bifulco, K.*, et al.* Cell invasiveness in sarcomas: a possibly useful clinical correlation. *Tumori* **94**, 505-510 (2008).
195. Lauffenburger, D.A. & Linderman, J.J. *Receptors: Models for Binding, Trafficking, and Signaling*, (Oxford University Press, Inc., New York, NY, 1993).
196. Keane, J.T., Ryan, D. & Gray, P.P. Effect of shear stress on expression of a recombinant protein by Chinese hamster ovary cells. *Biotechnol. Bioeng.* **81**, 211-220 (2003).